UNIVERSIDAD TÉCNICA FEDERICO SANTA MARÍA
DEPARTMENT OF ELECTRONIC ENGINEERING

DOCTORAL DISSERTATION
INSTANTANEOUS POWER CONSUMPTION WITH REGENERATIVE BRAKING MODEL FOR N-TRAILERS SYSTEM ON OFF-ROAD SCENARIOS.

FRANCO ARIEL JORQUERA PEZOA

DOCTORATE PROGRAM
DOCTORATE IN ELECTRONIC ENGINEERING

THESIS SUPERVISOR : PROF. DR. FERNANDO AUAT CHEEIN
EVALUATION COMMITTEE : PROF. DR. MATÍAS ZAÑARTU
: PROF. DR. FRANCISCO VARGAS
: PROF. DR. MARCOS ORCHAD

OCTOBER 2025

VALPARAÍSO-CHILE

CONSTANCIA DE VALIDACIÓN Y CONFIDENCIALIDAD DE MONOGRAFÍA A REPOSITORIO ACADÉMICO

1.- IDENTIFICACIÓN DEL TRABAJO ACADÉMICO

Tipo de monografía (marcar una opción): ☐ Memoria o trabajo de título ☒ Tesis de Postgrado

Título del trabajo: instantaneous power consumption with regenerative braking model for N-trailers system on off-road scenarios.

Nombre del candidato(a): Franco Ariel Jorquera Pezoa

Carrera / Grado: Doctorado en Ingeniería Electrónica

Campus: Casa Central **Departamento:** Electrónica

2.- VALIDACIÓN DEL PROFESOR GUÍA/DIRECTOR DE TESIS

Yo, Fernando Alfredo Auat Cheein, en mi calidad de profesor guía del trabajo académico mencionado anteriormente **DEJO CONSTANCIA** que:

- He revisado esta versión del documento y corresponde a la versión final aprobada del trabajo.
- El trabajo cumple con los requisitos académicos y de formato establecidos por la institución.

3.- EVALUACIÓN DE CONFIDENCIALIDAD POR PROPIEDAD INDUSTRIAL (marcar una opción)

☒ El trabajo **NO contiene** información que amerite confidencialidad y puede ser publicado de inmediato en repositorio con acceso abierto.

☐ El trabajo **CONTIENE** información con potenciales implicancias de propiedad industrial o intelectual y requiere un periodo de confidencialidad (**embargo**) por **(marcar una opción)**:

☐ 6 meses ☐ 12 meses ☐ 2 años ☐ 3 años ☐ 5 años ☐ 10 años

Fundamentación de la necesidad de confidencialidad (obligatorio si se solicita embargo):

4.- FIRMAS

Profesor(a) guía o director(a) de memoria o tesis:

Fecha: 19-11-2025 **Firma:**

Estudiante o Candidato(a):

Fecha: 18/11/2025 **Firma:**

Este formulario debe ser insertado como página 2 de la memoria o tesis, completado y firmado por estudiante y profesor(a) antes de la entrega en portal PRISMA de Biblioteca USM.

To my family …

I dedicate this work to all those who have supported me throughout my academic journey. To my parents, uncles, cousins, and grandparents, each of you has shaped the person I am today through your love, values, and encouragement. Even those who are no longer with us continue to live on in my heart, and their influence has guided me every step of the way.
Above all, I dedicate this work to my beloved partner, who has walked beside me through all these years. Her patience, unwavering support, and loving guidance have been my anchor during the most challenging moments and my source of joy in times of triumph. This achievement is as much hers as it is mine.

Acknowledgements

I would like to express my deepest gratitude to Prof. Dr. Fernando Auat Cheein for his invaluable guidance and support throughout this academic journey, which began in 2020 during my Master's program and continued through my Doctorate. His profound wisdom, remarkable patience, and unwavering support have been a constant source of inspiration, extending far beyond academic matters.

I would also like to extend my sincere gratitude to Prof. Dr. Matías Zañartu, a remarkable person whose constant support, generosity, and willingness to help made him an essential part of my academic formation. His guidance has been a fundamental pillar throughout this process, for which I am truly grateful.

I am also sincerely thankful to Dr. Leonardo Guevara, an outstanding professional and person with whom I had the opportunity to collaborate remotely. He generously shared his work with me and entrusted me to be part of it, which allowed me to further explore and build upon the solid foundations he established.

My heartfelt thanks also go to Dr. Néstor Denis (Nahuel), with whom I had the great pleasure of collaborating. I deeply appreciate his patience, his generosity, and his willingness to teach and share his knowledge.

I would also like to extend my appreciation to PhD(c) Juan Estrada for his valuable support during the experimental stage of this research and for sharing his expertise from his field of study. Without a doubt, he is an inspiring and remarkable researcher.

I am grateful to the Universidad Técnica Federico Santa María for its excellent academic program and for the scholarships that allowed me to pursue my studies. I also acknowledge AC3E and the Basal Project AFB240002 for providing access to their facilities, equipment, and administrative support throughout the development of this thesis. Finally, I would like to express my sincere appreciation to the Agencia Nacional de Investigación y Desarrollo (ANID) for the multiple financial supports that made this research possible, particularly through the ANID-PFCHA/Doctorado Nacional/2024-21242630 scholarship program.

I would like to express my sincere gratitude to CODELCO and its Piensa Minería Program – 2023 Process for providing the financial support that enabled the development of this research. The funding granted made it possible to carry out the project and progress consistently toward its objectives.

I appreciate the confidence placed in this work and the opportunity to conduct a study supported by such a prominent national institution. Thank you to CODELCO and the Piensa Minería Program for contributing to the advancement of applied research and innovation in electromobility and the mining sector.

RESUMEN EJECUTIVO

Esta tesis presenta un marco integral de modelado y análisis para el sistema N-Trailer Generalizado (GNT), una clase de vehículos articulados no holonómicos compuestos por un tractor tipo uniciclo y un número arbitrario de remolques acoplados pasivamente. Se desarrolla una formulación dinámica completa basada en el método de Euler-Lagrange, incorporando los efectos de la distribución de masas, fuerzas de Coriolis y restricciones no holonómicas, las cuales se imponen mediante una matriz jacobiana de restricciones y su proyección asociada al espacio nulo. Se modelan explícitamente las interacciones externas, incluyendo la resistencia al rodado mediante fricción dinámica tipo LuGre, la resistencia aerodinámica en función de la velocidad, y los efectos gravitacionales sobre pendientes. Las ecuaciones resultantes se expresan en coordenadas reducidas, lo que permite un tratamiento coherente de las entradas de control y fuerzas de restricción. Se enfatiza especialmente la estimación en tiempo real del consumo instantáneo de potencia, calculado como el producto interno entre los torques actuadores y las velocidades angulares proyectadas en el espacio nulo. El modelo permite capturar tanto el consumo de energía como los eventos de regeneración, cuantificando la energía recuperada durante fases de desaceleración o descenso. Esta formulación energética proporciona una base físicamente coherente para evaluar el desempeño y optimizar los flujos de potencia del sistema en condiciones reales de operación fuera de carretera.

ABSTRACT

This thesis presents a comprehensive modeling and analysis framework for the Generalized N-Trailer (GNT) system, a class of nonholonomic articulated vehicles composed of a unicycle tractor and an arbitrary number of passively coupled trailers. A full dynamic formulation based on the Euler-Lagrange method is developed, incorporating the effects of mass distribution, Coriolis forces, and nonholonomic constraints enforced through a constraint Jacobian and its associated null space projection. External interactions are explicitly modeled, including rolling resistance via LuGre dynamic friction, aerodynamic drag as a function of velocity, and gravitational forces projected on sloped terrains. The resulting dynamic equations are expressed in reduced coordinates, allowing consistent treatment of control inputs and constraint forces. Particular emphasis is placed on the real-time estimation of instantaneous power consumption, which is computed as the inner product of actuator torques and angular velocities projected through the null space. The model captures both energy consumption and regenerative braking events, enabling the quantification of energy recovered during deceleration or downhill motion. This energetic formulation offers a physically consistent basis for evaluating performance and optimizing power flow in realistic off-road scenarios, paving the way for energy-aware control strategies in future work.

Contents

List of Tables

List of Figures

1 | Introduction

This thesis presents the development of a generalized dynamic model for an n-trailer system that explicitly incorporates the terramechanical interaction between the wheels and the ground, with the aim of estimating the instantaneous power consumption during off-road operation. This chapter outlines the problem statement and the motivations that have driven this research.

1.1 Introduction

The global transition toward cleaner energy sources has intensified in recent years, driven by the urgent need to mitigate climate change and reduce greenhouse gas emissions. Within this context, electromobility has emerged as a pivotal strategy for minimizing dependence on fossil-based fuels. Electric vehicles (EVs), encompassing automobiles, buses, trucks, and emerging autonomous solutions, are becoming central to this shift (2; 3). Beyond individual automotive units, electromobility encompasses more complex configurations such as *N-Trailers*, where one or more passive trailers are coupled to an electric tractor, offering new opportunities for off-road applications (4).

N-Trailer systems, while demonstrating promising adaptability for challenging environments such as agriculture and mining, face operational constraints associated with uneven terrain, variable masses, and intricate mechanical interactions (5; 6). These environments are characterized by soil deformability, non-uniform rolling resistance, and significant slope variations, which collectively demand advanced modeling approaches that account for physical phenomena and dynamic interactions. Consequently, there is growing interest in developing accurate models of instantaneous power consumption (IPC) alongside robust control systems tailored to these off-road scenarios (7; 8).

Numerous studies have explored IPC and energy consumption modeling for EVs. IPC models often rely on the forces interacting with a vehicle's motion and speed (9; 10). Specific research has been conducted under off-road conditions, allowing classification and quantification of terrain-mechanical impacts on power consumption (11). A critical factor influencing energy efficiency is regenerative braking, which facilitates partial energy recovery during deceleration. Studies have explored the operation of regenerative braking systems, addressing limitations based on torque and speed thresholds and identifying strategies for maximizing energy recovery (12; 13; 14).

Energy modeling has expanded to specialized platforms, such as Mecanum wheelset omnidirectional robots, which incorporate slope effects into consumption predictions, achieving high precision (15). Similarly, Husky robots have been used to analyze energy-aware trajectories (16). The effects of ground conditions on energy consumption have also been studied, with geodetic measurements and velocity variations integrated into dynamic models of skid-steer robots (17). Another approach uses GNSS and camera-based data to develop IPC models for car-like platforms in agricultural applications (18).

Machine learning techniques have further enhanced IPC and energy consumption predictions. Algorithms such as support vector machines (SVM), multiple linear regression (MLR), and deep learning have been employed for this purpose (19; 20). Control strategies that optimize energy usage, such as differential unicycle robot trajectory planning, have also been proposed, with studies incorporating location uncertainties and energy optimization considerations (21; 22; 23). Routing algorithms, such as those based on Dijkstra's algorithm, have modeled vehicle energy consumption within broader fleet management contexts (24).

For N-Trailer systems, kinematic and dynamic modeling has evolved significantly. Researchers have focused on N-Trailer kinematics for differential and Ackermann-type vehicles (25; 26; 27). Studies highlight the necessity of trailers in agricultural tasks, performing preliminary energy analyses (28), and presenting detailed models of articulated vehicles (29). Skid-steer robots have been used to estimate terrain effects on agricultural environments, linking contact surface forces to power consumption (30; 31). Additionally, dynamic models for autonomous vehicles have addressed trajectory control, center-of-gravity shifts, and curvature-induced effects on road conditions (32; 33).

The overarching motivation for this research lies in advancing energy-efficient and reliable motion modeling for agricultural machinery operating under challenging off-road scenarios. Mechanized solutions have long supported tasks such as fertilization, harvesting, and transport (34; 35). Today, concerns over sustainability and the adoption of electromobility add new dimensions to these technologies, enabling advanced techniques for energy measurement, mass estimation, and real-time traction analysis (4; 36). Electrified machinery promises not only reduced carbon emissions but also enhanced precision in farming operations, from load estimation to optimized battery utilization and regenerative braking (37; 38).

This work focuses specifically on the development of a generalized dynamic model for N-Trailer systems intended to operate in off-road environments. The model incorporates terramechanical interactions such as terrain slope and frictional forces, and evaluates how regenerative braking influences the instantaneous energy demand of each component. Unlike control-oriented formulations, this approach emphasizes the numerical simulation of motion and energy flows, without relying on NMPC frameworks, experimental validation, or virtual environments like Gazebo.

1.2 Hypotheses

According to previous research, the principal shortcomings identified in the state of the art can be summarized as follows: (1) the absence of a dynamic model that generalizes the components of the N-trailer system, and (2) the lack of a power consumption formulation that considers not only longitudinal motion but also two-dimensional displacements, including the effects of regenerative braking. These limitations have motivated the authors to pose the following research hypotheses:

- **Hypothesis 1 (H1):** Most existing works on N-trailer systems have predominantly focused on kinematic formulations that significantly simplify the real behavior of articulated vehicles. However, these models fail to capture essential dynamic phenomena, particularly those arising in off-road agricultural environments. This research posits that a generalized dynamic model explicitly incorporating wheel–soil terramechanical interactions enables a more accurate representation of the system dynamics under such conditions.
- **Hypothesis 2 (H2):** Current formulations of energy consumption in N-trailer systems tend to either neglect regenerative braking effects or represent them under overly simplified assumptions. This work hypothesizes that incorporating a dynamic formulation of regenerative braking into the instantaneous power estimation framework can substantially enhance the accuracy of energy consumption predictions, especially during deceleration phases and operations over inclined or irregular terrain.

1.3 Objectives

The main objective of this research is to develop a generalized dynamic model for N-Trailer systems operating in off-road environments, enabling the estimation of instantaneous power consumption by incorporating terramechanical interactions and regenerative braking effects. The goal is to establish a physically consistent framework for analyzing the energetic behavior of articulated vehicles in complex terrain.

The specific objectives of this project are:

- **SO1:** To derive a dynamic model for generalized N-Trailer systems using Lagrangian mechanics, explicitly incorporating mass distribution, kinematic constraints, trailer coupling, and wheel–soil interaction. This objective addresses Hypothesis 1 by capturing the dynamic behavior of the system in off-road conditions, moving beyond simplified kinematic formulations.
- **SO2:** To formulate a model for instantaneous power consumption based on the developed dynamics, including energy contributions from inertial effects, traction forces, and regenerative braking. The model will allow for simulation-based analyses of power profiles in representative scenarios, thus supporting Hypothesis 2 regarding the impact of regenerative mechanisms on energy efficiency.

1.4 Scope

The scope of this thesis encompasses the development, formalization, and in-depth analysis of a generalized N-Trailer system composed of unicycle-type vehicles operating under off-road conditions. The studied configuration considers a single electric tractor coupled to one or more passive trailers, modeled through a framework that explicitly incorporates the distribution of mass across the system, the kinematic and dynamic effects of mechanical coupling, and the nonlinear interactions between the wheels and the supporting terrain. This modeling perspective enables the characterization of fundamental behaviors that emerge from vehicle–trailer dynamics, which are of particular relevance in agricultural, forestry, and other off-road mobility contexts.

Although a variety of N-Trailer configurations can be found in the literature, including car-like or Ackermann-type steering architectures, this work restricts its focus to unicycle-based systems. This choice is motivated by the fact that such systems present a balance between structural simplicity and the ability to capture complex coupling phenomena, making them suitable for generalization without oversimplifying critical dynamic effects. By leveraging this configuration, it becomes possible to derive compact yet expressive symbolic models that retain the fidelity necessary for analyzing mechanical energy flows, while avoiding the excessive parametrization and control dependencies often associated with more complex steering mechanisms.

The propulsion system under consideration is assumed to be based on electric actuation, exemplified here by a brushed direct current (DC) motor. This assumption facilitates the integration of an electromechanical perspective into the modeling framework, enabling the explicit computation of instantaneous power consumption. The proposed formulation accounts for the various contributions to power demand, including traction effort, inertial forces, resistive effects arising from wheel–soil contact, gravitational components induced by terrain gradients, and the potential recovery of energy through regenerative braking during decelerated or downhill motion. This comprehensive energy representation is derived analytically and subsequently examined through numerical simulation, ensuring that the analysis remains grounded in well-established physical principles.

In line with the research objectives, the scope is deliberately limited to a symbolic and numerical modeling framework, excluding any implementation of real-time trajectory control, physical prototyping, or field experimentation. By focusing exclusively on the theoretical formulation and computational validation of the proposed models, this thesis establishes a robust foundation for understanding the energetic behavior of generalized N-Trailer systems. This approach ensures that the results directly support Hypotheses H1 and H2, offering a framework that can be further extended in future work to incorporate control strategies, optimization-based decision-making, and experimental validation in real-world scenarios.

1.5 Thesis Organization

This dissertation is structured into six chapters.

Chapter 2 reviews the state of the art in N-Trailer systems, focusing on their application in agriculture and robotics, with particular emphasis on kinematic and dynamic modeling approaches. It also explores the concept of instantaneous power consumption (IPC) in electric vehicles and discusses existing formulations that incorporate terrain interaction and regenerative braking.

Chapter 3 presents the research methodology, outlining the procedures used to develop a generalized dynamic model for N-Trailer systems. It includes the selection of modeling techniques, the formulation of terramechanical interactions, and the integration of regenerative braking into the dynamic framework.

Chapter 4 is devoted to the mathematical modeling of the N-Trailer system. It introduces the generalized coordinates, constraints, and motion equations derived via Lagrangian formalism, and describes how the model components (mass, inertia, terrain, etc.) are parameterized and structured for simulation.

Chapter 5 details the formulation of instantaneous power consumption for the N-Trailer system, incorporating traction, inertial, gravitational, and braking contributions. Particular attention is given to modeling the energy recuperation due to regenerative braking and evaluating its influence under variable terrain conditions.

Chapter 6 presents simulation-based results obtained from different case studies involving off-road scenarios. It analyzes the energetic behavior of the system, compares configurations with and without regenerative braking, and assesses how different model parameters affect instantaneous power demand.

Finally, Chapter 7 summarizes the key findings, highlights the main contributions of this research, and proposes directions for future work, such as extending the dynamic model to more complex trailer topologies, incorporating additional terrain models, and exploring hardware implementation strategies.

2 | Background and related work

This chapter provides a comprehensive review of the state of the art concerning N-Trailer systems, their industrial applications, kinematic and dynamic modeling, and considerations for instantaneous power consumption in electric vehicles. Special focus is placed on off-road environments and the potential for regenerative braking within these contexts.

2.1 Industrial Applications of Generalized N-Trailer Systems

Generalized N-Trailer (GNT) systems, composed of a tractor vehicle and multiple passive trailers, are widely employed in various industries due to their modularity, scalability, and load capacity. These systems are essential in logistics, mining, and agriculture, where terrain irregularities and energy constraints challenge vehicle efficiency. This section discusses the relevance of N-Trailer platforms in real-world industrial applications, motivating the need for accurate dynamic modeling and instantaneous power consumption estimation.

2.1.1 Applications in Logistics and Port Operations

In logistics and warehousing, GNT systems are extensively used to facilitate the internal transportation of goods. These platforms improve efficiency by enabling a single operator to move multiple trailers with varying loads across structured environments such as airport tarmacs and cargo terminals. Figure 2.1 illustrates a luggage N-Trailer configuration typically used in airport operations.

The electrification of Automated Guided Vehicles (AGVs) for intralogistics has promoted the adoption of electric N-Trailer systems in smart warehouses, improving energy efficiency and enabling data-driven fleet coordination (39). These vehicles require scalable control and power estimation techniques, especially when operating continuously across varying payload conditions and distances (6).

2.1.2 Mining Transport Systems and Energy Challenges

In mining, articulated vehicles with multiple trailers are used to transport heavy payloads over unstructured terrain, including gravel roads and slopes. These configurations reduce

Figure 2.1: Luggage N-Trailer used in airport operations. Source: www.gse.blumenbecker.com

ground pressure, improving terrain preservation and traction. Figure 2.2 shows a typical articulated mining truck operating in off-road conditions.

Figure 2.2: Articulated mining truck Komatsu HM400 used in off-road conditions. Source: www.komatsu.com

The mining sector is undergoing a transition toward hybrid and fully electric haulage systems. These vehicles require accurate models for predicting energy consumption under load, terrain deformation, and regenerative braking events. The estimation of IPC in such systems is essential for battery sizing, route planning, and performance monitoring (40).

2.1.3 Agricultural Machinery and Off-road Variability

Agriculture is another domain where GNT systems are employed for transporting harvested crops and distributing materials such as fertilizers or seeds. These vehicles operate on heterogeneous soils like clay, grass, and sand, where surface conditions change with weather, moisture, and mechanical compaction. Figure 2.3 shows a typical agricultural N-Trailer configuration.

Figure 2.3: N-Trailer system used in agricultural applications. Source: hzpt.com

Electric tractors and harvesters are increasingly being introduced in precision farming. These systems benefit from IPC models that incorporate terrain variability and the dynamic behavior of the payload. For instance, real-time estimation techniques can enhance operational planning and extend battery range by modeling regenerative phases and energy-intensive operations such as hill climbing or sudden deceleration (41).

2.1.4 Motivation for Dynamic Modeling and Energy Estimation

Despite their practical relevance, most GNT systems in industrial applications rely on static or kinematic models that fail to capture the complexities of trailer articulation, terrain interaction, and inertial coupling. These simplifications limit the accuracy of energy consumption estimation, particularly in electric systems subject to regenerative braking and variable loads.

This thesis addresses this gap by proposing a dynamic modeling framework that explicitly considers segmental dynamics, terrain-induced resistance, and braking recovery, tailored to generalized N-Trailer configurations. The objective is to provide a foundational model suitable for future energy-aware applications, including simulation-based planning and optimization.

2.2 Kinematic and Dynamic Modeling of N-Trailer Systems

This section reviews the fundamental modeling approaches for N-Trailer systems, starting with classical kinematic structures and progressing toward dynamic formulations that incorporate terrain interactions. These models provide a critical foundation for understanding system behavior, predicting motion trajectories, and estimating power consumption in realistic off-road scenarios.

2.2.1 Overview of Classical Kinematic Models (SNT, nSNT, GNT)

N-Trailer systems can be broadly classified based on their hitch configurations. The most common types are Standard N-Trailers (SNT), Non-Standard N-Trailers (nSNT), and Generalized N-Trailers (GNT). In SNT systems, all trailer hitches are aligned with the axle centerlines, whereas in nSNT configurations, the hitches are placed off-axle. GNT structures generalize both previous cases, combining on-axle and off-axle connections, which results in greater flexibility but also increased complexity in modeling and control (4; 42).

Due to their constrained kinematics and underactuated nature, GNT configurations are particularly challenging. Figure 2.4 illustrates a representative GNT system, where trailers are modeled as unicycle-like units and their hitch offsets determine the propagation of angles and velocities across the chain of segments.

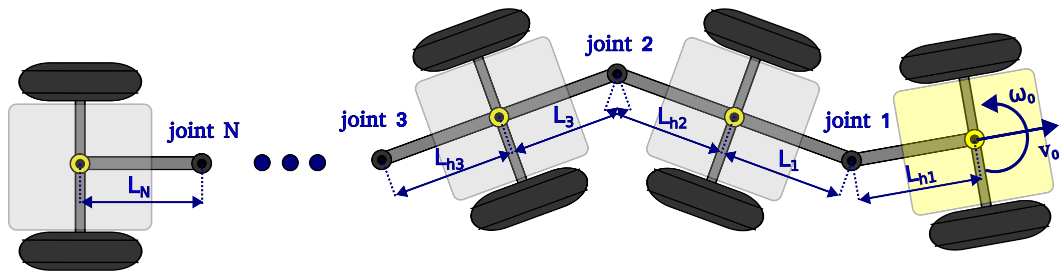

Figure 2.4: Generalized N-Trailer (GNT) configuration with interleaved on-axle and off-axle hitching. Each trailer is modeled as a unicycle-like segment.

2.2.2 Recursive Kinematics in Generalized Configurations

The recursive formulation of N-Trailer kinematics is essential for scalable modeling. Considering each trailer as a unicycle, the position and orientation of the i-th segment can be recursively defined from the preceding segment using holonomic and non-holonomic constraints. Assuming a rolling-without-slipping condition, the configuration vector $\mathbf{q}_i = [x_i, y_i, \theta_i]^T$ evolves as:

$$\dot{\mathbf{q}}_i = \begin{bmatrix} 0 & \cos(\theta_i) \\ 0 & \sin(\theta_i) \\ 1 & 0 \end{bmatrix} \begin{bmatrix} \omega_i \\ v_i \end{bmatrix} = G(q_i)u_i \tag{2.1}$$

This recursive structure enables the extension of kinematic models to an arbitrary number of segments while maintaining a compact representation. However, it also introduces challenges, such as the jackknifing effect and non-minimum phase behavior during backward motion or high-curvature turns, as observed in (43).

2.2.3 Dynamic Modeling from Lagrangian Mechanics

While kinematic models are suitable for motion planning and path tracking, they are insufficient for analyzing energy consumption and system stability in uneven terrain. Dynamic modeling, grounded in Lagrangian mechanics, incorporates mass distribution, inertial forces, and external effects. Each trailer is associated with a mass m_i, position $\mathbf{p}_i$, and orientation θ_i, and the system dynamics can be derived from:

$$\frac{d}{dt}\left(\frac{\partial \mathcal{L}}{\partial \dot{q}_i}\right) - \frac{\partial \mathcal{L}}{\partial q_i} = Q_i \tag{2.2}$$

Here, $\mathcal{L} = T - V$ represents the Lagrangian, with T being the total kinetic energy and V the potential energy of the system. The generalized forces Q_i capture friction, gravitational components, and traction or braking forces.

Recent studies, such as (44; 45; 46), have advanced scalable approaches to model full dynamics of articulated vehicles in agricultural and mining contexts, highlighting the relevance of coupling between trailers and the impact of variable loads.

2.2.4 Incorporation of Wheel-Soil Interaction via Dynamic Friction Modeling

Accurately representing the interaction between the wheels and the terrain is crucial for evaluating energy consumption and motion dynamics in N-Trailer systems, especially in off-road environments. Instead of using classical terramechanics formulations, this thesis employs a dynamic friction model based on the LuGre framework. This approach allows for the incorporation of both static and kinetic friction behaviors, including the Stribeck effect, in a compact yet expressive formulation.

The LuGre model introduces an internal state variable z representing the average deflection of bristles at the contact surface. The dynamics of z are given by:

$$\dot{z} = v - \frac{|v|}{g(v)} z \tag{2.3}$$

The resulting friction force f_{LuGre} is expressed as:

$$f_{\text{LuGre}} = \sigma_0 z + \sigma_1 \dot{z} + \sigma_2 v \tag{2.4}$$

where v is the relative velocity at the wheel-soil interface, σ_0 is the stiffness coefficient, σ_1 is the microdamping coefficient, and σ_2 models viscous friction. The function $g(v)$ captures the Stribeck effect and is typically defined as:

$$g(v) = F_c + (F_s - F_c)\exp\left(-\left(\frac{v}{v_s}\right)^2\right) \tag{2.5}$$

Here, F_s and F_c are the static and kinetic friction coefficients, respectively, and v_s is the Stribeck velocity that defines the transition between the two regimes.

This friction model enables the accurate representation of traction losses, resistance during deceleration, and regenerative braking effects. Moreover, it allows the system to respond realistically to variations in terrain conditions without requiring explicit empirical parameters for different soil types. As a result, it provides a practical compromise between physical fidelity and computational efficiency, well suited for generalized dynamic modeling of N-Trailer systems (47; 33).

2.3 Instantaneous Power Consumption in Electric Vehicles

The concept of instantaneous power consumption (IPC) in electric vehicles (EVs) refers to the power drawn from the energy source to maintain vehicle motion at a given time. Estimating IPC is crucial for optimizing energy-aware navigation, predicting battery autonomy, and analyzing the energetic behavior of electric powertrains in variable environments. These estimations become particularly relevant for off-road articulated systems, where terrain variability, trailer articulation, and load changes affect traction forces and regenerative behavior.

2.3.1 Fundamental Forces and Power Components

The total traction force $F_{\text{tr}}(t)$ required to maintain motion in an EV results from the combination of aerodynamic drag, gravitational slope force, rolling resistance, and inertial (acceleration-related) effects:

$$F_{\text{tr}}(t) = F_{\text{aero}}(t) + F_{\text{hc}}(t) + F_{\text{fr}}(t) + F_{\text{ac}}(t), \tag{2.6}$$

where:

- $F_{\text{aero}}(t) = \frac{1}{2}\rho C_d A v^2(t)$, aerodynamic drag,
- $F_{\text{hc}}(t) = m(t) g \sin(\theta(t))$, hill-climbing or gravitational component,
- $F_{\text{fr}}(t) = \mu_{\text{rr}} m(t) g \cos(\theta(t))$, rolling resistance,
- $F_{\text{ac}}(t) = m(t) a(t)$, inertial or acceleration force.

The instantaneous mechanical power at the wheel is then:

$$P_{\text{tr}}(t) = F_{\text{tr}}(t) \cdot v(t). \tag{2.7}$$

These components are depicted in Fig. 2.5, which shows the external forces acting on the vehicle as it ascends a slope.

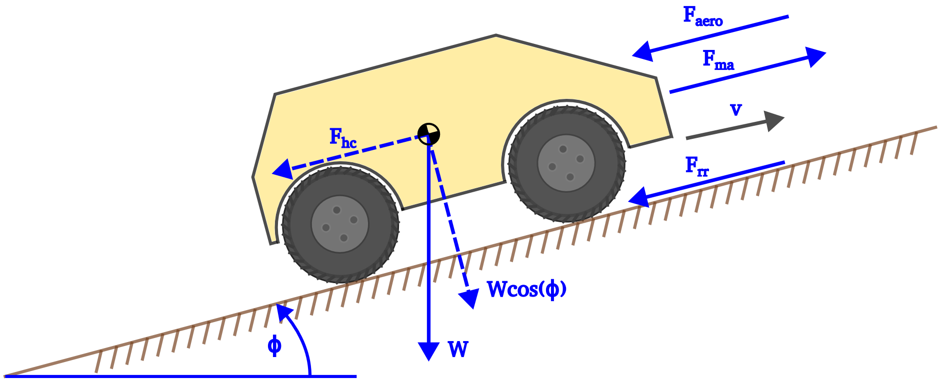

Figure 2.5: Force components acting on a vehicle on an inclined surface.

2.3.2 IPC Models in On-Road and Off-Road Environments

Most IPC models for on-road scenarios assume rigid surfaces, low curvature trajectories, and constant vehicle mass. However, in off-road conditions such as agricultural fields or mining operations, these assumptions are no longer valid. The terrain becomes deformable, the vehicle mass varies due to loading/unloading, and elevation changes introduce additional resistive forces. Ignoring these factors leads to underestimated power consumption (18). Improved models that incorporate terrain interaction, such as soil deformation and slip, are necessary to capture the real power demands in such environments (7).

2.3.3 Regenerative Braking Integration

Regenerative braking is the process by which kinetic energy is partially recovered during deceleration and converted into electrical energy to recharge the battery. The efficiency of this process depends on motor speed, torque limits, inverter capabilities, and battery acceptance rate. Typically, only a fraction of the braking energy is recovered due to saturation in the power electronics or battery state-of-charge limits.

Fig. 2.7 illustrates the power flow during motoring, while Fig. 2.6 presents the power flow in regenerative braking mode.

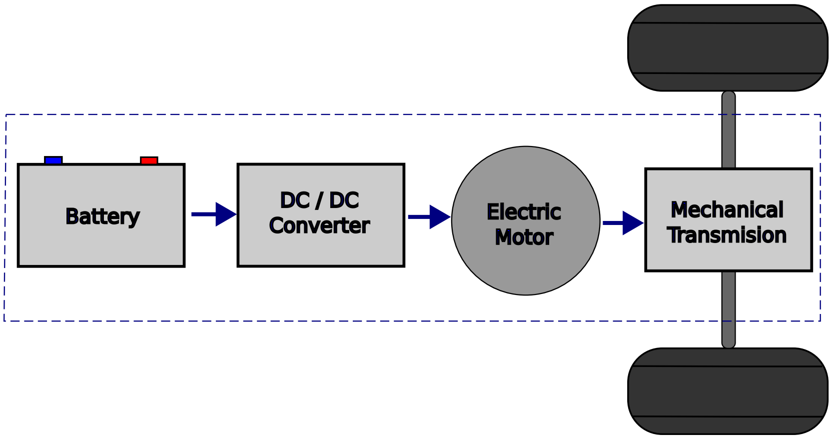

Figure 2.6: Overall power flow in electric vehicles, including energy losses in battery, inverter, motor, and transmission.

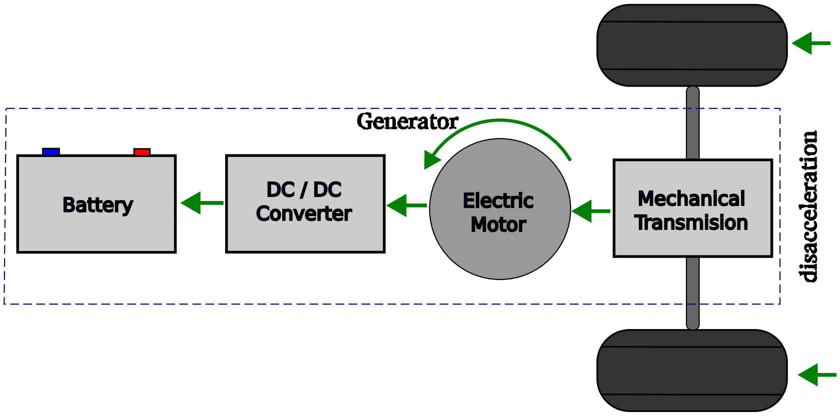

Figure 2.7: Power flow in electric vehicles with regenerative braking.

2.3.4 Efficiencies in the Powertrain: Battery, Inverter, Motor, and Transmission

The net electric-to-mechanical power transfer is affected by a cascade of subsystems, each with its own efficiency. The power extracted from the battery is first processed by the power electronics, passed to the motor, and finally delivered through the transmission to the wheels. Each stage introduces energy losses:

- **Battery efficiency** η_{bat}: typically 90–98%, depending on temperature, state-of-charge, and internal resistance.
- **Inverter efficiency** η_{inv}: ranges from 94–98%, influenced by switching frequency and load conditions.
- **Motor efficiency** η_{mot}: varies with torque-speed conditions, ranging between 80–96%.

- **Transmission efficiency** η_{tr}: usually between 85–95%, depending on gear ratios and mechanical friction.

  The overall system efficiency is given by:

$$\eta_{\text{sys}} = \eta_{\text{bat}} \cdot \eta_{\text{inv}} \cdot \eta_{\text{mot}} \cdot \eta_{\text{tr}}. \tag{2.8}$$

These losses are critical in IPC estimation, especially under highly variable torque demand, regenerative braking, or when operating near the limits of inverter or motor performance. Additionally, manufacturers often provide normalized motor maps using base values ($T_{\text{base}}, \omega_{\text{base}}, P_{\text{base}}$) to allow scaling and system identification across different platforms (10; 48).

2.3.5 Sensor-Based and Data-Driven Approaches

Recent studies have leveraged sensor-based frameworks to estimate IPC in real time (49; 50). These include GNSS for velocity and position, IMUs for slope and acceleration, and even visual systems for terrain classification. The fusion of such data enables regression-based and learning-based IPC estimation models, which are especially useful when detailed system parameters are unavailable or vary across deployments.

Data-driven methods such as Support Vector Machines, Multiple Linear Regression, and Deep Neural Networks have been proposed to estimate IPC dynamically in off-road autonomous robots (51). These methods can also support terrain classification and energy prediction under varying mobility profiles (52).

2.4 Energy Modeling in N-Trailer and Robotic Systems

Energy modeling has become a key aspect in the analysis and design of modern robotic and vehicular systems, particularly for platforms operating under strict efficiency and endurance constraints. In the case of articulated vehicles such as N-Trailer systems, energy-aware formulations are not only necessary for evaluating instantaneous power consumption but also for understanding how terrain conditions, payload, and motion strategies influence overall system performance. Previous research has proposed different approaches to estimate the energetic cost of motion in mobile robots, ranging from analytical models based on friction and resistive forces to data-driven strategies that employ learning algorithms. However, most contributions in the literature focus either on single-body vehicles or simplified trailer configurations, leaving a gap in the integration of accurate energy models with advanced control strategies for generalized N-Trailer systems. Addressing this gap is particularly relevant for applications in agriculture, mining, and autonomous logistics, where energy-efficient operation directly impacts productivity and sustainability.

2.4.1 Instantaneous Power Consumption in Single-Body Robots and Vehicles

As detailed in Section 2.3.1, the estimation of instantaneous power consumption (IPC) in electric vehicles considers aerodynamic drag, hill-climbing resistance, rolling resistance, and inertial forces. For single-body platforms, this modeling framework can be directly applied with high precision, since the mass distribution, geometric configuration, and operating conditions tend to remain constant and are well characterized.

These conditions enable not only the use of simplified dynamic models, but also the integration of the powertrain efficiency maps described in Section 2.3.4, allowing accurate predictions of energy demand and autonomy under various operational profiles.

However, this direct applicability is strongly dependent on the assumption of structural homogeneity and the absence of internal dynamic couplings, which limits the extension of these models to more complex platforms, such as multi-axle articulated systems or agricultural vehicles with multiple load modules. This limitation motivates the development of more robust energy models, as discussed in the following sections.

2.4.2 Limitations of Existing Models in Articulated Configurations

Conventional energy models exhibit significant limitations when applied to articulated platforms such as N-Trailer systems. These configurations present complex coupled dynamics between the tractor and the trailers, including mass redistribution, variable articulation angles, and high-curvature trajectories. All of these generate internal forces that single-body models cannot accurately capture (53).

In addition, articulated systems face specific challenges in regenerative braking modeling, since energy recovery strategies cannot be uniformly applied across the convoy. This complicates the estimation of total energy consumption, especially when load distribution varies between modules or the topography changes over time.

2.4.3 Terrain-Aware Power Modeling Approaches

Energy modeling in unstructured environments requires the explicit consideration of soil properties and their interaction with each segment of the system. In off-road conditions, terrain type, moisture content, and compaction directly affect rolling resistance, slippage, and the power required to sustain motion.

As discussed in Section 2.2.4, the use of dynamic friction models such as LuGre allows for an effective representation of these interactions. For articulated vehicles, this approach can be extended to multiple wheels distributed across different segments, enabling the estimation of additional frictional losses and load imbalances.

Recent approaches incorporate geospatial data, wheel pressure sensors, and digital terrain maps to dynamically adjust the model parameters according to local conditions, significantly improving the accuracy of IPC computation compared to homogeneous terrain models (54; 55).

2.5 Previous Work by the Author

In this section, previous studies and contributions related to both the modeling and control of N-Trailer systems, as well as to the computation of power in electric vehicles, are presented. The reviewed works cover a wide range of approaches, from kinematic and dynamic formulations for representing articulated vehicles with multiple trailers, to control methodologies aimed at improving stability and performance under realistic operating conditions.

Likewise, prior research concerning energy consumption and instantaneous power estimation in electric platforms is included, since this aspect is fundamental for applications in agricultural, mining, and autonomous transportation scenarios.

This overview provides the necessary context to situate the present research within an established body of knowledge, while also highlighting existing gaps in the literature. In particular, the integration of energy-based models with robust control strategies in non-ideal environments, as well as the experimental validation in full-scale vehicles, remain as open challenges that this work seeks to address.

2.5.1 Robust control strategy for generalized N-trailer vehicles based on a dual-stage disturbance observer

Articulated vehicles, such as generalized N-trailers (GNTs), have various applications. The motion control problem has been widely addressed in the literature; however, most reported solutions are theoretical, developed in simulations, or tested under laboratory conditions. In real-world scenarios, these systems are subject to multiple challenges, including slippage, noise, and low-accuracy sensors, which often result in degraded performance.

In this context, the contribution presented in (56) reports the use of Active Disturbance Rejection Control (ADRC) with a Dual-Stage Disturbance Observer (DS-DO) to improve the backward trajectory-tracking performance of a GNT under non-ideal conditions, specifically compensating for propagation errors. The proposed ADRC+DS-DO scheme is illustrated in Fig. 2.8.

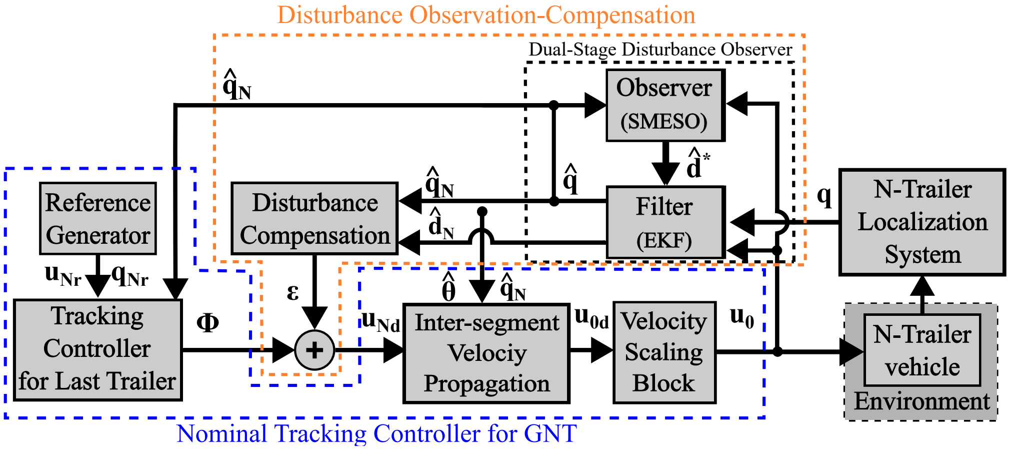

Figure 2.8: Proposed ADRC with dual-stage disturbance observer.

2.5.1.1 Nominal Kinematics of a Generalized N-Trailer

Fig. 2.9 shows a Generalized N-Trailer (GNT) with interlaced on-axle and off-axle hitching. In this particular configuration, the combination of two consecutive trailer segments is referred to as a full trailer (dolly + semi-trailer).

The GNT shown can be interpreted as a chain of N unicycle-like trailers, as well as $N/2$ full trailers. Following the works in (57) and under the rolling-without-slipping assumption, a generic and scalable kinematic model for an arbitrary number of trailers can be derived by considering each i^{th} trailer segment as a unicycle:

$$\dot{\boldsymbol{q}}_i = \begin{bmatrix} \dot{\boldsymbol{p}}_i \\ \dot{\theta}_i \end{bmatrix} = \begin{bmatrix} \dot{x}_i \\ \dot{y}_i \\ \dot{\theta}_i \end{bmatrix} = \begin{bmatrix} 0 & \cos\theta_i \\ 0 & \sin\theta_i \\ 1 & 0 \end{bmatrix} \begin{bmatrix} \omega_i \\ v_i \end{bmatrix} = \boldsymbol{G}(\boldsymbol{q}_i)\boldsymbol{u}_i, \tag{2.9}$$

where $\boldsymbol{p}_i = [x_i \ y_i]^\top$ denotes the position of the axle midpoint of the i^{th} segment, θ_i is its orientation angle, and ω_i, v_i are its angular and longitudinal velocities, respectively. The relation between the velocity of the i^{th} segment $\boldsymbol{u}_i = [\omega_i \ v_i]^\top$ and the velocity of its preceding segment is given by:

$$\boldsymbol{u}_i = \begin{bmatrix} -\frac{L_{hi}}{L_i}\cos\beta_i & \frac{1}{L_i}\sin\beta_i \\ L_{hi}\sin\beta_i & \cos\beta_i \end{bmatrix} \boldsymbol{u}_{i-1} = \boldsymbol{J}_i(\beta_i)\boldsymbol{u}_{i-1} \tag{2.10}$$

where $L_i > 0$ is the i^{th} trailer length, L_{hi} is the i^{th} hitching offset, $\beta_i \triangleq \theta_{i-1} - \theta_i$ is the i^{th} joint angle, and $\boldsymbol{J}_i$ is a transformation matrix, invertible for any β_i if $L_{hi} \neq 0$.

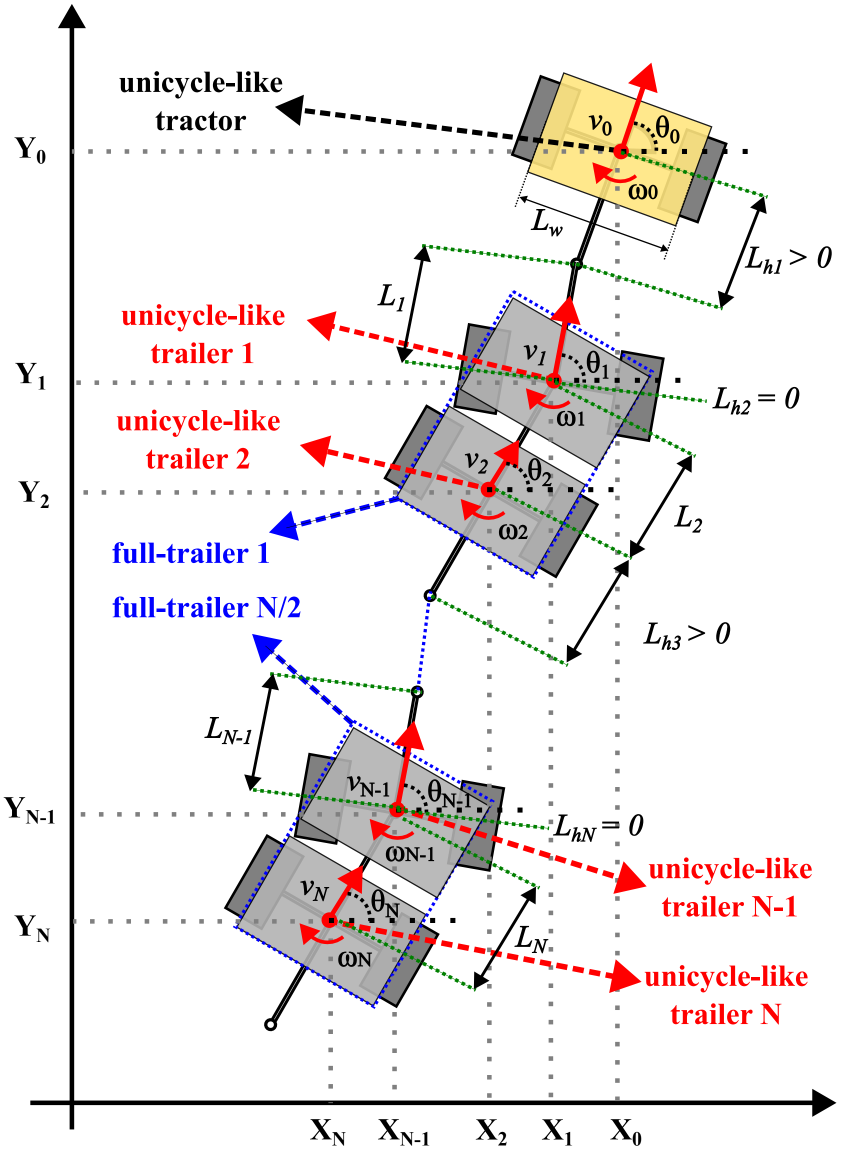

Figure 2.9: Kinematic structure of a typical GNT with interlaced on-axle and off-axle hitching.

Thus, the complete state of the N-Trailer system at any given time can be represented by the vector:

$$\boldsymbol{q} \triangleq [\underbrace{x_N\; y_N\; \theta_N}_{\boldsymbol{q}_N}\; \underbrace{\theta_{N-1} \cdots\; \theta_0}_{\boldsymbol{\theta}}]^\top \in \mathbb{R}^{N+3} \tag{2.11}$$

where the vector $\boldsymbol{\theta} \in \mathbb{R}^N$ contains the orientation of each i^{th} segment for $i \in \{0, \cdots, N-1\}$, and $\boldsymbol{q}_N$ denotes the posture of the last trailer, chosen as the guidance segment for motion control purposes. Consequently, a generic and scalable kinematic model of an N-Trailer can be expressed as:

$$\dot{\boldsymbol{q}} = \begin{bmatrix} \dot{\boldsymbol{q}}_N \\ \dot{\boldsymbol{\theta}} \end{bmatrix} = \begin{bmatrix} \boldsymbol{S}_{TN} \\ \boldsymbol{S}_{\theta} \end{bmatrix} \boldsymbol{u}_0 = \boldsymbol{S}(\boldsymbol{q})\boldsymbol{u}_0 \tag{2.12}$$

where,

$$\boldsymbol{S}_{TN} = \begin{bmatrix} \boldsymbol{S}_1 \\ \boldsymbol{S}_2 \\ \boldsymbol{S}_3 \end{bmatrix} \triangleq \boldsymbol{G}(\boldsymbol{q}_N) \prod_{i=N}^{1} \boldsymbol{J}_i(\beta_i), \tag{2.13}$$

$$\boldsymbol{S}_{\theta} = \begin{bmatrix} \boldsymbol{S}_4 \\ \boldsymbol{S}_5 \\ \vdots \\ \boldsymbol{S}_{N+2} \\ \boldsymbol{S}_{N+3} \end{bmatrix} \triangleq \begin{bmatrix} \boldsymbol{c}^{\top} \prod_{i=N-1}^{1} \boldsymbol{J}_i(\beta_i) \\ \boldsymbol{c}^{\top} \prod_{i=N-2}^{1} \boldsymbol{J}_i(\beta_i) \\ \vdots \\ \boldsymbol{c}^{\top} \boldsymbol{J}_1(\beta_1) \\ \boldsymbol{c}^{\top} \end{bmatrix}, \ \boldsymbol{c}^{\top} \triangleq [1\ 0] \tag{2.14}$$

The system input in (2.12), denoted by $\boldsymbol{u}_0$, corresponds to the velocity vector of the tractor, which is the only actively driven segment in the chain.

2.5.1.2 Trajectory-Tracking Control for Nominal Kinematics

In this work, we adopt the cascade control methodology presented in (1) as the nominal kinematic controller, due to its scalability and modularity. The control problem and the nominal controller are described below.

2.5.1.3 Nominal Control Problem Formulation

Consider a desired time-varying reference trajectory $\boldsymbol{q}_{Nr}(t) = [x_{Nr}(t)\ y_{Nr}(t)\ \theta_{Nr}(t)]^{\top}$, which for all $t \geq 0$ satisfies the unicycle kinematics:

$$\dot{\boldsymbol{q}}_{Nr}(t) = \boldsymbol{G}(\boldsymbol{q}_{Nr}(t))\boldsymbol{u}_{Nr}(t) \in \mathbb{R}^3, \tag{2.15}$$

where $\boldsymbol{u}_{Nr}(t) = [\omega_{Nr}(t)\ v_{Nr}(t)]^{\top}$ denotes the reference velocity vector. In this work, we focus on the backward motion of N-Trailer systems, i.e., $v_{Nr}(t) < 0$ for all $t \geq 0$. The goal of the trajectory-tracking task is to minimize the tracking error of the last trailer (the guidance segment), defined as $\boldsymbol{e}_N(t) = [e_x(t)\ e_y(t)\ e_{\theta}(t)]^{\top}$, such that

$$\limsup_{t \to \infty} \| \boldsymbol{e}_N(t) \| \leq \delta_e, \tag{2.16}$$

where $\delta_e \geq 0$ is an arbitrarily small bound, and the guidance error is given by

$$\boldsymbol{e}_N(t) \triangleq \boldsymbol{q}_{Nr}(t) - \boldsymbol{q}_N(t). \tag{2.17}$$

To achieve this, the modular structure of the nominal control framework allows the integration of any existing control law designed for unicycle-type vehicles. Accordingly, the control function is denoted by $\boldsymbol{\Phi}(\boldsymbol{e}_N, t) = [\Phi_{\omega}(\boldsymbol{e}_N, t)\ \Phi_{v}(\boldsymbol{e}_N, t)]^{\top}$, which must be chosen so that, by setting $\boldsymbol{u}_N(t) := \boldsymbol{\Phi}(\boldsymbol{e}_N, t)$ in (2.9) (for $i = N$), the condition in (2.16) is satisfied for all $t \geq 0$, ideally with $\delta_e = 0$.

2.5.1.4 Inter-Segment Velocity Propagation

Since the control function $\boldsymbol{\Phi}(\boldsymbol{e}_N, t)$ defines the desired velocity of the last trailer, this velocity must be propagated along the vehicular chain in order to compute the corresponding desired velocity of the tractor. This is expressed as

$$\boldsymbol{u}_{0d}(t) = \prod_{i=1}^{N} \boldsymbol{J}_i^{-1}(\beta_i)\boldsymbol{\Phi}(\boldsymbol{e}_N, t), \tag{2.18}$$

where $\boldsymbol{J}_i^{-1}$ denotes the inverse of the transformation matrix $\boldsymbol{J}_i$ in (2.10). The propagation law in (2.18) is directly scalable to an arbitrary number of trailers; however, it is only valid for configurations with off-axle hitches, since $\boldsymbol{J}_i$ becomes non-invertible when $L_{hi} = 0$. To address this limitation, the velocity mapping must be reformulated by introducing an approximate version of $\boldsymbol{J}_i^{-1}$. Following the methodology in previous studies (58; 59), the trajectory-tracking control scheme for a generalized N-Trailer (under nominal conditions) can be summarized in three steps:

S1: Compute the desired velocities of the last trailer as

$$\omega_{Nd}(t) := \Phi_\omega(\boldsymbol{e}_N, t), \quad v_{Nd}(t) := \Phi_v(\boldsymbol{e}_N, t). \tag{2.19}$$

S2: Propagate the desired velocities $\boldsymbol{u}_{id} = [\omega_{id}\ v_{id}]^\top$ through the chain (omitting t for compactness):

$$\omega_{i-1d} = \begin{cases} \dfrac{v_{id}}{L_{hi}} \sin\beta_i - \dfrac{L_i}{L_{hi}}\omega_{id}\cos\beta_i, & L_{hi} \neq 0, \\ k_i e_{id} + \omega_{id} + \dot{\beta}_{id}, & L_{hi} = 0, \end{cases} \tag{2.20}$$

$$v_{i-1d} = \begin{cases} L_i\omega_{id}\sin\beta_i + v_{id}\cos\beta_i, & L_{hi} \neq 0, \\ \sigma\left|L_i\omega_{id}\sin\beta_i + v_{id}\cos\beta_i\right|, & L_{hi} = 0, \end{cases} \tag{2.21}$$

where $i \in \{0, \ldots, N\}$, $\sigma \in \{-1, +1\}$ is a binary factor determined by the motion direction, and $k_i > 0$ is a tunable gain ensuring convergence of the auxiliary joint-angle error to zero, defined as

$$e_{id} \triangleq \underbrace{\mathrm{Atan2c}(\sigma L_i\omega_{id}, \sigma v_{id})}_{\beta_{id}} - \beta_i, \tag{2.22}$$

with β_{id} representing the desired joint angle of the i^{th} segment. The operator Atan2c$(\cdot,\cdot)$ is a continuous variant of Atan2$(\cdot,\cdot)$. The feed-forward term $\dot{\beta}_{id}$ in (2.20) may be omitted (i.e., $\dot{\beta}_{id} := 0$) when online reconstruction is not feasible due to measurement noise (**?**).

S3: Compute the tractor control inputs as

$$\boldsymbol{u}_0(t) := \frac{\boldsymbol{u}_{0d}(t)}{s(t)}, \quad s(t) \triangleq \max\left\{1,\ \frac{|\omega_R(t)|}{\omega_{max}},\ \frac{|\omega_L(t)|}{\omega_{max}}\right\}, \tag{2.23}$$

$$\begin{bmatrix}\omega_R(t)\\ \omega_L(t)\end{bmatrix} = \begin{bmatrix}L_w/2r & 1/r\\ -L_w/2r & 1/r\end{bmatrix}\boldsymbol{u}_{0d}(t), \tag{2.24}$$

where $s(t) \geq 1$ is a scaling factor that guarantees satisfaction of the physical limitations of the tractor, such that $\forall t \geq 0$, $|\omega_R(t)|, |\omega_L(t)| \leq \omega_{max}$ (60). Here, ω_R and ω_L are the desired wheel velocities, ω_{max} is the maximum admissible wheel speed, while r and L_w denote the wheel radius and tractor wheelbase, respectively.

2.5.1.5 N-Trailer Localization System

In outdoor conditions, degradation of control performance is inevitable due to measurement noise and the limited quality of onboard sensors. Therefore, sensing and localization systems are essential to achieve control performance comparable to that expected under nominal conditions. In the literature, localization strategies for articulated vehicles can generally be divided into two main approaches:

A1: Laboratory-scale experiments in controlled environments, where the full vehicular configuration $\boldsymbol{q}$ is obtained using external RGB cameras (61; 62). Since this approach is designed for indoor navigation, cameras can be strategically mounted above the testing area, ensuring all vehicular segments remain visible at all times. Under this exteroceptive methodology, the posture of each segment is estimated independently of the others, meaning that no cumulative error propagates along the vehicular chain.

A2: Real-scale deployments, where the tractor configuration $\boldsymbol{q}_0 = [\boldsymbol{p}_0^\top\ \theta_0]^\top$ is obtained by sensor fusion of odometry, Inertial Measurement Unit (IMU), and Global Navigation Satellite System (GNSS) data. The position of the i^{th} segment is then computed as

$$\boldsymbol{p}_i = \boldsymbol{p}_0 - \begin{bmatrix}\sum_{k=1}^{i}\left(L_k\cos\theta_k + L_{hk}\cos\theta_{k-1}\right)\\ \sum_{k=1}^{i}\left(L_k\sin\theta_k + L_{hk}\sin\theta_{k-1}\right)\end{bmatrix}, \tag{2.25}$$

where θ_i, for $i \in \{1, \ldots, N\}$, is estimated using sensors installed on each trailer segment. These sensors may include RGB cameras (63; 64), LiDARs (65; 66), or inter-segment draw-wire displacement sensors (58). Unlike approach **A1**, these proprioceptive methodologies are subject to error propagation: a corrupted measurement or poor estimation in one segment directly affects the accuracy of all subsequent segments along the vehicular chain (43).

In this work, we focus exclusively on proprioceptive estimation strategies (approach **A2**), since exteroceptive methods (**A1**) are impractical for real outdoor applications.

2.5.1.6 N-Trailer Kinematics in the Presence of Disturbances

To describe a more realistic representation than the ideal model in (2.12), model uncertainties and unpredictable kinematic effects must be incorporated as disturbances. These are categorized as follows:

D1: *Model uncertainties and measurement errors.* The kinematic model is sensitive to variations in the geometric parameters L_{hi} and L_i, which may arise from fabrication inaccuracies, modeling approximations, or changes over time. Consequently, the parameters employed for control purposes represent only approximate values, expressed as

$$L_i \triangleq \delta_{Li}\hat{L}_i, \quad L_{hi} \triangleq \delta_{Lhi}\hat{L}_{hi}, \tag{2.26}$$

where $\delta_{Li} > 0$ and $\delta_{Lhi} \neq 0$ are unknown factors that quantify the mismatch between the nominal parameters $\hat{L}_i$, $\hat{L}_{hi}$ and their true values (61).

Furthermore, under a proprioceptive localization framework (**A2**), the orientation angles are subject to erroneous or noisy measurements of the form

$$\theta_i := \theta_i + \delta_{\theta i}, \tag{2.27}$$

where $\delta_{\theta i}$ represents an unpredictable measurement error. Substituting (2.27) into (2.25) reveals that the estimated position of the guidance segment $\boldsymbol{p}_N$ accumulates the measurement errors of all preceding segments. For control design, this error propagation can be addressed in a manner similar to parametric uncertainties (43). By substituting (2.26) and (2.27) into the transformation matrix $\boldsymbol{J}_i$, the matrix $\boldsymbol{S}(\boldsymbol{q})$ defined in (2.13)–(2.14) can be expressed as

$$\boldsymbol{S}(\boldsymbol{q}) = \hat{\boldsymbol{S}}(\boldsymbol{q}) + \underbrace{\boldsymbol{\Delta S}_L(\boldsymbol{q}, \boldsymbol{\delta_L}, \boldsymbol{\delta_{Lh}}) + \boldsymbol{\Delta S}_\theta(\boldsymbol{q}, \boldsymbol{\delta_\theta})}_{\boldsymbol{\Delta S}(\boldsymbol{q})}, \tag{2.28}$$

where $\hat{\boldsymbol{S}}(\boldsymbol{q})$ denotes the nominal matrix, $\boldsymbol{\Delta S}_L(\cdot)$ accounts for parametric uncertainties with $\boldsymbol{\delta_L} = [\delta_{L1} \dots \delta_{LN}]^\top$, $\boldsymbol{\delta_{Lh}} = [\delta_{Lh1} \dots \delta_{LhN}]^\top$, and $\boldsymbol{\Delta S}_\theta(\cdot)$ captures the impact of orientation measurement errors $\boldsymbol{\delta_\theta} = [\delta_{\theta 1} \dots \delta_{\theta N}]^\top$.

D2: *Wheel slip.* One of the dominant sources of uncertainty in wheeled robotic systems is wheel slip. Similar to the approach in (57), we assume that slips occur in directions aligned with the system's velocity inputs. Under slip conditions, the kinematics of the i^{th} segment in (2.9) can be rewritten as

$$\dot{\boldsymbol{q}}_i = \boldsymbol{G}(\boldsymbol{q}_i)(\boldsymbol{u}_i + \boldsymbol{\delta}_{S\,i}), \tag{2.29}$$

where $\boldsymbol{\delta}_{S\,i} \in \mathbb{R}^2$ represents unpredictable slip disturbances acting on the i^{th} segment. Aggregating the slip contributions into a single disturbance term, the system input in (2.12) can be expressed as

$$\boldsymbol{u}_0 = \hat{\boldsymbol{u}}_0 + \underbrace{\boldsymbol{\Delta u}_0^S(\boldsymbol{\delta}_S) + \boldsymbol{\Delta u}_0^{on}(\boldsymbol{e}_\beta)}_{\boldsymbol{\Delta u}_0}, \tag{2.30}$$

where $\hat{\boldsymbol{u}}_0$ is the nominal tractor input, $\boldsymbol{\Delta u}_0^S$ corresponds to the cumulative effect of wheel slip, with $\boldsymbol{\delta_S} = [\delta_{S\,0} \dots \delta_{S\,N}]^\top$, and $\boldsymbol{\Delta u}_0^{on}(\boldsymbol{e}_\beta)$ captures additional uncertainties introduced by the velocity propagation along on-axle hitches (see **S2**). The mismatch between desired and actual velocity propagation is strongly dependent on the tuning of the gains k_i and, therefore, on the convergence of the auxiliary joint-angle errors $\boldsymbol{e}_\beta = [e_{2d} \; \dots \; e_{id} \; \dots \; e_{Nd}]^\top \in \mathbb{R}^M$, where i takes only even values in $2 < i < N$ (as defined by the GNT structure in Fig. 2.9) and M is the number of on-axle hitches in the vehicular chain.

2.5.1.7 Robust Control Strategy

The disturbances described in Subsection 2.5.1.6 are the primary cause of performance degradation under uncertainty. Consequently, the nominal controller presented in Subsection 2.5.1.2 must be enhanced to explicitly compensate for these effects. To this end, an Active Disturbance Rejection Control (ADRC) scheme is adopted to robustify the nominal controller.

The fundamental principle of ADRC is to group all unmodeled dynamics and uncertainties into a single *total disturbance*, which is then estimated and compensated online using an Extended State Observer (ESO)-based structure (67).

By incorporating the disturbances defined in (2.28) and (2.30) into the nominal kinematic model (2.12), the generalized kinematics of the GNT system can be written as

$$\dot{\boldsymbol{q}} = \hat{\boldsymbol{S}}(\boldsymbol{q})\hat{\boldsymbol{u}}_0 + \boldsymbol{d}, \tag{2.31}$$

where $\boldsymbol{d} \in \mathbb{R}^{N+3}$ denotes the total disturbance, given by

$$\boldsymbol{d} = \begin{bmatrix} \boldsymbol{d}_N \\ \boldsymbol{d}_\theta \end{bmatrix} \triangleq \boldsymbol{\Delta S}\hat{\boldsymbol{u}}_0 + \hat{\boldsymbol{S}}(\boldsymbol{q})\boldsymbol{\Delta u}_0 + \boldsymbol{\Delta S}(\boldsymbol{q})\boldsymbol{\Delta u}_0. \tag{2.32}$$

The proposed control framework, illustrated in Fig. 2.8, introduces a dual-stage disturbance observer to replace the standard ESO, thereby reducing the impact of noise and sensor inaccuracies on the disturbance estimation loop. The disturbance observation–compensation block can be divided into two functional modules.

2.5.1.8 Disturbance Compensation

Equation (2.31) defines the full-chain kinematics of the GNT system. However, for control design, only the guidance error $\boldsymbol{e}_N$ associated with the last trailer is relevant. A disturbed version of (2.9) for $i = N$ is therefore introduced:

$$\dot{\boldsymbol{q}}_N = \boldsymbol{G}(\boldsymbol{q}_N)\boldsymbol{\Gamma} + \boldsymbol{d}_N, \tag{2.33}$$

where $\boldsymbol{d}_N \in \mathbb{R}^3$ represents disturbances affecting the last trailer, and $\boldsymbol{\Gamma} \in \mathbb{R}^2$ is a new control input to be designed.

Under nominal conditions, substituting $\boldsymbol{u}_N(t) := \boldsymbol{\Phi}(\boldsymbol{e}_N, t)$ into (2.9) for $i = N$ ensures perfect trajectory tracking, i.e., $\boldsymbol{e}_N(t) = 0$. Following the derivation in (61), comparison of the nominal kinematics $\dot{\boldsymbol{q}}_N = \boldsymbol{G}(\boldsymbol{q}_N)\boldsymbol{\Phi}(\boldsymbol{e}_N, t)$ with the disturbed model (2.33) yields

$$\boldsymbol{G}(\boldsymbol{q}_N)\boldsymbol{\Gamma} + \boldsymbol{d}_N = \boldsymbol{G}(\boldsymbol{q}_N)\boldsymbol{\Phi}(\boldsymbol{e}_N, t). \tag{2.34}$$

Since $\boldsymbol{G}^\top(\boldsymbol{q}_N)\boldsymbol{G}(\boldsymbol{q}_N) = \boldsymbol{I}_{2\times 2}$ holds for all $\boldsymbol{q}_N$, the control function $\boldsymbol{\Gamma}$ can be obtained as

$$\boldsymbol{\Gamma}(\boldsymbol{e}_N, \hat{\boldsymbol{q}}_N, \hat{\boldsymbol{d}}_N, t) = \boldsymbol{\Phi}(\boldsymbol{e}_N, t) - \underbrace{\boldsymbol{G}^\top(\hat{\boldsymbol{q}}_N)\hat{\boldsymbol{d}}_N}_{\boldsymbol{\varepsilon}(\hat{\boldsymbol{q}}_N, \hat{\boldsymbol{d}}_N)}, \tag{2.35}$$

where $\varepsilon(\hat{\boldsymbol{q}}_N, \hat{\boldsymbol{d}}_N)$ serves as a compensation term. The estimates $\hat{\boldsymbol{d}}_N$ and $\hat{\boldsymbol{q}}_N$ are provided by the Dual-Stage Disturbance Observer (DS-DO), described in Subsection 2.5.1.9.

Accordingly, the desired velocities of the last trailer are computed by replacing $\boldsymbol{q}_N(t) := \hat{\boldsymbol{q}}_N(t)$ in (2.17) and setting $\boldsymbol{u}_{Nd} := \boldsymbol{\Gamma}(\boldsymbol{e}_N, \hat{\boldsymbol{q}}_N, \hat{\boldsymbol{d}}_N, t)$ in (2.19). Then, steps **S2** and **S3** can be applied to propagate the velocities and compute the tractor control inputs, using the nominal parameters $L_i := \hat{L}_i$, $L_{hi} := \hat{L}_{hi}$ and the reconstructed angles $\beta_i := \hat{\theta}_{i-1} - \hat{\theta}_i$, for $i \in \{1, \cdots, N\}$, where $\hat{\theta}_i$ are obtained from the DS-DO.

Differentiating (2.17) with respect to time and substituting (2.33) and (2.35) yields the guidance error dynamics:

$$\dot{\boldsymbol{e}}_N = \boldsymbol{\phi}(\boldsymbol{e}_N, t) + \boldsymbol{\kappa}(\boldsymbol{e}_N, \boldsymbol{e}_d, t), \tag{2.36}$$

where $\boldsymbol{\phi}(\boldsymbol{e}_N, t)$ is a nominal term dependent on the chosen $\boldsymbol{\Phi}(\boldsymbol{e}_N, t)$, and $\boldsymbol{\kappa}(\boldsymbol{e}_N, \boldsymbol{e}_d, t)$ is a perturbation term proportional to the disturbance observation error

$$\boldsymbol{e}_d(t) \triangleq \boldsymbol{d}_N(t) - \hat{\boldsymbol{d}}_N(t). \tag{2.37}$$

It is important to highlight that the disturbance observer is the key component of the ADRC structure: the precision of the online disturbance reconstruction directly determines the robustness of the closed-loop system (68). Full disturbance compensation is achievable if the reconstruction error satisfies

$$\limsup_{t\to\infty} \| \boldsymbol{e}_d(t) \| \leq \delta_d, \tag{2.38}$$

where δ_d is an arbitrarily small nonnegative bound.

2.5.1.9 Dual-Stage Disturbance Observer

The basic idea of the disturbance observer in ADRC is to estimate the non-measurable total disturbances by use an augmented state-space model that includes $\boldsymbol{d}$ as an additional state. In a standard ADRC scheme, the reconstruction of $\boldsymbol{d}$ is generally done by using a conventional Linear Extended State Observer (LESO) as was implemented in (61). However, the LESO is a high-gain technique, which means that it can dangerously amplify the measurement noise. Thus, if the measurement noise is sufficiently large, the corrupted estimates of $\boldsymbol{d}$ may even destabilize the closed-loop system (68). In this context, this work presents a methodology which partially decouples the measurement imprecision from the observer, thus improving the estimation convergence in order to satisfy the condition in (2.38). The proposed disturbance observer methodology consist of two stages which combine a deterministic observer with a stochastic filter as follows:

DS1: The LESO of the standard ADRC is replaced by a nonlinear observer designed by the sliding mode technique. The observer used is the Sliding Mode Extended State Observer (SMESO) which was originally proposed in (69). The SMESO can be treated as an extension of the LESO with a chattering reduction feature. For observer design purposes, the vectors $\boldsymbol{q}$ and $\boldsymbol{d}$ are expressed as:

$$\boldsymbol{q} = [q_1\ q_2\ \dots\ q_{N+2}\ q_{N+3}]^\top \in \mathbb{R}^{N+3}, \tag{2.39}$$

$$\boldsymbol{d} = [d_1\ d_2\ \dots\ d_{N+2}\ d_{N+3}]^\top \in \mathbb{R}^{N+3} \tag{2.40}$$

Then, using the notation in (2.39) and (2.40), the SMESO is implemented in the form of $N+3$ parallel observers where for every $i \in \{1, \cdots, N+3\}$, one defines the so-called extended state as follows:

$$\boldsymbol{x}_i = [x_{1,i}\ x_{2,i}]^\top \triangleq [q_i\ d_i]^\top \in \mathbb{R}^2, \tag{2.41}$$

where $x_{1,i}$ is the only measurable state. Then, recalling (2.31), one can write the extended state dynamics and the output equation as follows:

$$\dot{\boldsymbol{x}}_i = \underbrace{\begin{bmatrix} 0 & 1 \\ 0 & 0 \end{bmatrix}}_{\boldsymbol{A}_i} \boldsymbol{x}_i + \underbrace{\begin{bmatrix} \hat{\boldsymbol{S}}_i(\boldsymbol{q}) \\ \boldsymbol{0}_{1\times 2} \end{bmatrix}}_{\boldsymbol{B}_i(\boldsymbol{q})} \hat{\boldsymbol{u}}_0 + \begin{bmatrix} 0 \\ 1 \end{bmatrix} \dot{d}_i \tag{2.42}$$

$$y_i = \underbrace{\begin{bmatrix} 1 & 0 \end{bmatrix}}_{\boldsymbol{C}_i = \boldsymbol{c}^\top} \boldsymbol{x}_i \tag{2.43}$$

where $\boldsymbol{0}_{1\times 2}$ denotes a zero matrix with dimensions 1×2, and $\hat{\boldsymbol{S}}_i$ is a nominal version of vectors $\boldsymbol{S}_i$ defined in (2.13)-(2.14). Thus, based on this augmented model, the following SMESO is proposed:

$$\dot{\hat{\boldsymbol{x}}}_i = \boldsymbol{A}_i \hat{\boldsymbol{x}}_i + \boldsymbol{B}_i(\hat{\boldsymbol{q}}) \hat{\boldsymbol{u}}_0 + \boldsymbol{l}_i \boldsymbol{k}_i(e_i) e_i, \tag{2.44}$$

$$\boldsymbol{k}_i(e_i) = K_{\alpha i} |e_i|^{\alpha_i - 1} + K_{\gamma i} |e_i|^{\gamma_i}, \tag{2.45}$$

$$e_i = y_i - \boldsymbol{C}_i \hat{x}_i, \tag{2.46}$$

where $\hat{\boldsymbol{x}}_i$ is an estimate of the ith extended state, $\hat{\boldsymbol{u}}_0$ is the tractor control input computed by (2.23) (with the methodology explained in Subsection 2.5.1.8, $\boldsymbol{l}_i = [l_{1,i}\ l_{2,i}]^\top \in \mathbb{R}^2$ is a gain vector selected to make the matrix $\boldsymbol{A}_i - \boldsymbol{l}_i \boldsymbol{C}_i$ Hurwitz (70), $K_{\alpha i}$, $K_{\gamma i}$, α_i, $\gamma_i \neq 0$ are design parameters, and the measurement y_i corresponds to the ith-component of the vector $\hat{\boldsymbol{q}}$ defined in (2.57).

The computation of (2.44)-(2.46) for $i \in \{1, \cdots, N+3\}$ provides a preliminary estimate of $\boldsymbol{d}$:

$$\hat{\boldsymbol{d}}^* \triangleq [\hat{x}_{2,1}\ \hat{x}_{2,2}\ \dots\ \hat{x}_{2,N+2}\ \hat{x}_{2,N+3}]^\top \in \mathbb{R}^{N+3} \tag{2.47}$$

that will be used as a virtual measurement of $\boldsymbol{d}$ in the stochastic stage explained below.

DS2: In order to deal with noisy measurements and since both disturbances and sensor noise usually include random high-frequency signals, a stochastic approach can be used to i) filter the available noisy measurements of $\boldsymbol{q}$ and ii) to improve the estimate $\hat{\boldsymbol{d}}^*$ by considering random dynamics. Thus, the extended state in 2.41 can be augmented with another fictitious state variable representing the time derivative of $\boldsymbol{d}$ as follows:

$$\boldsymbol{x} = [\boldsymbol{x}_1\ \boldsymbol{x}_2\ \boldsymbol{x}_3]^\top \triangleq [\boldsymbol{q}^\top\ \boldsymbol{d}^\top\ \dot{\boldsymbol{d}}^\top]^\top \in \mathbb{R}^{3N+9}, \tag{2.48}$$

where $\boldsymbol{x}_1$ and $\boldsymbol{x}_2$ are assumed to be measurable states. Then, recalling (2.31), one can write the secundary extended state dynamics and the output equation as follows:

$$\dot{\boldsymbol{x}} = \underbrace{\begin{bmatrix} \hat{\boldsymbol{S}}(\boldsymbol{x}_1)\hat{\boldsymbol{u}}_0 \\ \boldsymbol{x}_3 \\ \boldsymbol{0}_{N+3\times 1} \end{bmatrix}}_{\boldsymbol{f}(\boldsymbol{x},\hat{\boldsymbol{u}}_0)} + \boldsymbol{\nu} \tag{2.49}$$

$$\boldsymbol{y} = \underbrace{\begin{bmatrix} \boldsymbol{I}_{2N+6\times 2N+6} & \boldsymbol{0}_{2N+6\times N+3} \end{bmatrix} \boldsymbol{x}}_{\boldsymbol{h}(\boldsymbol{x})} + \boldsymbol{\mu} \tag{2.50}$$

where $\boldsymbol{\nu}$, $\boldsymbol{\mu} \in \mathbb{R}^{N+3}$ are assumed to be zero-mean multivariate Gaussian noises with covariance $\boldsymbol{Q} \in \mathbb{R}^{3N+9\times 3N+9}$ and $\boldsymbol{R} \in \mathbb{R}^{2N+6\times 2N+6}$ respectively. Thus, inspired in the works (71), the well-known Extended Kalman Filter (EKF) is proposed as an observer where the prediction/update equations can be obtained by discretizing the secondary augmented model in (2.49)-(2.50) using the Euler method:

$$\hat{\boldsymbol{x}}^-(n) = \boldsymbol{f}(\hat{\boldsymbol{x}}(n-1), \hat{\boldsymbol{u}}_0(n)), \tag{2.51}$$

$$\boldsymbol{P}^-(n) = \boldsymbol{F}(n)\boldsymbol{P}(n-1)\boldsymbol{F}^\top(n) + \boldsymbol{Q} \tag{2.52}$$

$$\boldsymbol{K}(n) = \boldsymbol{P}(n)\boldsymbol{H}^\top(n)\left[\boldsymbol{H}(n)\boldsymbol{P}^-(n)\boldsymbol{H}^\top(n) + \boldsymbol{R}\right]^{-1} \tag{2.53}$$

$$\hat{\boldsymbol{x}}(n) = \hat{\boldsymbol{x}}^-(n) + \boldsymbol{K}(n)\left[\boldsymbol{z}(n) - \boldsymbol{h}(\hat{\boldsymbol{x}}^-(n))\right] \tag{2.54}$$

$$\boldsymbol{P}(n) = \left[\boldsymbol{I}_{3N+9\times 3N+9} - \boldsymbol{K}(n)\boldsymbol{H}(n)\right]\boldsymbol{P}^-(n) \tag{2.55}$$

where (2.51)-(2.52) correspond to the prediction process while (2.53)-(2.55) correspond to the update process for $n \in \mathbb{N}$, $\boldsymbol{F} \triangleq \partial\boldsymbol{f}/\partial\boldsymbol{x}|_{\hat{x}}$, $\boldsymbol{H} \triangleq \partial\boldsymbol{h}/\partial\boldsymbol{x}|_{\hat{x}^-}$, and $\boldsymbol{z}$ is a vector which collects the noisy measurements of $\boldsymbol{q}$ and the estimate $\hat{\boldsymbol{d}}^*$ such that $\boldsymbol{z} \triangleq [\boldsymbol{q}^\top\ \hat{\boldsymbol{d}}^{*\top}]^\top \in \mathbb{R}^{2N+6}$. To improve the filter convergence, we propose to modified the covariance matrix $\boldsymbol{P}(n)$ computed in (2.55) by:

$$\boldsymbol{P}(n) := \boldsymbol{P}(n) + (\lambda^{-1} - 1)\boldsymbol{P}(n) \tag{2.56}$$

where $0 < \lambda \leq 1$ is a fading factor which modifies the memory length of the filter in order to improve the filtering dynamic response speed(72). In other words, the recalculation of $\boldsymbol{P}(n)$ in (2.56) makes the filter more responsive to new data and introduces a certain amount of flexibility into the estimation of $\boldsymbol{x}$.

Finally, the computation of (2.51)-(2.56) provides the estimates:

$$\hat{\boldsymbol{d}} = [\hat{\boldsymbol{d}}_N^\top\ \hat{\boldsymbol{d}}_\theta^\top]^\top \triangleq \hat{\boldsymbol{x}}_2, \quad \hat{\boldsymbol{q}} = [\hat{\boldsymbol{q}}_N^\top\ \hat{\boldsymbol{\theta}}^\top]^\top \triangleq \hat{\boldsymbol{x}}_1 \tag{2.57}$$

where $\hat{\boldsymbol{q}}_N$ and $\hat{\boldsymbol{F}}_N$ are used for disturbance compensation in (2.35) while $\hat{\boldsymbol{q}}$ is also used as a filtered version of $\boldsymbol{q}$ for the SMESO as well as for the nominal tracking controller as was indicated in Fig. 2.9.

2.5.1.10 Motion Controller Results

To validate the proposed control strategy, a series of simulation studies were conducted to illustrate the compensation of each disturbance type separately. In addition, real experiments were performed to demonstrate that the approach can be implemented on a full-scale vehicle under non-ideal operating conditions.

Following previous works (73; 74), the control performance was quantitatively assessed using the following discrete-time cumulative cost functions:

$$\Psi_e \triangleq \sum_{n=0}^{\Omega} \eta_v v_0^2(n) + \eta_\omega \omega_0^2(n), \tag{2.58}$$

$$\Psi_u \triangleq \sum_{n=0}^{\Omega} \eta_{xy}(e_x^2(n) + e_y^2(n)) + \eta_\theta e_\theta^2(n), \tag{2.59}$$

where Ψ_e denotes the total tracking error, Ψ_u represents the control effort, Ω is the number of discrete steps required to complete the trajectory, and $\eta_v, \eta_\omega, \eta_\theta, \eta_{xy} > 0$ are weighting coefficients that normalize terms of different physical units. A controller is considered to perform better when both Ψ_e and Ψ_u are minimized.

For all simulations and real experiments, the control function $\boldsymbol{\Phi}(\boldsymbol{e}_N, t)$ introduced in (75) and applied in (61) was adopted. The reference guidance trajectories were generated by time-parametrized functions defined as follows:

- Constant-curvature references: $v_{Nr}(t) = 0.15\sigma$ m/s with $\sigma = -1$, and $\omega_{Nr}(t) \in \{0.04,\ 0.075\}$ rad/s.
- Variable-curvature reference: $v_{Nr}(t) = 0.15\sigma$ m/s with $\sigma = -1$, and $\omega_{Nr}(t) = 0.025 + 0.025\sin(0.075/2\ t)$ rad/s.

The initial posture of the N-Trailer vehicle was set as $\boldsymbol{q}_N(0) = [0\ 0\ \theta_{init}]^\top$, with $\theta_i(0) = \theta_{init}$ for $i \in \{0, \ldots, N-1\}$. For simulations, $\theta_{init} = \pi/2$, while for real experiments, $\theta_{init} = 0$.

2.5.1.11 Numerical Validation

The simulations were done using $N = 4$ for G4T as well as for nS4T to show the scalability and generalization of the approach. The vehicle dimensions used for simulation were

$L_{1,3} = 1.397$m, $L_{2,4} = 0.78$m, $L_{h1,3} = 0.342$m, $L_{h2,4} = 0$m (for G4T case), and $L_{hi} = 0.342$m for $i = \{1, 2, 3, 4\}$ (for nS4T case).

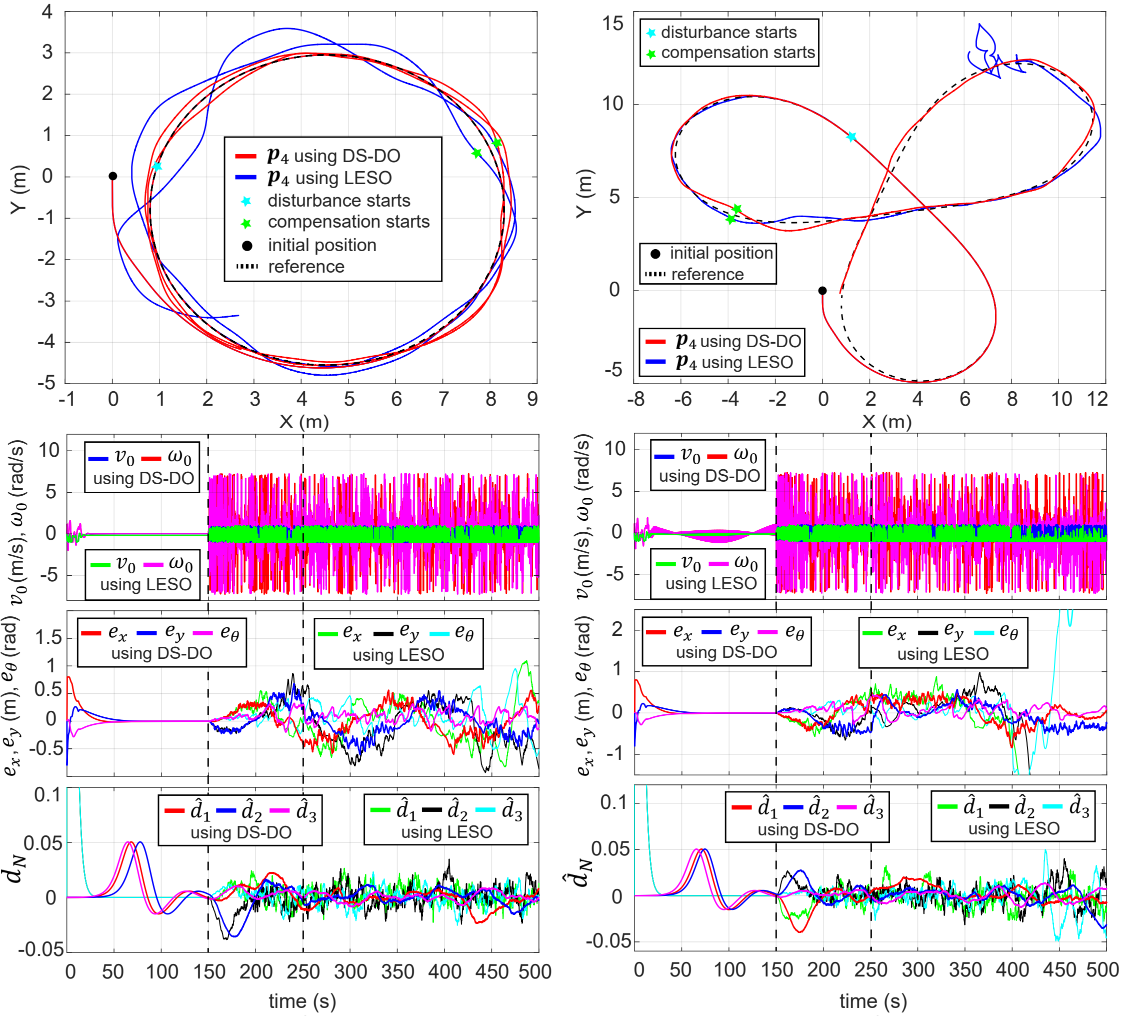

a) b)

Figure 2.10: Tracking results of a G4T vehicle under noisy measurements for a trajectory with (a) constant curvature, (b) variable curvature. Noise is applied at 150s and the compensation is turned on at 250s.

The parameters used to scale the tractor control inputs were $L_w = 0.55$m, $r = 0.165$m, $\omega_{max} = 1/r$ rad/s, and the parameters used to propagate the velocities in the case of G4T were set as $\dot{\beta}_{2,4d} = 0$, $k_2 = 5$, $k_4 = 1$. To reconstruct the total disturbance, the SMESO design parameters were set as $K_{\alpha i} = K_{\gamma i} = 0.1$, $\alpha_i = \gamma_i = 1$, and the gains l_i were tunned using an observer bandwidth $w_0 = 0.3$ rad/s such that $l_{1,i} = 2w_0$, $l_{2,i} = w_0^2$ for $i = \{1, \ldots, 7\}$. The EKF was initialized with $\hat{\boldsymbol{x}}(0) = [\boldsymbol{q}_N(0)^\top \ \boldsymbol{0}_{1\times 14}]^\top$, $\boldsymbol{P}(0) = \mathrm{diag}(P_1, \ldots, P_{21})$ where $P_i = 0.01$, $P_j = 1$ for $i = \{1, \ldots, 7\}$ and $j = \{8, \ldots, 21\}$. The fading factor used was $\lambda = 0.9$ and the covariance matrix were defined as $\boldsymbol{R} = 0.01\ \boldsymbol{I}_{14\times 14}$, $\boldsymbol{Q} = \mathrm{diag}(Q_1, \ldots, Q_{21})$ where $Q_i = 0.01$, $Q_j = 0.1$ for $i = \{1, \ldots, 14\}$ and $j = \{15, \ldots, 21\}$.

Table 2.1 summarizes the results of several simulated examples divided into the different disturbance tested, N-trailer structure used, trajectory tracked, and observer used. For comparison purposes, the standard LESO implemented in (61) was also tested. The LESO was tunned using the same observer bandwidth than SMESO.

For all the simulations, the nominal control was applied to the vehicle during the time interval $0 \leq t < 250$s and the disturbance compensation was applied in the interval $t \geq 250$s. The parametric uncertainties were introduced by consider $\delta_{Li} = \delta_{Lhi} = 0.5$ for $i = \{1, 2, 3, 4\}$. The slipping perturbances were introduced such that $\boldsymbol{\Delta u}_0^S(t) = r_d(t)[0.4\ 0.4]^\top$, where $r_d(t) \in [0, 1]$ is a time-variant gain which is 0 for $t < 150$s, varies from 0 to 1 within the interval $150s \leq t < 200s$ and is 1 for $t \geq 200$s. The noise disturbances were introduced by considering $\delta_{\theta i}(t) = r_d(t)\sigma_\theta$ for $i = \{1, 2, 3, 4\}$, where $\sigma_\theta \in \mathbb{R}$ is a random variable such that $\sigma_\theta \sim \mathcal{N}(0,\ 0.02)$,

The Fig. 2.10 illustrates the results of two specific cases in the Table 2.1, showing the evolution in time of the control inputs, tracking errors, and disturbance estimates. The cases in Fig. 2.10 correspond to a G4T under measurement noise for trajectories with constant curvature (left side) and variable curvature (right side).

Table 2.1: Simulation results using a 4-Trailer vehicle.

Disturbance tested	Structure used	Observer used	Constant curvature		Variable curvature	
			Ψ_e	Ψ_u	Ψ_e	Ψ_u
parametric uncertanties	G4T	DS-DO	182.06	131.63	157.91	145.38
		LESO	182.02	143.77	158.17	1171
	nS4T	DS-DO	108.98	56.37	98.75	5116
		LESO	108.94	57.3	98.55	5160
slip	G4T	DS-DO	221.34	405.66	278.41	468.97
		LESO	222.87	408.48	274.9	473
	nS4T	DS-DO	206.54	407.13	245.11	422.42
		LESO	205.69	413.46	242.78	427.71
noise	G4T	DS-DO	604.48	7355	665.87	7179
		LESO	1363	7489	80770*	6720*
	nS4T	DS-DO	183.03	9275	186.99	8439
		LESO	330.21	10860	259.74	8945

According to the results in Table 2.1, the performance improvement obtained by using DS-DO instead of LESO is most evident under noisy conditions, as illustrated in Fig. 2.10. In scenarios involving parametric uncertainties and wheel slip, the tracking cost Ψ_e is comparable for both observers, with LESO occasionally performing slightly better than DS-DO. Nevertheless, in all tested cases, DS-DO consistently reduced the control effort cost Ψ_u compared to LESO. The only instance where LESO yielded a lower control effort is indicated with $*$, which corresponds to the case where LESO destabilized the closed loop, leading to a collision between trailers (see Fig. 2.10b). In this situation, the control signals after the collision are not meaningful for comparison.

As expected, when $L_{h2,4} = 0$ m (G4T case), the propagation of desired velocities through on-axle hitches resulted in a significant increase in tracking error compared to the case $L_{h2,4} = 0.342$ m (nS4T case), under identical disturbances. This outcome underscores the importance of developing new and effective control strategies for GNTs, since approaches originally designed for nSNTs are not always compatible or may fail to deliver comparable performance when applied to GNTs.

2.5.1.12 Experimental Verification

The proposed approach was experimentally validated using a full-scale G2T vehicle, shown in Fig. 2.11. The active segment (tractor) was a commercial Husky robot with skid-steer locomotion, equipped with an onboard computer running the Robot Operating System (ROS) to synchronize sensor data and send control commands to the motors. Following the localization methodology **A2** (see Subsection 2.5.1.5), the Husky posture $\boldsymbol{q}_0$ was estimated by fusing odometry, IMU, and GNSS measurements. The orientation angles $\theta_{1,2}$ were obtained using incremental rotary encoders mounted at each hitching point (see Fig. 2.11). These encoders, delivering 600 pulses per revolution, were connected to an Arduino Uno board, allowing orientation changes to be detected with a resolution of 0.6°.

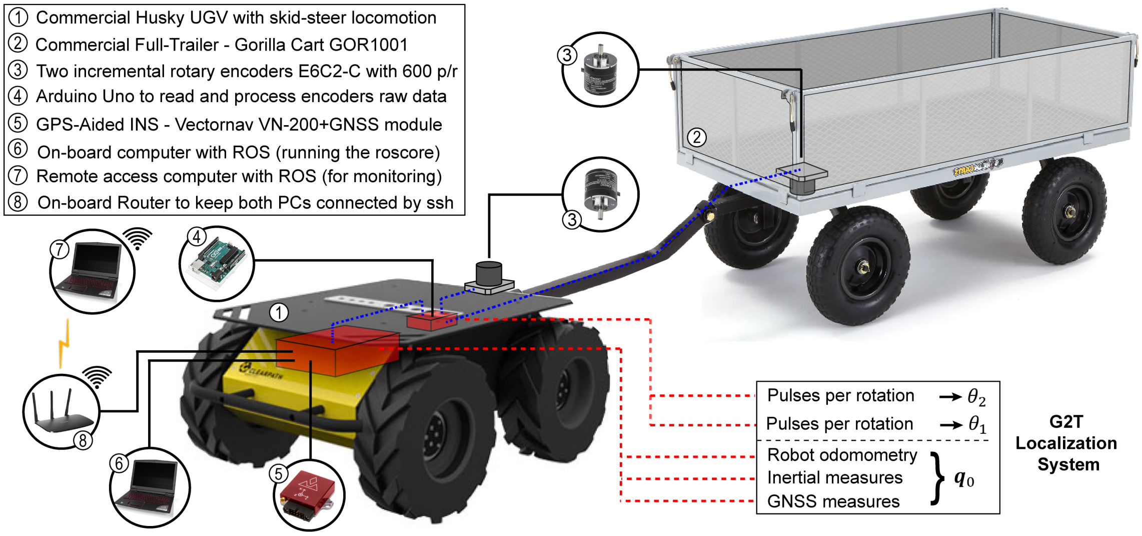

Figure 2.11: Scheme of the G2T vehicle used as experimental platform for the in field tests.

Because the computation of $\boldsymbol{q}_0$ and $\theta_{1,2}$ involves different sampling rates, the onboard computer synchronized all sensor streams and fused them with the G2T kinematics to provide new feedback information every 0.01 s.

The G2T dimensions were consistent with those of the simulated G4T, and most tuning parameters from the simulations were retained for the real experiments. However, the observer parameters were adjusted to $K_{\alpha i} = K_{\gamma i} = \alpha_i = \gamma_i = w_0 = 0.1$ rad/s for $i \in \{1, \ldots, 5\}$, while the EKF covariance matrices were set to $\boldsymbol{R} = 0.01\, \boldsymbol{I}_{10\times 10}$ and $\boldsymbol{Q} = 0.1\, \boldsymbol{I}_{15\times 15}$.

In real implementations, disturbances are always present and cannot be isolated by the user. In particular, wheel slip—intrinsic to skid-steer vehicles such as the Husky—and

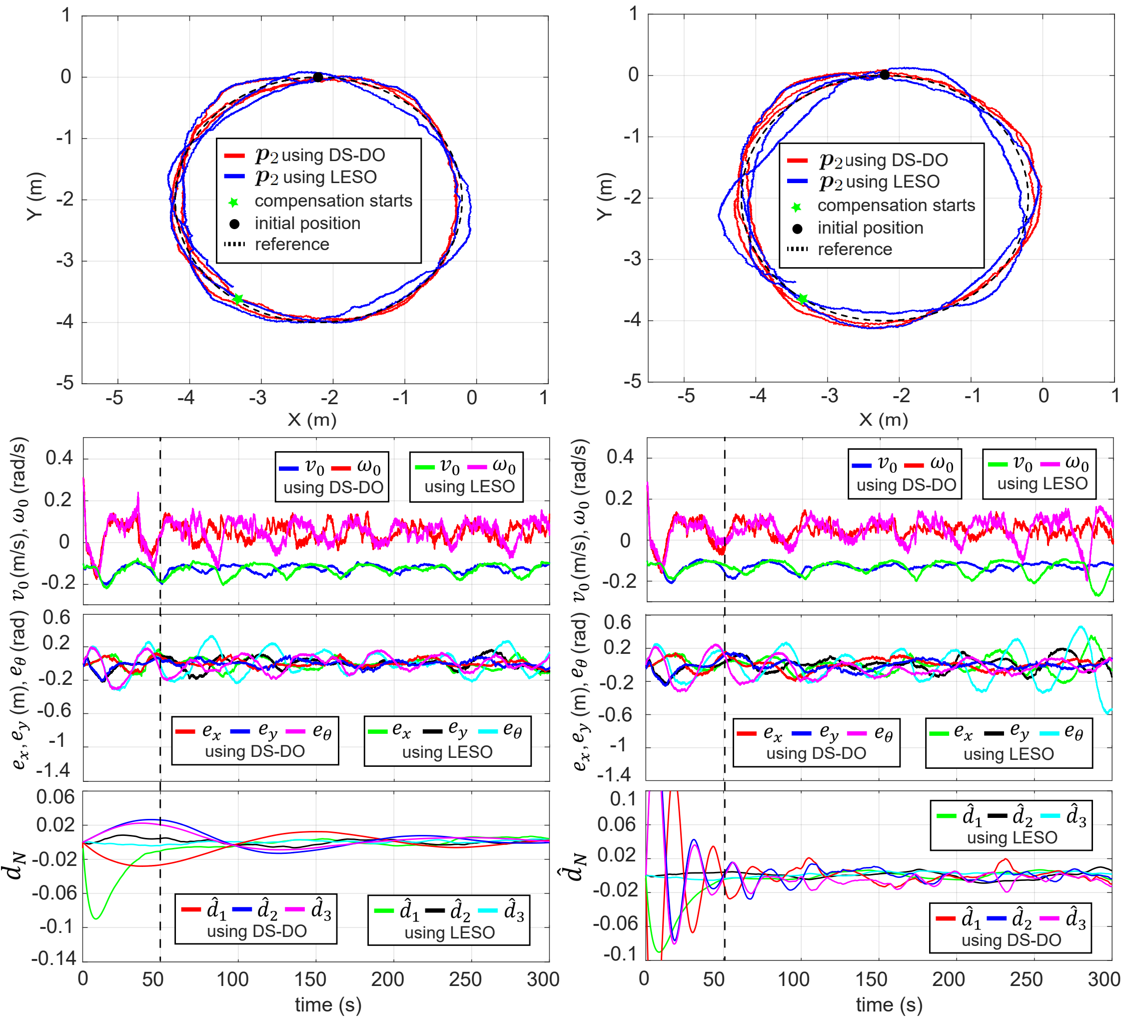

(a) (b)

Figure 2.12: Tracking results of a G2T vehicle on pavement terrain, considering a constant-curvature trajectory of 4 m diameter: (a) without additional disturbances and (b) with parametric uncertainties applied from the initial position. Compensation was activated at $t = 50$ s.

measurement errors occur simultaneously, unlike in the simulations where they could be studied independently. Consequently, in real experiments, multiple disturbances acted concurrently, though in each test a single disturbance type was deliberately amplified.

Table 2.2 summarizes the cost functions obtained from three experiments in which the vehicle tracked a constant-curvature trajectory on pavement terrain. The first experiment was performed without injecting additional disturbances into the feedback loop, the second introduced parametric uncertainties by setting $\delta_{Li} = \delta_{Lhi} = 0.7$ for $i \in \{1, 2\}$, and the third amplified sensor noise by defining $\delta_{\theta i}(t) = r_d(t)\sigma_\theta$ with $\sigma_\theta \sim \mathcal{N}(0,\ 0.03)$ and $r_d(t)$ ramping from 0 to 1 within the interval $0 \leq t < 50$ s. In all experiments, disturbance compensation was activated at $t = 50$ s.

As shown in Table 2.2, and consistent with the simulation results, DS-DO reduced the control effort Ψ_u in every case tested. In terms of tracking accuracy (Ψ_e), DS-DO

Table 2.2: Experimental results using a G2T vehicle.

Experiment	Disturbance Tested	Observer Used	Cost Function	
			Ψ_e	Ψ_u
1st	None	DS-DO	45.282	6.269
		LESO	93.022	7.046
2nd	Parametric Uncertainties	DS-DO	71.533	6.383
		LESO	167.693	7.748
3rd	Noise Amplification	DS-DO	113.49	12.62
		LESO	146.58	15.88

also outperformed LESO. Specifically, in the absence of additional disturbances, DS-DO achieved $\Psi_e = 45.28$ compared to $\Psi_e = 93.02$ with LESO, an improvement of approximately 54%. Under parametric uncertainties, DS-DO reduced Ψ_e by about 57% relative to LESO, while under noise amplification, the improvement was around 22% (reducing Ψ_e from 146.58 to 113.49).

These results are encouraging and confirm that selecting an appropriate disturbance observer is crucial for ensuring that the ADRC scheme compensates for accumulated errors effectively under real-world conditions.

2.5.2 Absolute joint-angle estimation of Generalised N-Trailer vehicles equipped with incremental encoders using moving horizon estimation

The Generalised N-Trailer (GNT) vehicle consists of a tractor pulling an arbitrary number of trailers connected through different hitching configurations. Its kinematics are highly nonlinear, and the increasing number of trailers significantly enlarges the system's complexity. Understanding the GNT kinematics is therefore fundamental, as accurate knowledge of the joint angles between consecutive segments directly influences the vehicle's ability to track trajectories, avoid collisions, and prevent undesired effects such as jackknifing.

In practice, joint-angle information is commonly acquired through rotary encoders. Incremental encoders are attractive because of their low cost, robustness, and ease of integration, but they only measure angles relative to an unknown initial position. Absolute encoders, in contrast, provide global angular measurements but are more expensive and require calibration procedures. For articulated vehicles with multiple trailers, such calibration quickly becomes impractical, highlighting the need for alternative estimation methods.

This leads to the consideration of the joint-angle subsystem as a critical part of the GNT dynamics. Since the joint angles are not directly observable from incremental encoders, the subsystem's observability properties must be exploited to reconstruct absolute angular information. In this context, Moving Horizon Estimation (MHE) provides a suitable framework, as it allows combining system kinematics, noisy measurements, and constraints to estimate the true joint angles.

The contribution of (76) is to compute absolute joint-angle estimates for a GNT vehicle equipped only with incremental encoders, thus avoiding costly calibration steps. A two-stage Nonlinear MHE (NMHE) is proposed: the first stage identifies the unknown initial conditions, while the second maintains an accurate estimate during operation with reduced computational burden. Finally, both simulations and real-scale experiments are carried out to validate the approach and demonstrate its applicability in realistic scenarios.

2.5.2.1 Kinematics of the N-trailer vehicle

As previously described in Subsection 2.5.1.1, the Generalised N-Trailer (GNT) vehicle consists of a tractor pulling an arbitrary number of trailers connected through passive rotary joints. In this work, the tractor is modeled as a differentially driven vehicle (77).

The state vector of the system is defined as

$$\boldsymbol{q}_t = (\beta_{1,t}, \ldots, \beta_{N,t}, \theta_{0,t}, \ldots, \theta_{N,t}, x_{0,t}, y_{0,t}, x_{N,t}, y_{N,t})^\top , \tag{2.60}$$

where $\beta_{i,t}$ denotes the joint angle between segments $i-1$ and i, with $i \in \mathbb{Z}[1, N]$. The attitude of the i^{th} segment is represented by $\theta_{i,t}$, with $i \in \mathbb{Z}[0, N]$, where the index 0 corresponds to the tractor. Thus, the joint angles satisfy

$$\beta_{i,t} = \theta_{i-1,t} - \theta_{i,t}, \quad \dot{\beta}_{i,t} = \omega_{i-1,t} - \omega_{i,t}, \tag{2.61}$$

with $\omega_{i,t}$ being the angular velocity of the i^{th} segment. The Cartesian coordinates $(x_{0,t}, y_{0,t})$ and $(x_{N,t}, y_{N,t})$ describe the positions of the tractor and the last trailer, respectively.

The control actions are given by the tractor's steering rate $\omega_{0,t}$ and longitudinal velocity $v_{0,t}$, such that the control vector is

$$\boldsymbol{u}_t = (\omega_{0,t}, v_{0,t})^\top . \tag{2.62}$$

The kinematic model of the chained system is well established in the literature and can be succinctly expressed as

$$\dot{\boldsymbol{q}}_t = G(\boldsymbol{q}_t)\, \boldsymbol{u}_t, \tag{2.63}$$

for the nominal case, i.e., without considering external disturbances (77).

In practice, it is often assumed that only the attitude and position of the tractor are directly measurable, i.e., $\theta_{0,t}$ and $(x_{0,t}, y_{0,t})$. Hence, for a GNT vehicle equipped with absolute encoders, the output equation is defined as

$$\boldsymbol{r}_t = h(\boldsymbol{q}_t) + \nu_t = (\beta_{1,t}, \ldots, \beta_{N,t}, \theta_{0,t}, x_{0,t}, y_{0,t})^\top + \nu_t, \tag{2.64}$$

where $h : \mathbb{R}^{n_q} \to \mathbb{R}^{n_r}$ is the output function, and $\nu_t \in \mathbb{R}^{n_r}$ represents bounded measurement noise. The complete system dynamics are thus described as

$$\begin{cases} \dot{\boldsymbol{q}}_t = G(\boldsymbol{q}_t)\, \boldsymbol{u}_t + w_t, \\ \boldsymbol{r}_t = (\beta_{1,t}, \ldots, \beta_{N,t}, \theta_{0,t}, x_{0,t}, y_{0,t})^\top + \nu_t, \end{cases} \tag{2.65}$$

where w_t accounts for bounded additive disturbances.

2.5.2.2 N-Trailer Vehicle Equipped with Incremental Encoders

In practice, the joint angles of a Generalised N-Trailer (GNT) vehicle can be measured using incremental encoders mounted at the hitch points between segments. The measurement at joint i and time t is denoted by $\gamma_{i,t}$. The relationship between the incremental encoder measurement $\gamma_{i,t}$ and the true joint angle $\beta_{i,t}$ is given by:

$$\gamma_{i,t} = \beta_{i,t} - \beta_{i,0}, \tag{2.66}$$

where $\beta_{i,0}$ is the unknown initial angle of the i^{th} joint. Thus, incremental encoders provide relative angular measurements, which require further processing to obtain absolute joint angles.

The main objective is to compute an estimation $\hat{\boldsymbol{q}}_t$ of the system state $\boldsymbol{q}_t$ by using the incremental encoder measurements $\gamma_{i,t}$, along with the tractor's attitude $\theta_{0,t}$ and position $(x_{0,t}, y_{0,t})$. Consequently, estimating the initial joint angles $\beta_{i,0}$ becomes a parameter estimation problem that must be solved jointly with the state estimation task.

By modifying the output equation of the system (see Eq. (1)) to include incremental encoder measurements, the following equations describe the system equipped with incremental encoders:

$$\begin{cases} \dot{\boldsymbol{q}}_t = G(\boldsymbol{q}_t)\,\boldsymbol{u}_t + w_t, \\ \rho_t = \begin{pmatrix} \beta_{i,t} \\ \theta_{0,t} \\ x_{0,t} \\ y_{0,t} \end{pmatrix} - \begin{pmatrix} \beta_{i,0} \\ 0 \\ 0 \\ 0 \end{pmatrix} + \nu_t = \begin{pmatrix} \gamma_{i,t} \\ \theta_{0,t} \\ x_{0,t} \\ y_{0,t} \end{pmatrix} + \nu_t, \end{cases} \tag{2.67}$$

where ρ_t denotes the measurement vector, ν_t is bounded measurement noise, and w_t represents bounded process disturbances.

2.5.2.3 Joint Angles Subsystem

To analyze whether the joint angles $\beta_{i,t}$ can be estimated from the incremental encoder measurements $\gamma_{i,t}$, we focus on the subsystem that contains only the joint dynamics $g(\boldsymbol{p}_t)$. The reduced state vector is defined as:

$$\boldsymbol{p}_t := [\beta_{1,t}, \beta_{2,t}, \ldots, \beta_{N,t}]^\top, \tag{2.68}$$

and the subsystem output is:

$$\boldsymbol{s}_t = [\beta_{1,t} - \beta_{1,0},\, \beta_{2,t} - \beta_{2,0},\, \ldots,\, \beta_{N,t} - \beta_{N,0}]^\top = [\gamma_{1,t}, \gamma_{2,t}, \ldots, \gamma_{N,t}]^\top. \tag{2.69}$$

Thus, the subsystem can be expressed as:

$$\begin{cases} \dot{\boldsymbol{p}}_t = g(\boldsymbol{p}_t)\,\boldsymbol{u}_t + w_t, \\ \boldsymbol{s}_t = \begin{pmatrix} \gamma_{1,t} \\ \vdots \\ \gamma_{N,t} \end{pmatrix} + \nu_t, \end{cases} \tag{2.70}$$

where w_t represents bounded process disturbances and v_t denotes bounded measurement noise.

The main goal is to reconstruct the vector $\boldsymbol{p}_t$ from the measurements $\boldsymbol{s}_t$. According to the persistence of excitation theorem (78), the vehicle must be in motion to guarantee state reconstruction. Furthermore, it will be shown that traveling along a short straight line is sufficient to excite the subsystem. Otherwise, if $\theta_{0,t} = 0$, $x_{0,t} = y_{0,t} = 0$, and $\beta_{i,t} \neq 0$, then $\boldsymbol{s}_t = 0$, which corresponds to a non–kernel-free output function for which no observer exists (79).

2.5.2.4 Subsystem's Observability

As introduced in the previous subsection, the reduced joint-angle subsystem (Eq. 2.70) isolates the dynamics of the angles $\beta_{i,t}$ and their corresponding measurements $\gamma_{i,t}$. The next step is to analyze whether this subsystem is observable, i.e., whether the states $\boldsymbol{p}_t$ can be reconstructed from the available outputs $\boldsymbol{s}_t$.

It is important to note that proving the observability of the reduced subsystem implies, in turn, the observability of the complete N-trailer system described in Eq. (3), since the tractor's attitude $\theta_{0,t}$ and position $(x_{0,t}, y_{0,t})$ are assumed to be directly measurable.

To formalize this analysis, we rely on the notion of incrementally input–output-to-state stability (i-IOSS), a concept of detectability for nonlinear systems (**?**).

The subsystem in Eq. (4) is said to be *i-IOSS* if there exist functions $\beta \in KL$ and $\gamma_w, \gamma_v \in K$ such that for each pair of initial conditions $\boldsymbol{p}_0^{(1)}, \boldsymbol{p}_0^{(2)} \in \mathbb{R}^{n_q}$, and for each pair of disturbance sequences $w_t^{(1)}$, $w_t^{(2)}$ and output sequences $\boldsymbol{s}_t^{(1)}$, $\boldsymbol{s}_t^{(2)}$, the following inequality holds:

$$\left|\boldsymbol{p}_t^{(1)} - \boldsymbol{p}_t^{(2)}\right| \leq \beta\left(\left|\boldsymbol{p}_0^{(1)} - \boldsymbol{p}_0^{(2)}\right|, t\right) + \gamma_w\left(\|w_t^{(1)} - w_t^{(2)}\|_{[0,t]}\right) + \gamma_v\left(\|\boldsymbol{s}_t^{(1)} - \boldsymbol{s}_t^{(2)}\|_{[0,t]}\right). \tag{2.71}$$

The following theorem summarizes the first main result regarding the subsystem's observability:

Theorem 1 *The subsystem given by Eq. (4) is incrementally input–output-to-state stable. Consequently, an estimator for the subsystem exists. Moreover, for any two feasible trajectories $\boldsymbol{p}_t^{(1)}$ and $\boldsymbol{p}_t^{(2)}$ with N joints, these trajectories become indistinguishable after the system travels at a constant velocity $v_0 > 0$ and $\omega_0 = 0$ for a time period T satisfying:*

$$T \geq -\frac{L}{v_0 N} \ln\left(\tan\left(\frac{\delta}{2}\right)\right), \tag{2.72}$$

where $\delta \in \mathbb{R}_{>0}$ is a tuning parameter and $L = \max\{L_i\}$, $i \in \mathbb{Z}[1, N]$. Furthermore, the difference $\nabla_t := \left|\boldsymbol{p}_t^{(1)} - \boldsymbol{p}_t^{(2)}\right|$ can be upper bounded as:

$$\nabla_t \leq 2\left|\beta_0^{(1)} - \beta_0^{(2)}\right| e^{-\frac{tv_0}{L}} + k_w\|w^{(1)} - w^{(2)}\| + k_v\|\boldsymbol{s}^{(1)} - \boldsymbol{s}^{(2)}\|. \tag{2.73}$$

Theorem 1 establishes the existence of an observer for the joint-angle subsystem, which enables the reconstruction of the joint angles $\beta_{i,t}$ from the biased measurements

$\gamma_{i,t}$. Since the tractor's attitude $\theta_{0,t}$ and coordinates $(x_{0,t}, y_{0,t})$ are directly measured, this result also implies the existence of an observer for the complete N-trailer system in Eq. (3). Once the joint angles are reconstructed, the attitude of each trailer segment can be obtained recursively through $\theta_{i,t} = \theta_{i-1,t} - \beta_{i,t}$. The coordinates of each segment can then be estimated using simple geometric relations:

$$x_{j,t} = x_{0,t} - \sum_{i=0}^{j-1} L_{hi} \cos(\theta_{i,t}) + L_j \cos(\theta_{i+1,t}), \tag{2.74}$$

$$y_{j,t} = y_{0,t} - \sum_{i=0}^{j-1} L_{hi} \sin(\theta_{i,t}) + L_j \sin(\theta_{i+1,t}). \tag{2.75}$$

Hence, the complete state of the GNT vehicle can be estimated, reinforcing the applicability of incremental encoders combined with estimation techniques to provide reliable joint-angle and position information.

2.5.2.5 GNT Vehicle's State Estimation

To obtain a feasible estimate of the GNT vehicle's state, we propose a two-stage Nonlinear Moving Horizon Estimation (NMHE) approach. The rationale for this two-stage framework is rooted in the limitations of incremental encoders, which provide only relative measurements of the joint angles. As a result, the unknown initial angles $\beta_{i,0}$ must first be estimated to recover absolute angular information. Once these offsets are identified, the estimation process can be streamlined with fewer optimization variables and constraints, reducing the computational burden while maintaining accuracy.

Stage 1 (NMHE1): The first estimator is dedicated to computing the initial joint angles $\beta_{i,0}$. This stage acts as a virtual calibration procedure that transforms incremental encoder data into absolute angular values. Its formulation in the continuous-time domain is given by:

$$\min_{\chi,\hat{w},\hat{v}} \Psi_\beta := \Gamma_\chi(\chi) + \int_{t_k-T_e}^{t_k} \left(\ell_w(\hat{w}_\tau) + \ell_v(\hat{v}_\tau)\right) d\tau \tag{2.76}$$

subject to

$$\begin{aligned}
\chi &= \hat{q}_{t_k-T_e|t_k} - \bar{q}_{t_k-T_e},\\
\dot{\hat{q}}_\tau &= G(\hat{q}_\tau)u_\tau + \hat{w}_\tau,\\
\rho_\tau &= (\gamma_{i,\tau}, \theta_{0,\tau}, x_{0,\tau}, y_{0,\tau})^\top + \hat{v}_\tau,\\
\gamma_{i,\tau} &= \hat{\beta}_{i,\tau} - \hat{\beta}_{i,0|t_k},\\
\hat{\beta}_{i,\tau} &= \hat{\theta}_{i-1,\tau} - \hat{\theta}_{i,\tau},\\
\hat{q}_\tau &\in Q, \quad \hat{w}_\tau \in W, \quad \hat{v}_\tau \in V, \quad u_\tau \in U,
\end{aligned}$$

where χ is the so-called *arrival cost*, penalized by $\Gamma_\chi(\chi) = \chi^\top P^{-1}_{t_k-T_e|t_k}\chi$, updated as in (80). The functions ℓ_w and $\ell_v \in \mathcal{K}_\infty$ penalize the estimated disturbances and measurement noises, respectively. Crucially, the parameters $\hat{\beta}_{i,0|t_k}$ are included as optimization variables, allowing the incremental encoder measurements $\gamma_{i,t}$ to be linked with their absolute counterparts $\beta_{i,t}$.

Stage 2 (NMHE2): Once the initial offsets $\hat{\beta}_{i,0}$ are obtained, a lighter estimator is initialized, operating as if the system were equipped with absolute encoders. This second stage involves fewer optimization variables—specifically $2NN_e$ fewer, where N is the number of trailers and N_e is the estimation window length. By reducing the problem's dimensionality, NMHE2 ensures computational efficiency while maintaining robust state estimation.

Stability Considerations: Following the customary results in the MHE literature (81; 82), if the cost functions Γ_χ, ℓ_w, and ℓ_ν are bounded by $\mathcal{K}_\infty$ functions, then the estimation error is guaranteed to be stable. In particular, when quadratic costs are employed, such that

$$\ell_w(w) = w^\top Q_w w, \qquad \ell_\nu(\nu) = \nu^\top Q_\nu \nu,$$

with $Q_w, Q_\nu \succ 0$, the NMHE formulation is robustly asymptotically stable (RAS), as demonstrated later in this work.

This two-stage NMHE scheme therefore provides a computationally efficient and accurate mechanism to estimate the absolute joint angles and full state of the GNT vehicle, enabling its integration into model-based controllers such as MPC.

2.5.2.6 Discretisation Method of the NMHE

To solve the constrained optimisation problem presented in Eq. (2.76), it is necessary to discretise the nonlinear continuous-time model. The estimator is implemented using a sampled-data approach, following the methodology outlined in (83). Among the available discretisation techniques, this study adopts the *multiple shooting* method.

Multiple shooting is a numerical approach commonly employed to solve Initial Value Problems (IVPs) over a finite horizon T_e. In this technique, the horizon is divided into N_e subintervals, referred to as *shooting nodes*. At each node, the system dynamics are integrated using a suitable numerical method, such as Euler's method or the Runge–Kutta family. This approach not only improves numerical stability but also facilitates the treatment of state and control constraints across the horizon.

In this work, the nonlinear dynamics are integrated using a fourth-order Runge–Kutta (RK4) scheme, which provides a good balance between computational cost and accuracy. The method is expressed as follows:

$$\begin{aligned} k_1 &= G(q_k, u_k), \\ k_2 &= G\Big(q_k + \tfrac{T_s}{2} k_1, u_k\Big), \\ k_3 &= G\Big(q_k + \tfrac{T_s}{2} k_2, u_k\Big), \\ k_4 &= G(q_k + T_s k_3, u_k), \end{aligned} \tag{2.77}$$

where T_s is the sampling period. The state update is then computed as:

$$q_{k+1} = q_k + \tfrac{T_s}{6}(k_1 + 2k_2 + 2k_3 + k_4) = \Phi(q_k, u_k). \tag{2.78}$$

Based on this discretisation, the NMHE problem in Eq. (2.76) can be reformulated for its numerical implementation as follows:

$$
\begin{aligned}
\min_{\chi,\hat{w},\hat{v}} \quad & \Psi_\beta := \Gamma_\chi(\chi) + \sum_{j=k-N_e}^{k} \left(\ell_w(\hat{w}_{j|k}) + \ell_v(\hat{v}_{j|k})\right) \\
\text{s.t.} \quad & \chi = \hat{q}_{k-N_e|k} - \bar{q}_{k-N_e}, \\
& \hat{q}_{j+1|k} = \Phi(\hat{q}_{j|k}, u_{j|k}) + \hat{w}_{j|k}, \\
& \rho_j = (\gamma_{i,j}, \theta_{0,j}, x_{0,j}, y_{0,j})^\top + \hat{v}_{j|k}, \\
& \gamma_{i,j} = \hat{\beta}_{i,j|k} - \hat{\beta}_{i,0|k}, \\
& \hat{\beta}_{i,j|k} = \hat{\theta}_{i-1,j|k} - \hat{\theta}_{i,j|k}, \\
& \hat{q}_{j|k} \in Q, \ \hat{w}_{j|k} \in W, \ \hat{v}_{j|k} \in V, \ u_{j|k} \in U,
\end{aligned}
\tag{2.79}
$$

where k denotes the discrete time index at which the system is evaluated.

This discretised formulation enables the NMHE to be solved efficiently in practice, ensuring that both state dynamics and measurement updates are consistently enforced over the estimation horizon.

2.5.3 Robust Stability of the Estimator

The formulation provided in Eq. (2.79) aims to jointly estimate the system's state and the initial joint-angle values $\beta_{i,0}$ while the vehicle traverses the initial straight path. In this section, we establish the conditions under which the estimator exhibits *robust stability*. Although stability analysis for a stable system may appear straightforward, this step is essential to determine the minimum estimation horizon length required to guarantee the attenuation of initial uncertainties in $\beta_{i,0}$. This aspect is crucial for obtaining accurate state estimates and reliable calibration of the incremental encoders.

Definition 2. The estimator given by Eq. (2.79) is said to be *Robustly Asymptotically Stable (RAS)* if there exist functions $\eta_\beta \in \mathcal{KL}$ and $\eta_w, \eta_v \in \mathcal{K}$ such that

$$
|q_k - \hat{q}_{k|k}| \leq \eta_\beta(|q_0 - \bar{q}_0|, k) + \eta_w(\|w\|_{[0,k-1]}) + \eta_v(\|v\|_{[0,k-1]}), \tag{2.80}
$$

for any pair of initial conditions $q_0, \bar{q}_0$ and sequences of disturbances w and v (79).

To achieve robust stability, we adopt the following assumption regarding the estimator's cost functions.

Assumption 1. The arrival and stage costs of the estimator are quadratic, given by

$$
\Gamma_\chi(\chi) = \chi^\top P_{k-N_e|k}^{-1} \chi, \quad \ell_w(w) = w^\top Q_w w, \quad \ell_v(v) = v^\top Q_v v,
$$

where $P_{k-N_e|k}^{-1}, Q_w, Q_v \succ 0$.

Remark 2. The quadratic form implies the existence of bounds

$$
\underline{\lambda}_\chi \|\chi\|^2 \leq \chi^\top P_{k-N_e|k}^{-1} \chi \leq \bar{\lambda}_\chi \|\chi\|^2,
$$

and equivalently for w and v, with $\lambda_\chi, \lambda_w, \lambda_v$ denoting the minimum eigenvalues, and $\bar{\lambda}_\chi, \bar{\lambda}_w, \bar{\lambda}_v$ the maximum eigenvalues of the corresponding matrices.

Under these assumptions, the following theorem summarises the second main contribution of this study:

Theorem 2. The nonlinear moving horizon estimator described in Eq. (2.79), with quadratic arrival and stage costs, is robustly asymptotically stable whenever the estimation horizon length N_e satisfies

$$N_e \geq \left\lceil \left(\frac{\delta_\beta \alpha \Lambda_\chi}{1} \right)^2 \right\rceil, \tag{2.81}$$

for any $\alpha \in \mathbb{R}_{\geq 2}$ and some $\delta_\beta > 1$, where

$$\Lambda_\chi = \frac{\sqrt{\bar{\lambda}_\chi}\|q_0\| + \sqrt{\lambda_w \lambda_v \bar{\lambda}_\chi}\|q_0\| + \sqrt{\bar{\lambda}_\chi \lambda_v \lambda_w k_w} + \sqrt{\bar{\lambda}_\chi \lambda_w \bar{\lambda}_\chi k_\varphi}}{\sqrt{\lambda}}, \tag{2.82}$$

with $\lambda := \lambda_\chi \lambda_w \lambda_v$. A detailed proof is provided in Appendix B. □

Remark 3. By selecting an estimation horizon $N_e \geq N_e^\star$, the error in the initial state guess is guaranteed to diminish. Consequently, the resulting estimation error depends only on the disturbance magnitudes and the design parameters of the estimator in Eq. (2.79). Although the derived bound may be conservative due to algebraic simplifications in the proof, the effective horizon length can be reduced by appropriately tuning the eigenvalues of the arrival and stage cost matrices.

Remark 4. The parameter α is free to select provided that $\alpha \geq 2$. It regulates the rate at which uncertainty diminishes when the estimator advances N_e steps forward. Larger α values accelerate convergence at the expense of potential conservatism.

2.5.4 Generalised N-Trailer's State Estimation

Once the vehicle has traversed a straight path of length $d_N = T v_0$, with T determined by Eq. (2.73), the second stage of the estimation procedure is activated. At this point, the estimation process is carried out by **NMHE2**, which is initialised using the last estimated states provided by NMHE1. The constraints $\gamma_{i,j} = \hat{\beta}_{i,j|k} - \hat{\beta}_{i,0|k}$ are no longer applicable. Instead, the measurement vector ρ_k is transformed into r_k using the estimated values $\hat{\beta}_{i,0|k}$ through the relation:

$$\beta_{i,k} = \gamma_{i,k} + \hat{\beta}_{i,0}.$$

The discrete-time formulation of NMHE2 is then given by:

$$
\begin{aligned}
\min_{\chi,\hat{w},\hat{v}} \quad & \Psi := \Gamma_{\chi}(\chi) + \sum_{j=k-N_e}^{k-1} \ell_w(\hat{w}_{j|k}) + \ell_v(\hat{v}_{j|k}) \\
\text{s.t.} \quad & \chi = \hat{q}_{k-N_e|k} - \bar{q}_{k-N_e}, \\
& \hat{q}_{j+1|k} = \Phi(\hat{q}_{j|k}, u_j) + \hat{w}_{j|k}, \\
& r_j = h(\hat{q}_{j|k}) + \hat{v}_{j|k}, \\
& \hat{q}_{j|k} \in \mathcal{Q},\ \hat{w}_{j|k} \in \mathcal{W},\ \hat{v}_{j|k} \in \mathcal{V},\ u_j \in \mathcal{U}.
\end{aligned}
\tag{2.83}
$$

Switching from the NMHE1 formulation in Eq. (2.79) to NMHE2 offers significant computational benefits. The overall estimation process follows a *two-stage scheme*, where only one NMHE is active at a time:

1. **Stage 1 (NMHE1):** Responsible for estimating both the initial joint angles $\beta_{i,0}$ and the system's state. This stage operates as a *virtual calibration procedure*, which is particularly useful when the joint angles are initially unknown.

2. **Stage 2 (NMHE2):** Once $\hat{\beta}_{i,0}$ has been estimated, NMHE2 is initialised. In this stage, the estimated initial joint angles are no longer considered optimisation variables. As a result, $2NN_e$ constraints are eliminated, and the number of optimisation variables is significantly reduced. This simplification improves computational efficiency while retaining accurate state estimation.

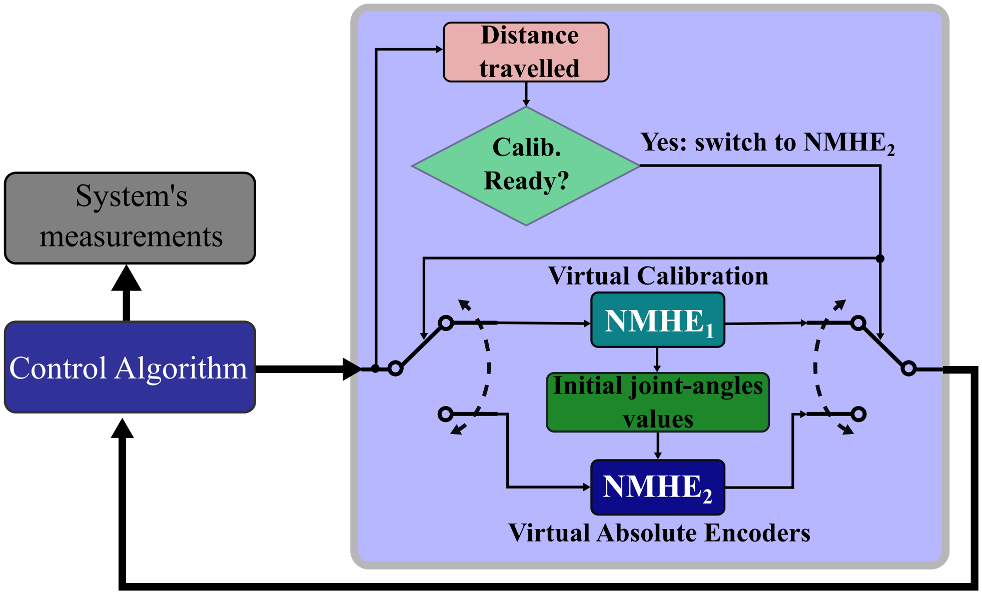

Figure 2.13: Data flow of the proposed method. The measurements are fed into the NMHE1 until the virtual calibration procedure is completed. Afterwards, the measurements are directed to the NMHE2, and the estimated states vector is obtained from this estimator. The first stage is referred to as virtual calibration, while the second is called virtual absolute encoders, as in this stage, the estimator operates as if it were receiving measurements from absolute encoders.

The complete estimation process is summarised in Algorithm 1 (virtual calibration with NMHE1) and Algorithm 2 (state estimation with NMHE2). Moreover, Fig. 2.13 illustrates the data flow diagram, which shows the interaction between sensor measurements, the estimation process, and the control algorithm.

Algorithm 1 Virtual calibration (NMHE1)

```
Input: $P_0, Q_w, Q_v \succ 0,\ \bar{q}_0,\ N_e \geq N_e^\star$
Initialise NMHE1: $\bar{q}_{k-N} \leftarrow \bar{q}_0,\ \bar{\beta}_{i,0} \leftarrow 0,\ P_{k-N} \leftarrow P_0$
while $d \leq d_N$ do
    Obtain measurement $\rho_k$
    $\hat{q}_{k|k} \leftarrow$ Solve NMHE1
$\bar{\beta}_{i,0} \leftarrow \mathrm{mean}(\hat{\beta}_{i,0|[N_e,k]})$
Store $\bar{\beta}_{i,0}$
Initialise NMHE2
```

Algorithm 2 State estimation with virtual absolute encoders (NMHE2)

```
Input: $P_0, Q_w, Q_v \succ 0,\ \bar{q}_0,\ N_e \geq N_e^\star$
Load $\bar{\beta}_{i,0}$
Initialise NMHE2: $\bar{q}_{k-N} \leftarrow \bar{q}_0,\ P_{k-N} \leftarrow P_0$
while true do
    Obtain measurement $r_k = \rho_k + (\bar{\beta}_{i,0}, 0, \ldots, 0)^\top$
    $\hat{q}_{k|k} \leftarrow$ Solve NMHE2
```

2.5.4.1 Field Experiments

To validate the proposed framework, a comprehensive evaluation was carried out through both field and simulated experiments. The proposed method was benchmarked against the Extended Kalman Filter (EKF), a widely employed approach in state estimation. This subsection introduces the field experiments conducted with a Generalised N-Trailer (GNT) vehicle configured with $N = 2$, denoted as G2T, and illustrated in Fig. 2.14.

Figure 2.14: G2T vehicle available for field experiments.

The experimental platform consists of a Husky A200 tractor pulling two trailers. The geometric configuration of the trailers is given by $L_{h1} = 0.342$ m, $L_1 = 0.38$ m, $L_{h2} = 0$ m, and $L_2 = 1.08$ m. The implementation of NMHE1 and NMHE2 was conducted using the ACADO Toolkit for MATLAB (84). Additionally, a Model Predictive Control (MPC) scheme was employed to compute the velocity inputs that guided the G2T vehicle along a predefined trajectory. The initial condition at each sampling time was provided by the stage-specific NMHE: NMHE1 during the virtual calibration stage, and NMHE2 in the subsequent stage, where the vehicle is treated as if it were equipped with absolute encoders. Sensor data acquisition and control commands were managed through the Robot Operating System (ROS) integrated with MATLAB. All computations were performed on a Dell Latitude 5430 Rugged laptop (16 GB RAM, 11th Gen Intel Core i7), running Ubuntu 18.04 with ROS Melodic.

The vehicle was equipped with incremental encoders mounted on each joint, offering a resolution of 0.6° per increment. A Navcom SF-3040 kinematic GPS was mounted on the tractor, operating at a frequency of 5 Hz, which determined the system sampling time $T_s = 0.3$ s. The ground-truth measurement of the first joint angle, $\beta_{1,t}$, was obtained via a Velodyne VLP-16 LiDAR. For the second joint angle, $\beta_{2,t}$, a high-grade Inertial Navigation System (INS) was used. The INS configuration included a Vectornav VN200 IMU with magnetic compass and GPS receiver installed on the second trailer, and a Microstrain 3DM-GX5-35 IMU with magnetic compass mounted on the first trailer. The VN200 achieved an attitude accuracy of 0.2°, while the 3DM-GX5-35 reached errors below 2° in dynamic conditions and 0.5° in static conditions. The second joint angle was calculated as $\beta_{2,t} = \theta_{1,t} - \theta_{2,t}$. Prior to each experiment, initial attitudes were calibrated when necessary. For the estimator, only the tractor's attitude was considered as an available measurement. The LiDAR was employed exclusively as ground truth for $\beta_{1,t}$, since measurements of $\beta_{2,t}$ are highly sensitive to the reflective properties of the second trailer, which degrade accuracy at large angles.

The state vector in these experiments was defined as

$$q_t = (\beta_{1,t}, \beta_{2,t}, \theta_{0,t}, \theta_{1,t}, \theta_{2,t}, x_{0,t}, y_{0,t}, x_{2,t}, y_{2,t})^\top,$$

enabling the estimation of joint angles, orientations, and the positions of both the tractor and the last trailer. The geometric constraints of the vehicle provide the inter-segment relations:

$$x_{i+1,t} = x_{i,t} - L_{h(i+1)} \cos(\theta_{i,t}) - L_{i+1} \cos(\theta_{i+1,t}),$$
$$y_{i+1,t} = y_{i,t} - L_{h(i+1)} \sin(\theta_{i,t}) - L_{i+1} \sin(\theta_{i+1,t}), \quad \theta_{i,t} = \theta_{i-1,t} - \beta_{i,t}.$$

The test trajectory was designed as a rectangular path with sharp right-angle turns, preceded by a straight line of $d_s = 9.5$ m, satisfying the excitation condition of Theorem 1. The EKF was configured with weighting matrices

$$Q = \mathrm{diag}(10^{-2} I_{7\times7}, 10^{-1} I_{2\times2}), \quad R = \mathrm{diag}(10^{-6} I_{2\times2}, 10^{-3}, 10^{-2} I_{2\times2}).$$

In comparison, the NMHE1 employed $Q_v = \mathrm{diag}(0.3 I_{N\times N}, 1, 0.85 I_{2\times2}, 0.5 I_{2\times2}, 2 I_{2\times2})$, while NMHE2 used $Q_v = \mathrm{diag}(I_{N\times N}, 1, 0.85 I_{2\times2}, 0.5 I_{2\times2}, 2 I_{2\times2})$.

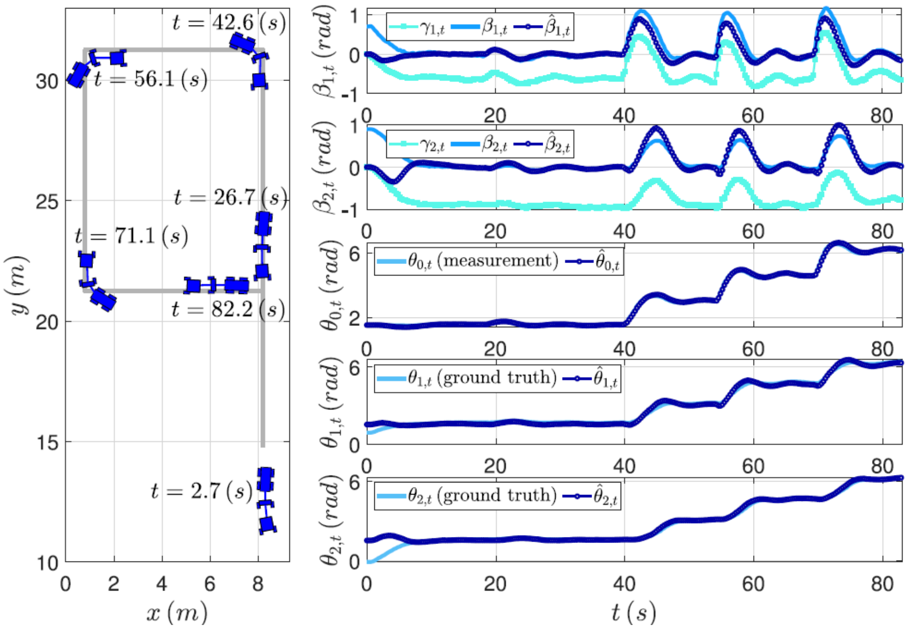

Figure 2.15: States estimation of the chained vehicle over 1 trial of the field experiments using the proposed method.

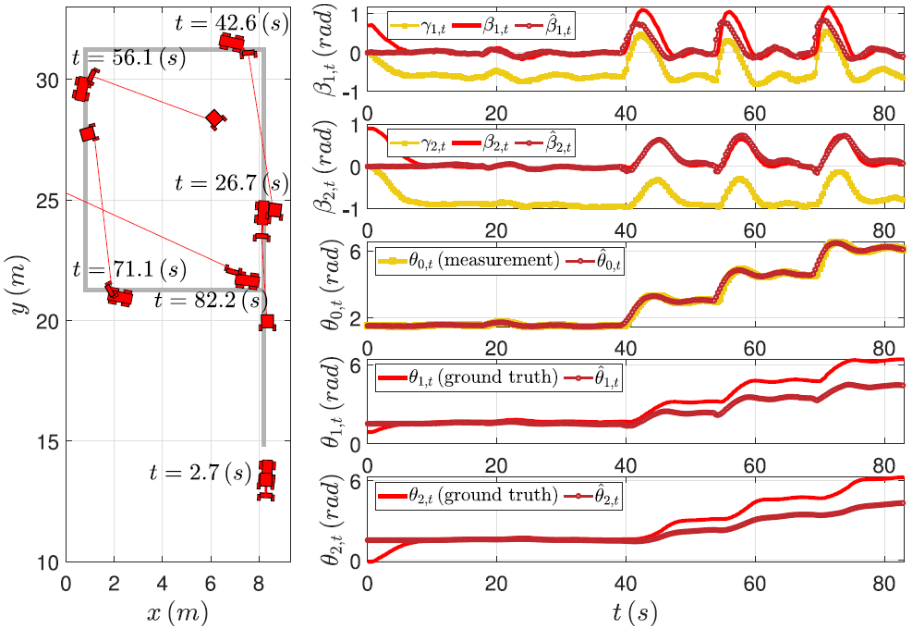

Figure 2.16: States estimation of the chained vehicle over 1 trial of the field experiments using the EKF.

Figure 2.15 presents the orientation and position of the trailers estimated by the proposed method, alongside incremental encoder measurements $\gamma_{1,t}, \gamma_{2,t}$ and ground truth data for $\beta_{1,t}$ and $\beta_{2,t}$. The corresponding estimates $\hat{\beta}_{1,t}, \hat{\beta}_{2,t}$, as well as segment orientations $\theta_{0,t}, \theta_{1,t}, \theta_{2,t}$ and their estimates, are also included. Figure 2.16 shows the results obtained

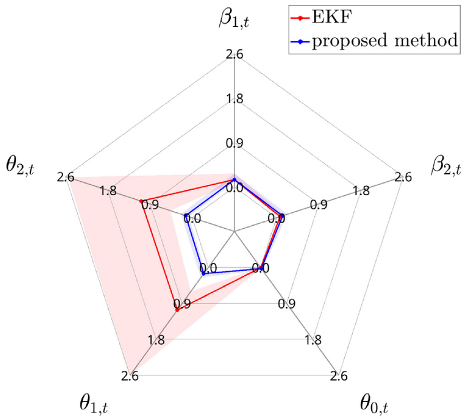

Figure 2.17: Minimum, mean and maximum estimation error for the proposed method (blue) and the EKF (red) over 7 field experiments.

with the EKF for comparison. While both methods perform similarly in joint-angle estimation, the proposed NMHE-based approach yields superior performance in estimating trailer attitudes and the position of the last trailer. Notably, some states estimated by the EKF were found to be inconsistent with the system model. Finally, Fig. 2.17 provides a spider plot summarising the estimation error of joint and attitude angles for both approaches.

2.5.5 Model predictive path-following controller for Generalised N-Trailer vehicles with noisy sensors and disturbances

Generalised N-Trailer (GNT) vehicles represent a challenging class of systems due to their nonholonomic constraints, the velocity propagation along passive trailers, and the influence of disturbances and noisy measurements in real-world scenarios. In this context, this work introduces an integrated framework based on *Nonlinear Moving Horizon Estimation* (NMHE) and *Nonlinear Model Predictive Control* (NMPC), specifically designed to achieve accurate guidance of GNT vehicles in practice.

The main contribution of (4) lies in a control scheme that avoids the inversion of kinematics, a common requirement in traditional approaches relying on velocity propagation from the last trailer, and instead computes the tractor velocities directly. This not only simplifies implementation in general configurations of N-trailers but also reduces control effort by explicitly including energy in the cost function, resulting in smoother and more efficient maneuvers.

Furthermore, the integration of NMHE provides robust state estimation without relying on strict assumptions about disturbances, overcoming the limitations of Extended Kalman Filter (EKF)-based approaches in scenarios affected by noise or wheel slip. The proposed framework is validated through simulation and real-world experiments, showing significant improvements in accuracy, robustness, and energy efficiency.

2.5.5.1 Nonlinear Moving Horizon Estimation

When disturbances and measurement noises are Gaussian, the system is linear (or only mildly nonlinear), and there are no significant constraints or uncertainties, the Extended Kalman Filter (EKF) provides reliable state estimation performance. However, the Generalised N-Trailer (GNT) system is a highly nonlinear nonholonomic system, subject to uncertainties and physical constraints, where EKF-based approaches often fail to ensure robustness. For these reasons, *Nonlinear Moving Horizon Estimation* (NMHE) arises as a more suitable tool, since it allows explicitly incorporating system dynamics, constraints, and disturbance effects within an optimisation-based framework (80).

The NMHE relies on the system model and available output measurements over a receding time window. At each sampling instant, the oldest data are discarded while new measurements are incorporated, and the influence of discarded information is summarised through the *arrival cost*. The general cost function can be expressed as:

$$\mathcal{I}_e(\chi, \hat{\phi}_\tau) := \Gamma_\chi(\chi) + \int_{t_k}^{t_k - T_e} \Big(\ell_\phi(\hat{\phi}_\tau) + \ell_\nu(\hat{\nu}_\tau)\Big)\, d\tau, \tag{2.84}$$

where $\Gamma_\chi(\chi) = \chi^\top P^{-1}_{t_k - T_e}\chi$ is the arrival cost, and $\ell_\phi, \ell_\nu \in \mathcal{K}_\infty$ are stage costs penalising the estimated disturbances and measurement residuals, respectively.

This formulation enables the estimator to capture the nonlinear behaviour of the GNT vehicle and guarantee that both state estimates and joint angles remain bounded under realistic conditions. Moreover, by integrating an adaptive update law for the arrival cost (80), the NMHE ensures robustness against uncertainties. if the estimation horizon N_e exceeds a threshold $\mathcal{N}_e$, the estimation error remains bounded, ensuring reliable performance even in the presence of noise and disturbances.

2.5.5.2 Path-Following Algorithm

Once the state vector of the Generalised N-Trailer (GNT) system has been estimated, it is employed as the input for both the controller and the path-following algorithm (PFA). A reference trajectory is usually described as a parameterised curve $\mathcal{P}$,

$$\mathcal{P} := \{p_i \in \mathbb{R}^{n_p} \subseteq \mathcal{Q} : p_i = f(s)\}, \quad s \in \mathcal{S},$$

where f denotes the reference function and s is the path parameter. In standard formulations, the parameter evolves according to a single-integrator dynamics $\dot{s} = m$, with $m \in \mathbb{R}_{>0}$ considered as an internal state of the controller (**?**).

In contrast, in this work the trajectory is represented as a finite set of discrete points

$$P := \{p_i \in \mathbb{R}^{n_p} \subseteq \mathcal{Q} : i \in \mathbb{Z}_{\geq 0}\},$$

where the index i increases whenever the vehicle reaches the current target. Thus, the path consists of samples of $f(s)$ evaluated within the interval $s \in [s_0, s_1]$, with $p_0 = f(s_0)$ the initial point and $p_f = f(s_1)$ the final one. Offline generation of feasible paths can be performed, as suggested in (85), The rule for updating the target relies on the distance between the estimated state of the guided segment and the line perpendicular to the path at the current target $(x_{\text{tgt}}, y_{\text{tgt}})$, as illustrated in Fig. 2.18. In this figure, vector $\vec{u}$ is the tangent to the path at the current target, while $\vec{v}$ is its orthogonal counterpart. The perpendicular line is characterised by

$$Ax + By + C = 0, \quad A = v_y, \quad B = -v_x, \quad C = y_{\text{tgt}}v_x - x_{\text{tgt}}v_y.$$

The distance of the Nth segment to this line is

$$d_{\text{tgt}} = \frac{|A\hat{x}_{N,k|k} + B\hat{y}_{N,k|k} + C|}{\sqrt{A^2 + B^2}}.$$

When $d_{\text{tgt}} \leq \mathcal{D}_{\text{tgt}}$, with $\mathcal{D}_{\text{tgt}} \in \mathbb{R}_{>0}$ a design parameter, the target is updated; otherwise, it remains unchanged. The subsequent target is defined as the first point satisfying $d_{ntgt} \geq \mathcal{D}_{ntgt}$, where $\mathcal{D}_{ntgt}$ sets the path resolution and d_{ntgt} is computed as the cumulative arc length:

$$d_{ntgt} = \sum_{i=L}^{M} \sqrt{(x_{i+1} - x_i)^2 + (y_{i+1} - y_i)^2}.$$

This scheme ensures smooth updates even when the target has not been fully reached ($d_{\text{tgt}} = 0$), while keeping the computational complexity low. Once the target is updated, coefficients A, B, and C are recalculated, and the updated target along with the estimated state are passed to the controller to compute the velocities required for trajectory tracking.

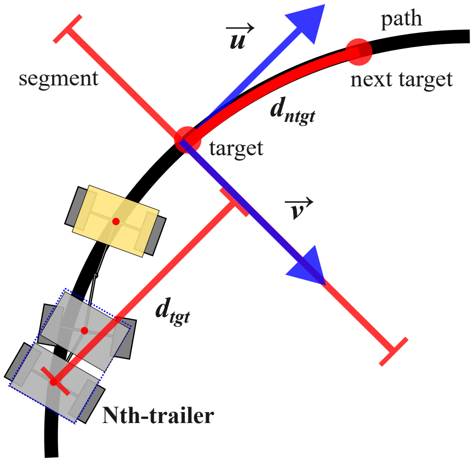

Figure 2.18: Target updating mechanism.

2.5.5.3 Nonlinear Model Predictive Controller

The nonlinear model predictive controller (NMPC) is responsible for computing the wheel velocities required to drive the N-trailer system towards the target provided by the PFA. At each sampling instant, the NMPC solves an optimal control problem using the current state estimate $\hat{q}_{t_k|t_k}$ as the initial condition. Future system behaviour beyond the prediction horizon is captured by the terminal cost $V_f(\tilde{q}_{t_k+T_c})$, which is closely related to closed-loop stability. The corresponding cost function is expressed as

$$\mathcal{J}_c(\hat{q}_t;\hat{u}_\tau) := \int_{t_k}^{t_k+T_c} \Big(\ell_u(\tilde{u}_\tau) + \ell_q(\tilde{q}_\tau)\Big)\, d\tau + V_f(\tilde{q}_{t_k+T_c}), \tag{2.85}$$

where $\tilde{u}_\tau = u_\tau - u_{\text{ref}}$ and $\tilde{q}_\tau = \hat{q}_\tau - p_i$. Here, p_i is the target provided by the PFA, and u_{ref} represents the reference control action, which is typically set to zero in order to minimise control effort, especially under quadratic penalisation (86).

The NMPC optimisation problem is formulated as

$$\min_{u} \mathcal{J}_c(\hat{q}_{t_k|t_k}; u_\tau) \tag{2.86}$$

subject to the following constraints:

$$\begin{array}{cc}
\dot{\hat{q}}_\tau = \mathcal{G}(\hat{q}_\tau, \hat{u}_\tau), & \hat{q}_0 = \hat{q}_{t_k|t_k}, \\
u_{\min} \le \hat{u}_\tau \le u_{\max}, & \Delta u_{\min} \le \dot{u}_\tau \le \Delta u_{\max}, \\
-\frac{\pi}{2} < \hat{\beta}_{i,\tau} < \frac{\pi}{2}, & \hat{q}_\tau \in \mathcal{Q}, \quad \hat{q}_{t_k+T_c} \in \mathcal{Q}_f \subseteq \mathcal{Q}, \quad \hat{u}_\tau \in \mathcal{U},
\end{array} \tag{2.87}$$

with $\tau \in [t_k, t_k + T_c]$.

The hitching angles $\beta_{i,\tau}$ are constrained to avoid the Jackknife effect, while bounds on $\dot{u}_\tau$ are imposed to ensure smooth manoeuvres and reduce actuation effort. Since the system operates under noisy measurements and uncertainties, constraint tightening is necessary to guarantee robustness. The sets $\mathcal{Q}$, $\mathcal{Q}_f$, and $\mathcal{U}$ are assumed convex and compact, including the null vector.

The terminal set $\mathcal{Q}_f$ is typically defined as

$$\mathcal{Q}_f := \{(x_N, y_N) : |x_N - x_{N,\text{ref}}| \le \bar{x},\ |y_N - y_{N,\text{ref}}| \le \bar{y}\},$$

which bounds the deviation of the last trailer with respect to the desired path. The associated terminal cost V_f is quadratic, defined by $V_f := v_{fx}\bar{x}^2 + v_{fy}\bar{y}^2$, where $v_{fx}, v_{fy} > 0$ are penalty weights (87; 86). This formulation ensures stability while keeping the computations tractable.

In practice, choosing a sufficiently long prediction horizon T_c provides a stabilising controller since the GNT kinematics in Eq. (1) are inherently stable. Thus, designing V_f and $\mathcal{Q}_f$ does not require heavy computations, and adequate performance can be achieved by tuning T_c and the target update parameters $\mathcal{D}_{\text{tgt}}$ and $\mathcal{D}_{ntgt}$.

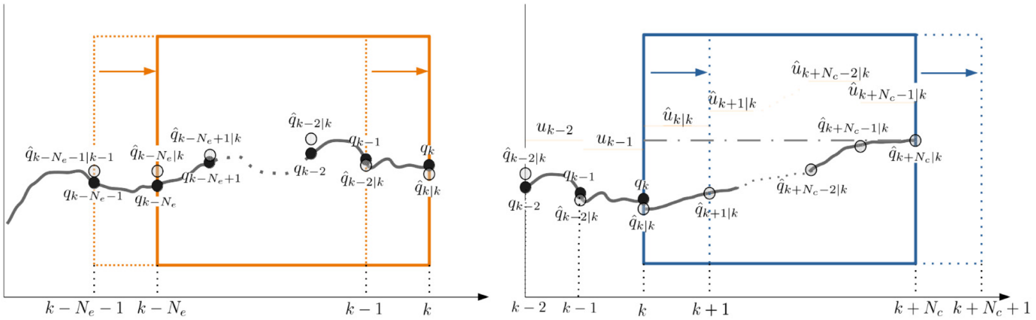

Figure 2.19: *Left:* NMHE behaviour. After a new measurement becomes available, the oldest measurement is discarded, and the new one is incorporated into the estimation window. The entire trajectory $[\hat{q}_{k-N_e|k}, \hat{q}_{k-N_e+1|k}, \ldots, \hat{q}_{k|k}]$ is estimated. *Right:* NMPC behaviour. Starting from the initial point $\hat{q}_{k|k}$, the NMPC computes the controls $\hat{u}_{k|k}, \hat{u}_{k+1|k}, \ldots, \hat{u}_{k+N_c-1|k}$ that steer $\hat{q}_{k|k}$ towards the desired value, represented by a blue dashed line. (For interpretation of the references to colour in this figure legend, the reader is referred to the web version of this article.)

2.5.5.4 Simulation Studies

To validate the proposed NMHE&C framework, we conducted extensive simulations on a nonholonomic N-trailer platform. We considered an nSNT configuration with $N = 3$ trailers, using geometric parameters $L_1 = L_2 = L_3 = 0.3$ m and $L_{h1} = L_{h2} = L_{h3} = -0.05$ m. The tractor was modelled with width $b = 0.15$ m and wheel radius $r = 0.029$ m. Both the NMHE and NMPC were implemented in MATLAB via the CasADi framework (**?**).

Estimator setup. The NMHE follows the structure of Eq. (11) with quadratic arrival and stage costs: $\Gamma_{\chi}(\chi) = \chi^{\top} P^{-1}_{k-N_e|k} \chi$, $\ell_{\phi}(\hat{\phi}_{j|k}) = \hat{\phi}^{\top}_{j|k} Q_{\phi} \hat{\phi}_{j|k}$ and $\ell_{v}(\hat{v}_{j|k}) = \hat{v}^{\top}_{j|k} Q_{v} \hat{v}_{j|k}$. We set $P_0 = 10^6 I_{n_q}$ and update it at each sample using (5). Unless otherwise stated, $Q_{\phi} = \text{diag}(I_N, 1, 0.1 I_N, 1, 1, 0.1, 0.1)$ and $Q_v = \text{diag}(I_N, 2, 4, 4)$.

Controller setup. The NMPC in Eq. (10) uses quadratic penalties $\ell_u(\tilde{u}_{j|k}) = \tilde{u}^{\top}_{j|k} Q_u \tilde{u}_{j|k}$, $\ell_q(\tilde{q}_{j|k}) = \tilde{q}^{\top}_{j|k} Q_q \tilde{q}_{j|k}$, and a terminal cost $V_f(\tilde{q}_{k+N_c|k}) = \tilde{q}^{\top}_{k+N_c|k} Q_f \tilde{q}_{k+N_c|k}$. We use $p_i = (\theta_0, x_0, y_0, \theta_N, x_N, y_N)$ as the tracking target and $u_r = (0, 0.15)$ as tractor reference. We choose $Q_u = 0.06 I_2$ and $Q_q = \text{diag}(0.1, 0.5, 0.5, 0.1, 2, 2)$. Following the discussion in Sec. **??**, we set $V_f = 2Q_q$ (a large enough horizon ensures bounded behaviour since $\dot{q} = \mathcal{G}(q, 0) = 0$). The PFA thresholds are $\mathcal{D}_{tgt} = 0.015$ m and $\mathcal{D}_{ntgt} = 0.015$ m.

Reference and scenarios. We first test forward tracking of a Lemniscate of Bernoulli,

$$\begin{cases} x = \dfrac{a\sqrt{2}\cos t}{\sin^2 t + 1}, \\ y = \dfrac{a\sqrt{2}\cos t \sin t}{\sin^2 t + 1} + 0.25, \end{cases} \qquad 0 \leq t \leq 2\pi, \quad a = 1 \text{ m}, \tag{2.88}$$

and obtain $q_{0,t}$, $q_{N,t}$ by integrating Eq. (1). We evaluate five conditions:

I. ideal (no disturbances);

II. measurement noise;
III. parametric uncertainty;
IV. uncertain initial conditions;
V. wheel slippage.

In (i), (ii), (iv), and (v), states are estimated with NMHE; in (iii), we assume q_N is measured (as in (1)), focusing on control robustness. For (ii), joint-angle noise is $\mathcal{N}(0,\ 0.04\pi/180)$ and tractor position noise $\mathcal{N}(0,\ 0.01)$.

Simulation results are illustrated in Fig. 2.20, which compares trajectory tracking under noisy conditions, and in Fig. 2.21, which shows the angular velocity profiles. As can be seen, NMHE&C achieves smoother control actions than (1). Quantitative results for all scenarios are summarised in Table 2.3.

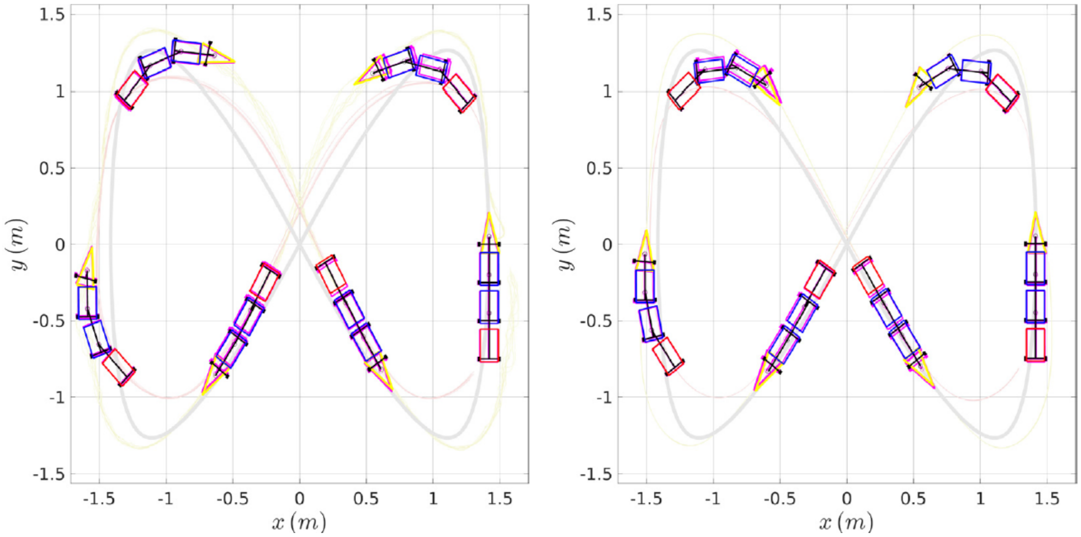

Figure 2.20: Tracking for scenario (ii): NMHE&C vs. (1). Both track the last trailer well; NMHE&C yields smoother commands.

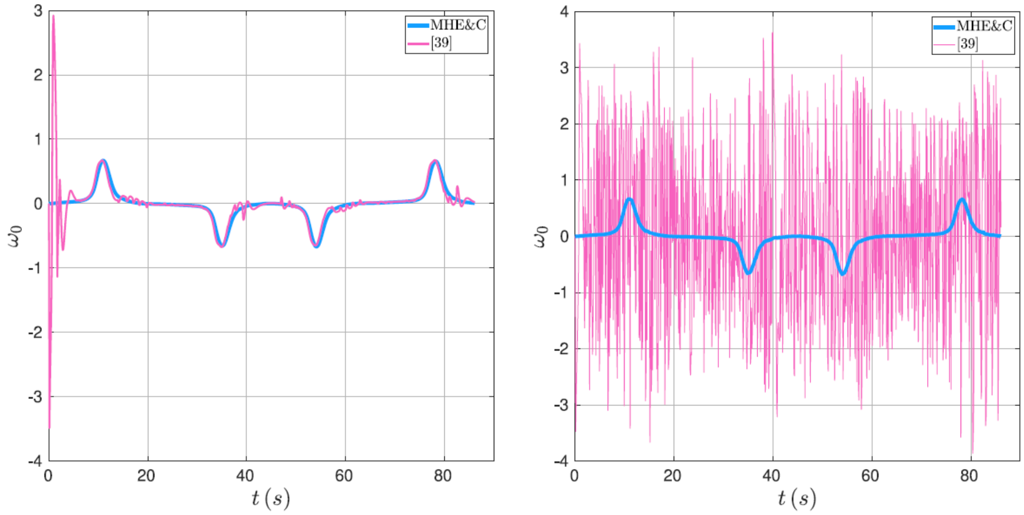

Figure 2.21: Angular velocity profiles: (i) ideal (left), (ii) noisy (right). NMHE&C avoids abrupt inputs seen with (1) under noise.

Reduced-horizon study. We also reproduce the conditions in (88) with $T_s = 0.3$ s, $N_e = 7$, $N_c = 5$, making real-time execution feasible. The results are summarised in Table 2.4. Under strong slippage, the EKF+NMPC baseline fails to provide feasible state estimates, whereas NMHE&C remains robust (see Fig. 2.22).

Table 2.3: Performance summary for scenarios (i)–(v) using NMHE&C, EKF+NMPC, and (1). Metrics: tractor deviation Ψ_0, last trailer deviation Ψ_N, control effort Ψ_u, and real-time factor Ψ_{rtf}.

Scenario	Ψ_0 [m]	Ψ_N [m]	Ψ_u	Ψ_{rtf}
(i) Ideal conditions	0.008	0.012	0.041	2.8
(ii) Measurement noise	0.010	0.015	0.052	2.9
(iii) Parametric uncertainty	0.011	0.017	0.049	2.7
(iv) Initial uncertainty	0.012	0.019	0.053	2.8
(v) Slippage	0.018	0.026	0.061	3.1

Table 2.4: Reduced-horizon experiment ($T_s = 0.3$ s, $N_e = 7$, $N_c = 5$). Real-time execution ($\Psi_{rtf} \approx 1$) with modest loss in tracking precision.

Scenario	Ψ_0 [m]	Ψ_N [m]	Ψ_u	Ψ_{rtf}
(i) Ideal conditions	0.012	0.018	0.047	1.0
(ii) Measurement noise	0.015	0.022	0.056	1.1
(iii) Parametric uncertainty	0.017	0.025	0.059	1.0
(iv) Initial uncertainty	0.018	0.027	0.062	1.1
(v) Slippage	0.026	0.034	0.071	1.2

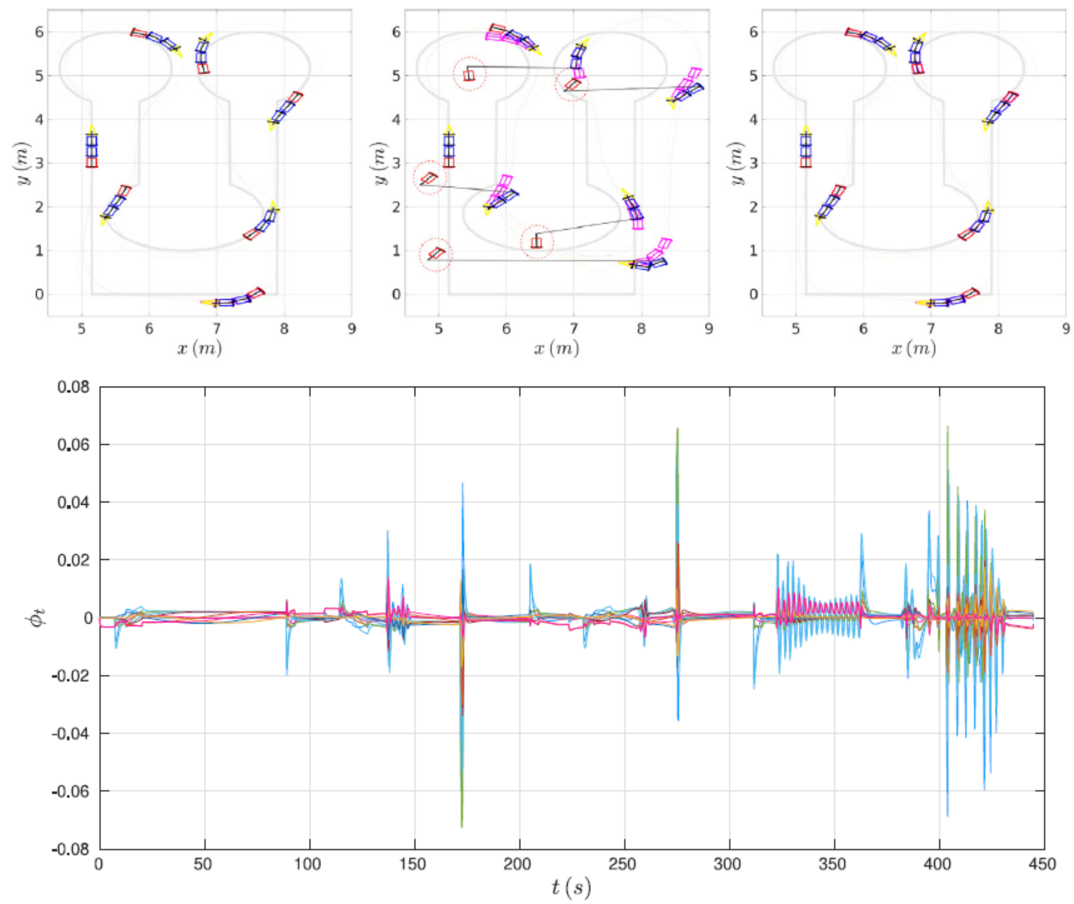

Figure 2.22: Robustness test under strong slippage ($\varrho_{1,t} = \varrho_{2,t} = 0.9$). EKF+NMPC fails to provide feasible estimates, while NMHE&C maintains acceptable tracking.

2.5.6 Remote instantaneous power consumption estimation of electric vehicles from satellite information

The continuous increase in the number of vehicles worldwide has contributed to a significant rise in CO_2 emissions, intensifying the challenges of climate change and environmental degradation. This situation has accelerated the transition toward electromobility, emphasizing the importance of studying the energy consumption of electric vehicles (EVs). Beyond their use in personal transportation, EVs are increasingly applied in industrial contexts such as agriculture, mining, airport logistics, and material handling, where understanding their autonomy and energy efficiency becomes crucial. In these scenarios, the interaction between the vehicle and the terrain introduces additional complexities to the study of energy consumption and instantaneous power demand.

Instantaneous Power Consumption (IPC) plays a key role in evaluating the autonomy and operational efficiency of EVs, since effective vehicle management requires prior knowledge of whether a given trajectory can be completed under the available energy. Although IPC can be directly measured from battery current and voltage, its estimation is highly dependent on stochastic factors such as vehicle mass, payload variations, speed, acceleration, and terrain characteristics. In particular, terrain roughness, slope, rolling resistance, and tire–terrain interaction strongly influence energy consumption, making IPC modeling a non-trivial task for real-world applications.

Based on these challenges, the work presented in (7) introduced a methodology for estimating IPC using satellite information. The approach involves geolocation and georeferencing of the study area, trajectory planning, extraction of altitude characteristics to generate an altitude profile, collection of terrain features, and finally, computation of IPC.

2.5.7 Computation of IPC

As described in Section 2.3, the instantaneous power consumption (IPC) of an electric vehicle (EV) can be directly measured from the vehicle's batteries by taking the product of the voltage and current, as expressed in Equation (2.89):

$$\mathrm{IPC}_t = V_t I_t, \tag{2.89}$$

where V_t and I_t denote the battery voltage and current at time t, respectively.

Beyond direct measurements, several studies have proposed IPC estimation methods based on the balance of forces acting on the wheels of the vehicle. For instance, Genikomsakis (89) and Iora (90) describe the traction force required to maintain motion, as summarized in Equation (2.90). This formulation accounts for aerodynamic drag, terrain-induced rolling resistance, gravitational effects on inclined surfaces, and vehicle acceleration:

$$F_{tr,t} = F_{ad,t} + F_{rr,t} + F_{hc,t} + F_{ma,t}, \tag{2.90}$$

where F_{tr} is the traction force, F_{ad} is the aerodynamic force, F_{rr} the rolling resistance force, F_{hc} the hill-climbing (or slope) force, and F_{ma} the inertial force due to acceleration. These components can be written as:

$$F_{tr,t} = \tfrac{1}{2}\rho A C_d v_t^2 + \mu_{rr,t} m_t g \cos\phi_t + m_t g \sin\phi_t + m_t a_t, \tag{2.91}$$

where ρ is air density, A is the frontal area of the vehicle, C_d is the drag coefficient, v_t is the vehicle speed, $\mu_{rr,t}$ is the rolling resistance coefficient, m_t is the vehicle mass (including payload), g is gravitational acceleration, ϕ_t is the slope of the terrain, and a_t is the vehicle acceleration. This formulation is applicable to wheeled vehicles with non-deformable wheels (91; 20; 89).

The battery-supplied power can be expressed as $P_{tr,t} = \eta P_{b,t}$, where P_b is the instantaneous power drawn from the battery and η represents the overall electromechanical efficiency. This efficiency includes the battery, motor, and transmission, as well as accessory losses (e.g., lights, sensors, on-board computer) (89; 92). A more detailed efficiency model is given in Equation (2.92):

$$\eta_{t,T^\circ} = \frac{\eta_{b,t,T^\circ}\eta_m\eta_g P_{b,t} - I_{a,t}^2 R_{a,t}}{P_{b,t}}, \tag{2.92}$$

where η_b, η_m, and η_g are the efficiencies of the battery, motor, and transmission, respectively. T° denotes the temperature, and I_a and R_a represent the current and resistance of the vehicle's accessories.

Thus, the IPC can be reformulated as:

$$\mathrm{IPC}_t = \eta_{t,T^\circ}\left(\tfrac{1}{2}\rho A C_d v_t^2 + \mu_{rr,t} m_t g \cos\phi_t + m_t g \sin\phi_t + m_t a_t\right) v_t. \tag{2.93}$$

From these formulations, two main approaches for obtaining IPC can be identified. The first involves direct measurement of battery voltage and current. The second relies on estimating the forces acting on the vehicle, which depend on several influencing factors. Temperature variations, for example, can alter battery performance and lifespan (93), while the type of terrain significantly impacts rolling resistance, slope effects, and vehicle mobility (91; 94).

Having prior knowledge of IPC along a predefined route enables effective energy management strategies: determining optimal charging points, assessing whether an EV can reach its destination with its available autonomy, and optimizing navigation resources (20; 95).

In this context, readily available satellite data offers a valuable opportunity. Besides enabling route planning between two geographic points (e.g., Google Maps, OpenStreetMap), satellite imagery and elevation profiles can provide relevant information to approximate IPC by incorporating terrain characteristics. This constitutes the central motivation of the present work.

2.5.8 IPC Based in Satellite Information Proposed Methodology

Satellite information provides valuable data for estimating the power consumption of an EV. Such information includes latitude, longitude, and elevation values on a map, which allow identification of starting and destination points. From these data, the distance between two points can be derived, and with prior knowledge of vehicle speed, the travel time can be determined. Elevation data also provides an approximation of the terrain slope. In addition, satellite maps deliver visual representations of terrain characteristics, enabling terrain classification and the association of each terrain type with its corresponding resistance effect on vehicle motion.

Approaches to modeling these effects have been proposed in the literature. For instance, Romero Schmidt and Auat (91) introduced a data acquisition methodology based on visual classification techniques using support vector machines (SVM). They established the relationship between speed and IPC consumption across four terrain types: clay, grass, gravel, and pavement. More recently, Villacrés and Auat (20) conducted experiments that collected IPC data and developed a polynomial model fitted through a piecewise regression algorithm. Their work enabled the correlation between velocity and IPC in three terrain types. Nevertheless, these studies, particularly in their experimental validation, assume constant vehicle mass and velocity and are limited to flat terrains, thereby neglecting the influence of slope.

Building upon these contributions, this work aims to estimate IPC using satellite information while explicitly considering both terrain type and slope effects. The proposed methodology is illustrated in Fig. 2.23. In this framework, satellite data provide the vehicle trajectory in terms of latitude, longitude, and altitude, together with the corresponding imagery where the path is embedded. Importantly, IPC estimation is performed *prior* to executing the trajectory. Therefore, satellite-derived vehicle speed information is not considered in this methodology.

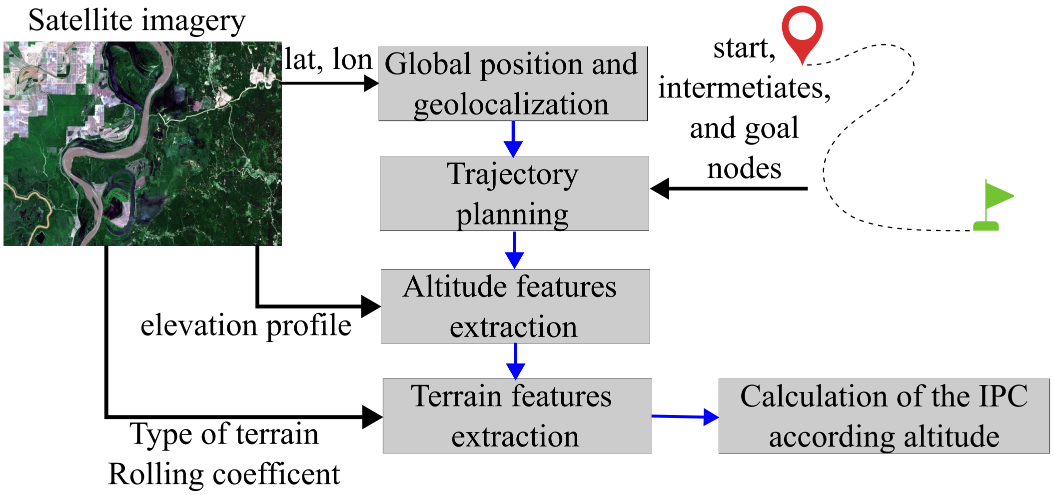

Figure 2.23: Schematic of the proposed methodology.

2.5.8.1 Global Positioning and Geolocation

The process begins by acquiring satellite information of a given city or location using platforms such as Google Maps and OpenStreetMap. This information provides latitude and longitude data, which allow for the identification of the vehicle's location in space. These coordinates can then be georeferenced onto a map. To achieve this, an image of the region is obtained, and the coordinates of its corners are known.

Georeferencing enables the transformation of latitude and longitude into x and y coordinates with respect to a reference frame. This step allows the satellite image to be processed and used consistently within the proposed methodology.

2.5.8.2 Trajectory Planning

The definition of the trajectory is essential to determine how the vehicle will travel from a starting point A to a destination point B. This involves planning a path on the map that connects A and B through intermediate points that the vehicle must traverse. Such a path can be represented as a graph, where the nodes correspond to points and the arcs represent the connections between these points.

In this methodology, the starting, intermediate, and destination nodes are arbitrarily determined to create a predefined route. However, different strategies can be employed for route construction. For instance, in urban navigation, the intermediate nodes may be determined by streets, intersections, or other infrastructure constraints. This allows the establishment of adjacency between nodes for subsequent optimization.

Since navigation is not limited to paved roads but may include different terrain types, only points that are reachable and allow continuous navigation are considered in the trajectory.

2.5.8.3 Altitude Feature Extraction

Each node along the trajectory must include both its geographical position and its elevation. While latitude and longitude data are readily available, elevation data are not freely accessible from platforms such as Google Maps or OpenStreetMap. Nevertheless, public APIs, such as Open-Elevation (open-elevation.com), allow the retrieval of elevation data by submitting latitude and longitude coordinates. Alternatively, elevation can be obtained manually from some service providers, which display on-screen altitude information.

It should be noted that elevation information is based on topographic contour lines. As such, errors may arise when determining the exact altitude of a specific point due to local surface irregularities. Nonetheless, these data are sufficient to approximate the slope between nodes.

2.5.8.4 Terrain Feature Extraction

The georeferenced satellite image provides a visual representation of different terrain types. For example, streets typically appear as gray, grass or wooded areas as green, and dirt or clay surfaces as brown. This makes it possible to label the arcs between nodes based on the terrain that the vehicle will encounter.

In this methodology, terrain labeling was carried out manually. Each node was categorized into three terrain types: pavement, clay, and gravel—based on the surrounding color in the satellite image (light gray, brown, and dark gray, respectively). However, automated classification techniques based on image processing and machine learning, such as those proposed in (91; 20), may also be applied to improve scalability and objectivity.

2.5.8.5 Calculation of the IPC

To estimate the IPC along the trajectory, the distance and slope between adjacent nodes must first be calculated.

The distance between nodes is computed using the Euclidean distance formula, as expressed in Equation (2.94). Here, the height difference is assumed negligible compared to horizontal distance:

$$d_{ij} = \sqrt{(x_i - x_j)^2 + (y_i - y_j)^2} \tag{2.94}$$

where d_{ij} represents the distance between nodes i and j, and (x_i, y_i) and (x_j, y_j) denote their respective coordinates.

The elevation angle between nodes is computed using Equation (2.95), where $H(n_i)$ and $H(n_j)$ represent the elevations at nodes i and j, respectively:

$$\theta_{ij} = \arctan\left(\frac{|H(n_j) - H(n_i)|}{d_{ij}}\right). \tag{2.95}$$

Finally, the IPC is calculated for each pair of nodes using Equation (2.93), considering a predefined vehicle speed, the vehicle mass (including passengers and cargo), the elevation angle, the terrain type, and its associated rolling resistance coefficient. Since the travel time between nodes is also known, the energy consumption can be estimated for the entire route by summing the contribution of each segment until the destination is reached.

2.5.9 Experiments

This section presents the results of the computational experiments carried out using the proposed methodology, along with the details of the experimental setup and the validation procedure. Table 2.5 summarizes the types of experiments performed and the data used in each case.

In the computational experiments, the variables such as velocity, acceleration, node position, and altitude were predefined or obtained through public APIs, and the IPC was computed using the proposed model. In the field experiments, these variables were directly measured using sensors (e.g., IMU and RTK), and IPC was subsequently calculated. Finally, direct measurement of IPC was obtained from the batteries during real experiments and used for validation of the methodology.

Table 2.5: Types of experiments and corresponding data setup for obtaining IPC.

Experiment	**Velocity (m/s)**	**Acceleration (m/s^2)**	**Node Position (lat, lon)**	**Altitude (m)**	**IPC (W)**
Computational experiment	defined	defined	defined	API	calculated
Field experiment	measured (IMU)	measured (IMU)	measured (RTK)	measured (RTK)	calculated
Direct measurement	–	–	–	–	measured

2.5.9.1 Computational Experiments

The computational experiments were conducted using a satellite map of the facilities of the Universidad Técnica Federico Santa María, located in Viña del Mar, Valparaíso, Chile.

A satellite image of the study area was obtained from Google Maps using the Sas Planet 2022 software. The image covered three different terrains of interest: gravel, clay, and pavement. The latitude and longitude coordinates of the upper-left (−33.03856107, −71.48669920) and lower-right (−33.04012602, −71.48467145) corners of the image were collected for georeferencing purposes. The image and coordinates were transformed into meters for distance analysis between nodes and into pixels for image interaction, as shown in Figure 2.24a (north oriented upwards).

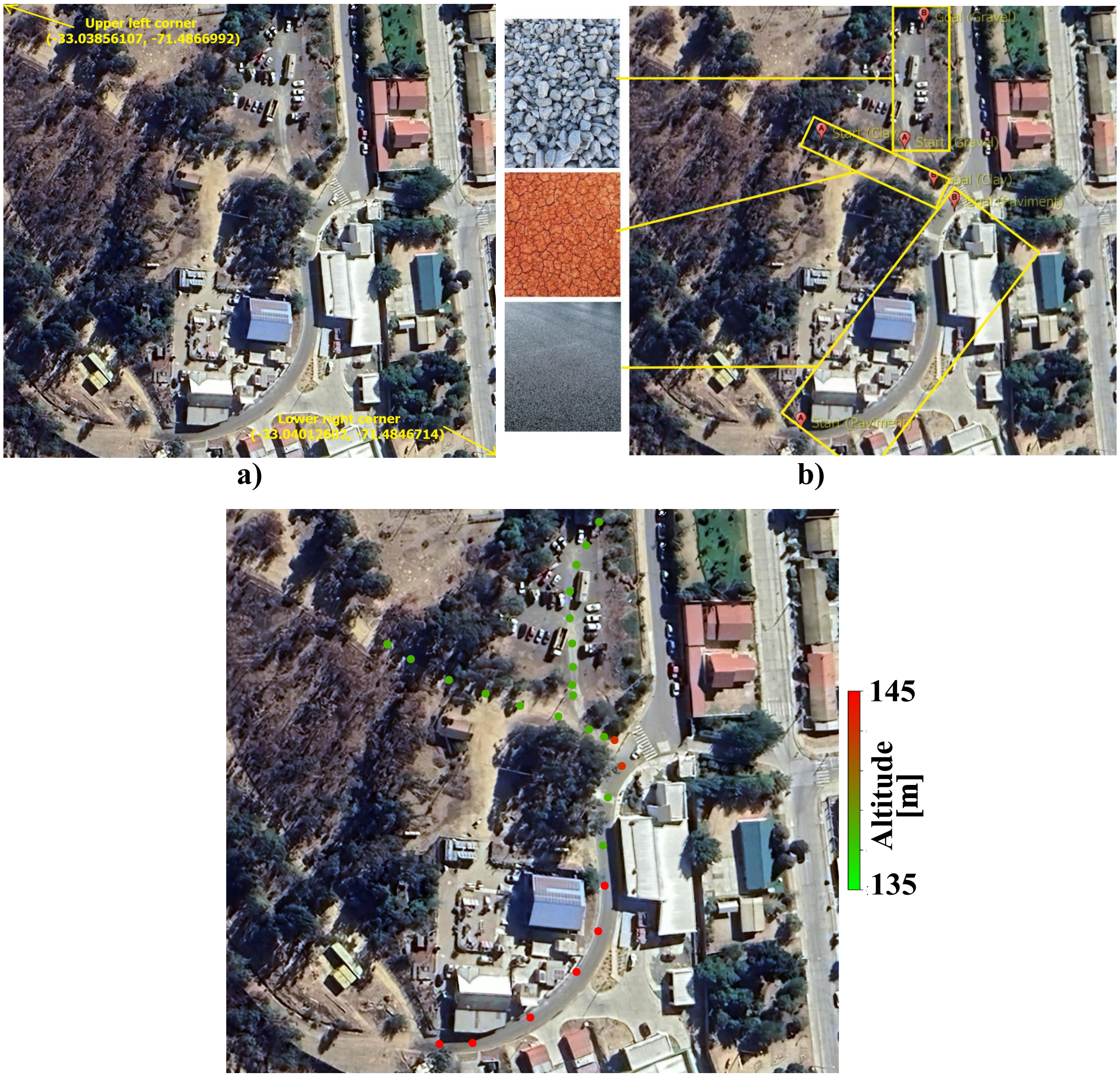

a)

b)

c)

Figure 2.24: Selected area of the facilities of Universidad Técnica Federico Santa María, Viña del Mar, Valparaíso, Chile (https://goo.gl/maps/yscek8oYisThQJTT6, accessed on 12 July 2023). a) Map Georreferenciated. b) Designed trajectories over gravel, clay, and pavement terrains (ordered from top to bottom). c) Nodes of trajectories over gravel, clay, and pavement, colored according to altitude. Red indicates maximum altitude and green indicates minimum altitude.

The starting and ending points of each trajectory were defined to construct three routes corresponding to the gravel, clay, and pavement surfaces. These routes are depicted in Figure 2.24b, with point A representing the start and point B the destination.

Each trajectory was discretized into eight nodes, including the start, intermediate, and destination nodes, which were evenly spaced. The longest trajectory covered a total distance of 105 m. Once the nodes were determined, their elevations were obtained using the Open-Elevation API based on their latitude and longitude coordinates (see Figure 2.24c).

With the nodes and their corresponding data available, the distance and slope between each pair of adjacent nodes were computed. To calculate the IPC, specific parameters were defined in advance. The vehicle speed was set to 5 m/s for pavement, 4 m/s for clay, and 3 m/s for gravel. These values were essential to determine the travel time between trajectory segments. Given these speeds, the effect of aerodynamic drag on the vehicle was assumed to be negligible due to its quadratic dependence on velocity.

The IPC calculations revealed distinct variations depending on both the terrain type and the slope along each trajectory, highlighting the influence of environmental conditions on energy consumption.

2.5.9.2 Experimental Setup

The experimental study was conducted using a Cushman Hauler Pro electric vehicle. This vehicle is equipped with an AC motor and provides seating capacity for two passengers. To obtain accurate positioning data along the route, a Real-Time Kinematics (RTK) system was installed on the roof of the vehicle.

Table 2.6 summarizes the hardware used in the setup, including the specifications of the electric vehicle, the RTK GNSS (Navcom SF-3040), the IMU (Vectornav VN-200), the voltage and current sensors, and the on-board processing unit (Nvidia Jetson TX2).

The vehicle speed was estimated based on the predefined route and sampling time. An Inertial Measurement Unit (IMU) Vectornav VN-200 was installed to measure the vehicle's inclination and, consequently, to compute the slopes encountered during the trials. Additionally, a voltage and current sensor was connected directly to the batteries in order to calculate the IPC.

Table 2.6: Characteristics of the hardware setup.

Name	Description
Electric Vehicle: Cushman Hauler Pro	
Motor	72 Vac; 16.7 kW at peak torque
Max. Speed	80 km/h
Nominal Speed	23.3 km/h ± 0.8 km/h
Curb Weight	411 kg
RTK GNSS: Navcom SF-3040	
Horizontal Accuracy (<40 km)	1 cm + 0.5 ppm
Vertical Accuracy (<40 km)	2 cm + 1 ppm
Data Rate	Selectable between 1 Hz, 5 Hz, and 10 Hz
Communication	Serial port via USB
IMU: Vectornav VN-200	
Data Rate	800 Hz
Dynamic Heading Accuracy	0.02 degrees
Dynamic Pitch/Roll Accuracy	0.03 degrees
Voltage and Current Sensor	
Voltage Range	15 V to 80 V
Current Range	−300 A to 300 A
Precision	12-bit ADC
Sampling Rate	800 Hz (average)
Communication	Serial port via USB
On-Board Computer: Nvidia Jetson TX2	
GPU	NVIDIA Pascal^{TM}, 256 CUDA cores
CPU	HMP Dual Denver 2/2 MB L2 + Quad ARM® A57/2 MB L2
Memory	8 GB 128-bit LPDDR4, 59.7 GB/s

[1] Provided by the manufacturer.

This design enables accurate measurement and monitoring of voltage and current, thereby allowing the reliable estimation of IPC in the study.

All information from the RTK, IMU, and IPC sensors was acquired and processed by the on-board computer, running the Ubuntu operating system with Robot Operating System (ROS) implemented. Figure 2.25 shows the experimental platform and the mounted sensors used for field testing.

Figure 2.25: Electric vehicle used for field testing, equipped with an RTK GNSS system, an IMU, and a voltage/current sensor connected to the batteries for IPC measurement.

2.5.9.3 Field Experiments

Field tests were conducted at the facilities of the Universidad Técnica Federico Santa María in Viña del Mar, Valparaíso, Chile. Three routes were established, each corresponding to a different terrain type: pavement, clay, and gravel, based on the simulation trajectories.

The experiments consisted of the following:

- 10 trials on pavement terrain,
- 10 trials on clay terrain,
- 10 trials on gravel terrain.

In each trial, measurements from the RTK, IMU, and IPC sensors were collected along the respective trajectory. The main objectives were to visualize the effect of elevation on IPC and to obtain global position data for trajectory reconstruction. The data were processed considering the velocity and acceleration behavior, and a reference IPC was obtained by direct measurement from the EV batteries.

Figure 2.26 shows the RTK nodes with their corresponding altitudes. The vehicle traveled from the lowest altitude zone to the highest altitude zone, encountering a positive elevation angle for most of the route.

Figure 2.26: Nodes and altitudes measured along each trajectory.

2.6 Results

Figure 2.27 presents the raw data collected from the RTK, IMU, and IPC sensors across the three terrain types. Height, velocity, acceleration, and IPC data are shown with respect to the number of synchronized measurements. Synchronization was performed using the slowest sensor, the RTK, operating with a sampling time of 0.3 s.

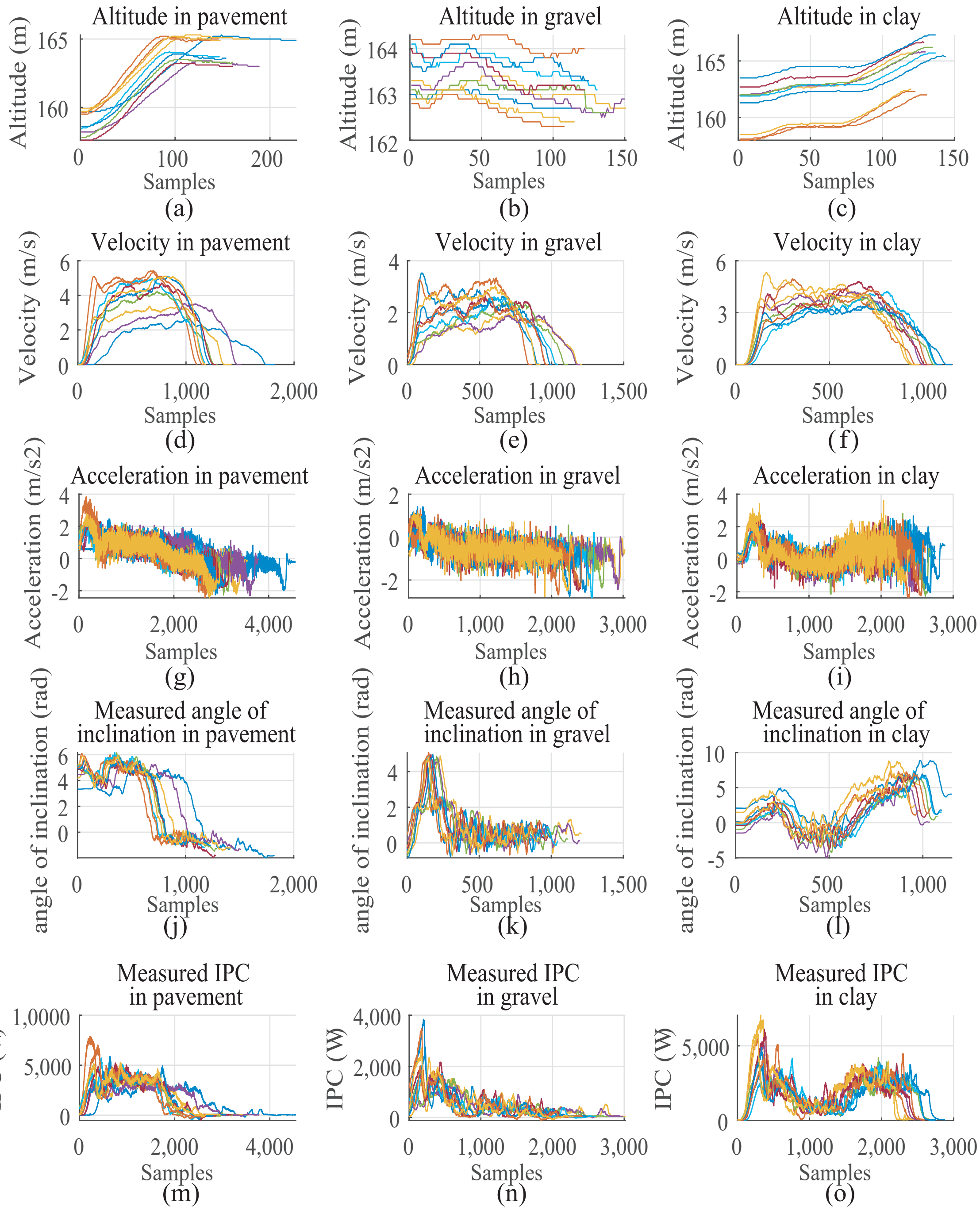

Figure 2.27: Raw data. (**a**–**c**) Altitude profiles on pavement, gravel, and clay. (**d**–**f**) Vehicle speed measured with the IMU. (**g**–**i**) Acceleration profiles on the three terrains. (**j**–**l**) Inclination angle from IMU pitch data. (**m**–**o**) IPC measured from the EV batteries.

On pavement (Figure 2.27a), the altitude fluctuates at the beginning of the run. In gravel (Figure 2.27b), variations appear even on seemingly flat terrain, reflecting route irregularities and sensor sensitivity. In clay (Figure 2.27c), the trajectory resembles the pavement case, starting at a lower altitude and gradually ascending, though some trials show deviations likely due to dense vegetation interfering with RTK signals. Importantly, only altitude variations are required for slope estimation in later calculations.

The speed profiles highlight terrain effects. On pavement (Figure 2.27d), speeds remain close to 5 m/s, though manual driving introduced acceleration and braking effects at the start and end. On gravel (Figure 2.27e), variability is greater, with sliding and skidding observed in situ. On clay (Figure 2.27f), speed behavior is stable, with trials converging near 4 m/s.

Acceleration data (Figures 2.27g–i) exhibit noisy fluctuations near zero, with peaks at startup and braking. Inclination angles derived from IMU pitch (Figures 2.27j–l) mirror the altitude trends: pavement shows a pronounced initial slope flattening towards zero, gravel displays noisy jumps, and clay reveals two distinct slopes separated by a flat section.

The IPC measured directly from the battery (Figures 2.27m–o) strongly correlates with slope variations, following similar shapes to the altitude profiles.

To compare estimates with measured IPC, the simplified longitudinal dynamics model in Equation 2.96 was applied:

$$IPC_t = (\mu_{rr,t} m_t g \cos\phi_t + m_t g \sin\phi_t + m_t a_t)\, v_t \tag{2.96}$$

Figure 2.28 shows estimated IPC against time (Figures 2.28a–c) and measured IPC (Figures 2.28d–f), along with IPC–velocity relations for estimated (Figures 2.28g–i) and measured values (Figures 2.28j–l). On pavement, estimates closely resemble battery measurements. On gravel, IPC values fluctuate more due to slope variability and intermittent wheel–ground contact, sometimes producing negative IPC linked to regenerative braking. On clay, the estimated and measured curves align closely.

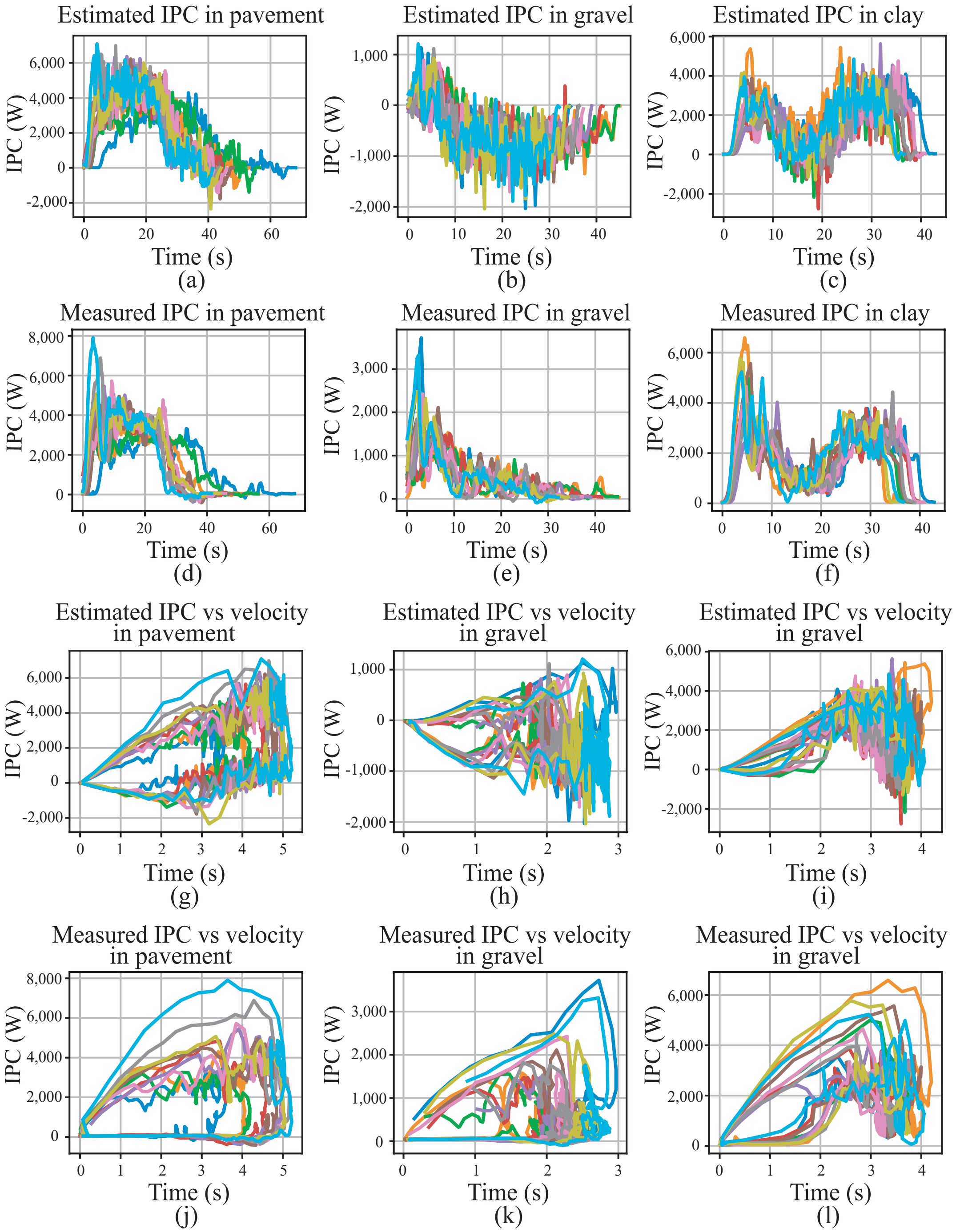

Figure 2.28: IPC results. (**a**–**c**) Estimated IPC on pavement, gravel, and clay. (**d**–**f**) Measured IPC. (**g**–**i**) Estimated IPC vs. velocity. (**j**–**l**) Measured IPC vs. velocity. Positive and negative IPC values appear, reflecting acceleration, braking, slope, and terrain effects.

Figure 2.29 summarizes averages and standard deviations of estimated and measured IPC. Although standard deviations are high—consistent with real-world variability—the averages show strong agreement across all terrains.

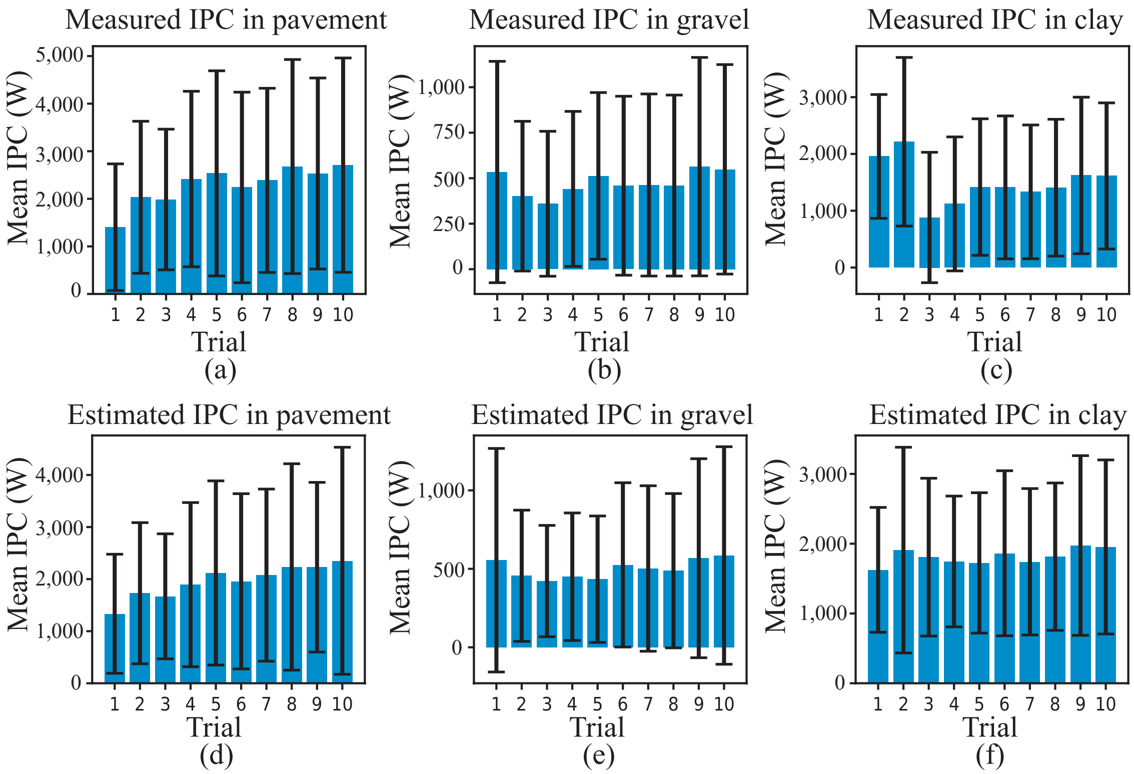

Figure 2.29: Comparison of IPC in field trials. (**a**–**c**) Average measured IPC with standard deviation for pavement, gravel, and clay. (**d**–**f**) Average estimated IPC using sensor data.

Finally, Figure 2.30 compares computational experiments, field estimates, and direct measurements. Computational experiments yielded errors of 5.43% (clay), 19.19% (pavement), and 102.20% (gravel). The high gravel error is attributed to satellite resolution limitations and terrain phenomena such as skidding and wheel sinkage. In contrast, field-based estimates with RTK and IMU achieved errors of 5.11% (gravel), 14.50% (pavement), and 21.25% (clay), demonstrating closer alignment with battery measurements.

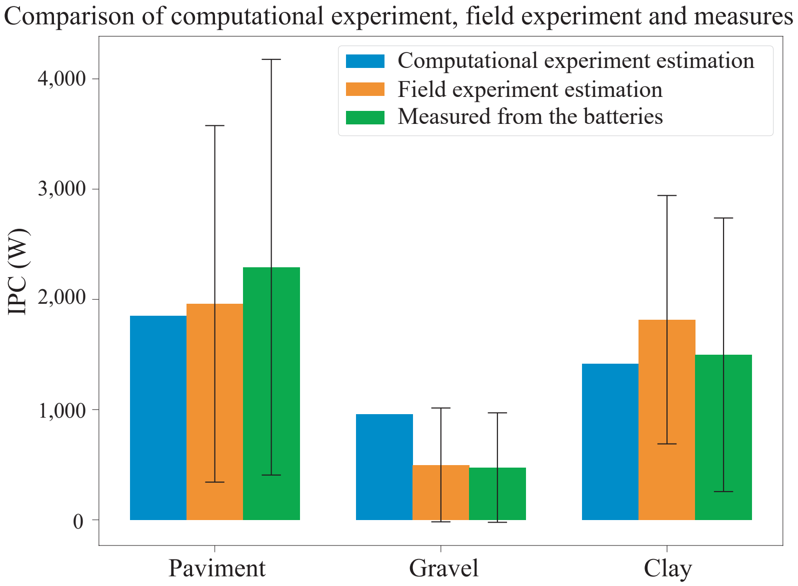

Figure 2.30: Average IPC values for pavement, gravel, and clay. Comparison among computational estimation (satellite), experimental estimation (RTK/IMU), and direct battery measurements.

3 | Methodology

This chapter describes the methodological framework developed to model the dynamics and power consumption of a generalized N-Trailer system operating in off-road environments. The methodology is organized into three main components: the formulation of the system dynamics, the modeling of terrain interaction and regenerative braking, and the computational estimation of instantaneous power.

3.1 Generalized Dynamic Model of the N-Trailer System

The N-Trailer system is composed of a unicycle-like tractor and multiple passive trailers connected via articulated joints. The model accounts for longitudinal, lateral, and vertical dynamics, with emphasis on the physical constraints and terrain-induced loads that affect off-road operation.

3.1.1 Kinematic Structure

The position and orientation of each trailer are defined recursively based on the configuration of the preceding segment. The kinematic chain captures nonholonomic constraints and ensures consistent motion propagation along the system.

3.1.2 Dynamic Formulation

Using the Euler-Lagrange formalism, the system's equations of motion are derived by defining the total kinetic and potential energy of the N-Trailer configuration. This formulation accommodates generalized coordinates and allows for the systematic inclusion of external forces and non-conservative effects.

Key dynamic effects considered include:

- **Inertial coupling** across articulated joints,
- **Gravitational and slope-induced** forces,
- **Lateral interaction** due to curvature and trailer configuration.

The model also incorporates load variation and mass distribution effects, which are critical for realistic energy estimation in agricultural and mining contexts.

3.2 Modeling Wheel-Terrain Interaction and Regenerative Braking

Energy losses and traction performance in off-road environments are significantly influenced by soil characteristics and braking mechanisms. This section describes how such phenomena are integrated into the dynamic model.

3.2.1 Dynamic Friction Modeling with LuGre

Wheel-soil interaction is modeled using the LuGre dynamic friction model. It captures pre-sliding displacement, stick-slip behavior, and velocity-dependent friction losses. This allows for accurate estimation of traction forces and rolling resistance under different terrain types.

3.2.2 Terrain and Slope Parameterization

Three representative terrains, gravel, clay, and pavement, are characterized based on literature-derived parameters such as rolling resistance coefficient, soil stiffness, and slope profiles. These are used to parameterize the terrain-dependent terms in the model.

3.2.3 Integration of Regenerative Braking

A regenerative braking model is incorporated by calculating the negative torque contribution during deceleration phases. The available regenerative power is constrained by motor, inverter, and battery efficiencies, as well as dynamic conditions of slope and mass distribution.

The instantaneous power consumption is computed as:

$$IPC(t) = \frac{(F_{rr}(t) + F_{hill}(t) + F_{aero}(t) + F_{acc}(t)) \cdot v(t)}{\eta_{\text{sys}}} \tag{3.1}$$

with:

- $F_{rr}(t)$: Rolling resistance,
- $F_{hill}(t)$: Gravitational force component due to slope,
- $F_{aero}(t)$: Aerodynamic drag,
- $F_{acc}(t)$: Inertial acceleration force,
- η_{sys}: Composite drivetrain efficiency.

3.3 Computational Implementation and Scenario Analysis

The proposed modeling framework has been implemented both symbolically and numerically using the Python programming language. The symbolic formulation, developed through a computer algebra system, serves as the foundation for generating explicit expressions of the dynamic model, the generalized forces, and the instantaneous power consumption terms. This symbolic stage enables a systematic parametric exploration of key variables such as terrain gradient, vehicle mass distribution, trailer geometry, and wheel–soil contact properties. Furthermore, symbolic manipulation facilitates the direct incorporation of model extensions, including alternative friction formulations or additional regenerative braking schemes, without requiring a complete reimplementation of the numerical solver.

The numerical implementation, in turn, transforms the symbolic equations into efficient simulation routines capable of producing detailed instantaneous power consumption (IPC) profiles for arbitrary trajectories. These simulations are configured to capture the temporal evolution of mechanical and electrical power demand under a variety of operating conditions. By leveraging numerical integration methods, it is possible to explore dynamic effects arising from acceleration phases, deceleration events, and steady-state motion, while retaining the fidelity of the underlying nonlinear model.

Scenario analysis constitutes an essential methodological component of this work. Rather than relying on field experiments or high-fidelity robotic simulations, validation is achieved through rigorous internal consistency checks, comparative analysis with established energy bounds, and the examination of limiting-case behaviors. Examples of such cases include constant-velocity motion on uphill and downhill slopes, variations in total system mass to represent different payload conditions, and the evaluation of sharp turning maneuvers where dynamic coupling effects become pronounced. These scenarios have been selected to reflect operational conditions typically encountered in agricultural, forestry, and mining environments, characterized by irregular terrain, variable topography, and load fluctuations. The analysis also considers representative ranges of friction coefficients and regenerative braking efficiencies, allowing the assessment of the model's sensitivity to both mechanical and electromechanical parameters.

Through this computational methodology, it is possible to identify the influence of each subsystem and environmental factor on the overall energy demand of the generalized N-Trailer system. This enables not only the prediction of expected performance in given scenarios but also the evaluation of design trade-offs, such as the number of trailers, mass distribution strategies, or motor sizing requirements. Ultimately, the symbolic–numerical integration ensures that the results are both physically interpretable and computationally efficient, thereby supporting reproducibility and future model extensions.

3.4 Summary

The methodology developed in this thesis provides a unified framework for estimating the instantaneous power consumption of generalized N-Trailer systems in off-road environments. By integrating dynamic coupling effects, advanced friction modeling, and regenerative braking mechanisms within an Euler–Lagrange formalism, the approach achieves a comprehensive yet analytically tractable representation of the system's energetic behavior. The symbolic formulation enables parameter-driven exploration and facilitates the derivation of reduced or specialized models, while the numerical simulation stage delivers high-resolution predictions for specific operational scenarios.

This dual-stage methodology supports a wide range of applications, from early-stage vehicle concept evaluation to mission planning and energy-aware configuration of articulated electric platforms. In particular, it enables decision-makers to assess the implications of trailer configurations, payload variations, and terrain conditions without the cost or logistical complexity of field testing. By maintaining a clear separation between the modeling, simulation, and scenario analysis phases, the framework also ensures adaptability, allowing its extension to incorporate real-world sensor data, control strategies, or optimization-based design processes in future work.

Overall, the computational implementation and scenario-driven validation strategy presented here form a rigorous methodological basis for advancing the understanding of energy consumption in N-Trailer systems, providing a robust toolset for both academic research and engineering practice in the domains of agricultural robotics, off-road mobility, and energy-efficient vehicle design.

4 | Dynamic Modeling of the N-Trailer System

This chapter presents the derivation of the dynamic model for a generalized N-Trailer system composed of a unicycle-like tractor and passive trailers. The model includes the full Euler-Lagrange formulation, the integration of wheel-terrain interaction, and the computation of instantaneous power consumption. These developments form the basis for evaluating energetic performance under different terrain and configuration scenarios.

4.1 Description of the N-Trailer System

Based on the concepts introduced in the methodology, an N-trailer system consists of a tractor vehicle to which multiple trailers are connected via rigid or articulated joints. This structure allows the tractor to be the only active component, while the trailers follow passively. The dynamics of the system are significantly influenced by geometric layout, load distribution, and terrain characteristics.

The tractor is modeled as a unicycle vehicle with front-wheel steering, and the trailers are subject to kinematic constraints that ensure their alignment and stability. This system is widely used in off-road applications such as agriculture and mining, where efficient navigation over complex terrain is essential.

This section models the dynamics of such vehicles, beginning with the unicycle as a basic form, and progressively extending to a single trailer and its generalization.

4.2 Unicycle Modeling

To derive the kinematic equations of a unicycle-type vehicle, it is essential to express the positions of the left and right wheels, as follows:

$$\overrightarrow{p}_{r_0} = (x + b_0 \sin\theta_0)\,\hat{\mathbf{i}} \;+\; (y - b_0 \cos\theta_0)\,\hat{\mathbf{j}} \tag{4.1}$$

$$\overrightarrow{p}_{l_0} = (x - b_0 \sin\theta_0)\,\hat{\mathbf{i}} \;+\; (y + b_0 \cos\theta_0)\,\hat{\mathbf{j}} \tag{4.2}$$

where $\vec{p}_{r0}$ and $\vec{p}_{l0}$ represent the position vectors of the unicycle's wheels. The velocities of both wheels are obtained by differentiating the position vectors:

$$\overrightarrow{v}_{r_0} = (\dot{x} + b_0\dot{\theta}_0 \cos\theta_0)\,\hat{\mathbf{i}} \;+\; (\dot{y} + b_0\dot{\theta}_0 \sin\theta_0)\,\hat{\mathbf{j}} \tag{4.3}$$

$$\overrightarrow{v}_{l_0} = (\dot{x} - b_0\dot{\theta}_0 \cos\theta_0)\,\hat{\mathbf{i}} \;+\; (\dot{y} - b_0\dot{\theta}_0 \sin\theta_0)\,\hat{\mathbf{j}} \tag{4.4}$$

The configuration of the unicycle including the wheel angles is given by:

$$\vec{q} = \begin{bmatrix} x & y & \theta_0 & \theta_{r0} & \theta_{l0} \end{bmatrix}^T \tag{4.5}$$

To impose nonholonomic constraints such as the no-slip condition, the body velocity is projected along the normal component $(-\sin\theta_0, \cos\theta_0)$, yielding:

$$-\dot{x}\sin\theta_0 + \dot{y}\cos\theta_0 = 0 \tag{4.6}$$

Similarly, wheel constraints are derived by projecting the wheel velocities onto $(\cos\theta_0, \sin\theta_0)$:

$$\dot{x}\cos\theta_0 + \dot{y}\sin\theta_0 + b_0\dot{\theta}_0 - r\dot{\theta}_{r0} = 0 \tag{4.7}$$

$$\dot{x}\cos\theta_0 + \dot{y}\sin\theta_0 - b_0\dot{\theta}_0 - r\dot{\theta}_{l0} = 0 \tag{4.8}$$

The constraints in equations 4.6–4.8 can be written compactly as $A(\vec{q})\dot{\vec{q}} = 0$, where $A(\vec{q})$ is the Jacobian matrix of the constraints:

$$A(q) = \begin{bmatrix} -\sin\theta_0 & \cos\theta_0 & 0 & 0 & 0 \\ \cos\theta_0 & \sin\theta_0 & b_0 & -r & 0 \\ \cos\theta_0 & \sin\theta_0 & -b_0 & 0 & -r \end{bmatrix} \tag{4.9}$$

These constraints define the relationship between wheel velocities $\vec{v} = [\dot{\theta}_{r0}, \dot{\theta}_{l0}]^T$ and the generalized velocity vector $\dot{\vec{q}}$. The mapping is given by $\dot{\vec{q}} = S(\vec{q})\vec{v}$, where $S(\vec{q})$ is the null space matrix of $A(\vec{q})$:

$$S(q) = \begin{bmatrix} \frac{r}{2}\cos\theta_0 & \frac{r}{2}\cos\theta_0 \\ \frac{r}{2}\sin\theta_0 & \frac{r}{2}\sin\theta_0 \\ \frac{r}{2b_0} & -\frac{r}{2b_0} \\ 1 & 0 \\ 0 & 1 \end{bmatrix} \tag{4.10}$$

To derive the dynamic model, the Euler-Lagrange method with Lagrange multipliers is used to incorporate the constraints:

$$\frac{d}{dt}\left(\frac{\partial L}{\partial \dot{q}_k}\right) - \left(\frac{\partial L}{\partial q_k}\right) = f_k - \sum_{i=1}^{n} \lambda_i a_{ik} \tag{4.11}$$

where n is the number of kinematic constraints, λ_i the Lagrange multipliers, f_k the generalized force, and L is the Lagrangian.

Assuming planar motion and inertial effects of the wheels, the Lagrangian L equals the total kinetic energy:

$$T = \tfrac{1}{2}(m_0 v_0^2 + I_0 \dot{\theta}_0^2) + \tfrac{1}{2}(m_w v_{r0}^2 + I_w \dot{\theta}_{r0}^2) + \tfrac{1}{2}(m_w v_{l0}^2 + I_w \dot{\theta}_{l0}^2) \tag{4.12}$$

Substituting (4.12) into (4.11) and simplifying leads to the compact form:

$$M(\vec{q})\ddot{\vec{q}} + C(\vec{q}, \dot{\vec{q}}) = B(\vec{q})\vec{U} + A^T(\vec{q})\vec{\lambda} \tag{4.13}$$

where M is the mass-inertia matrix, C is the Coriolis term, B the actuation input matrix, and $\vec{\lambda}$ the vector of Lagrange multipliers.

Including external forces, the equation becomes:

$$M(\vec{q})\ddot{\vec{q}} + C(\vec{q}, \dot{\vec{q}}) + f(\dot{\vec{q}}) = B(\vec{q})\vec{U} + A^T(\vec{q})\vec{\lambda} \tag{4.14}$$

The matrix $M(\vec{q})$ is given by:

$$M = \begin{bmatrix} m_0 + 2m_w & 0 & 0 & 0 & 0 \\ 0 & m_0 + 2m_w & 0 & 0 & 0 \\ 0 & 0 & I_0 + 2b_0^2 m_w & 0 & 0 \\ 0 & 0 & 0 & i_w & 0 \\ 0 & 0 & 0 & 0 & i_w \end{bmatrix} \tag{4.15}$$

The Coriolis matrix $C(\vec{q}, \dot{\vec{q}})$ is:

$$C(q, \dot{q}) = \begin{pmatrix} -a_0 m_0 \dot{\theta}_0^2 \cos\theta_0 \\ -a_0 m_0 \dot{\theta}_0^2 \sin\theta_0 \\ 0 \\ 0 \\ 0 \end{pmatrix} \tag{4.16}$$

This completes the full derivation of the unicycle dynamics using Euler-Lagrange theory, forming the basis for extension to trailer-coupled systems.

4.3 G1T System Modeling

The G1T system is an extension of the unicycle model in which a single trailer is attached to the main vehicle via an intermediate articulated joint. This configuration increases the complexity of the system dynamics by introducing additional degrees of freedom and constraints. To derive the kinematic and dynamic equations of a G1T (Generalized 1-Trailer), the positions and velocities of the wheels of both the tractor and the trailer must be defined explicitly.

4.3.1 Wheel Position Vectors

The position vectors of the right and left wheels of the tractor and trailer are given by:

$$\vec{p}_{r_0} = (x + b_0 \sin\theta_0)\,\hat{\mathbf{i}} + (y - b_0 \cos\theta_0)\,\hat{\mathbf{j}} \tag{4.17}$$

$$\vec{p}_{l_0} = (x - b_0 \sin\theta_0)\,\hat{\mathbf{i}} + (y + b_0 \cos\theta_0)\,\hat{\mathbf{j}} \tag{4.18}$$

$$\begin{aligned}\vec{p}_{r_1} = {} & (x - L_{h1}\cos\theta_0 - L_1\cos\theta_1 + b_1\sin\theta_1)\,\hat{\mathbf{i}} \\ & + (y - L_{h1}\sin\theta_0 - L_1\sin\theta_1 - b_1\cos\theta_1)\,\hat{\mathbf{j}}\end{aligned} \tag{4.19}$$

$$\begin{aligned}\vec{p}_{l_1} = {} & (x - L_{h1}\cos\theta_0 - L_1\cos\theta_1 - b_1\sin\theta_1)\,\hat{\mathbf{i}} \\ & + (y - L_{h1}\sin\theta_0 - L_1\sin\theta_1 + b_1\cos\theta_1)\,\hat{\mathbf{j}}\end{aligned} \tag{4.20}$$

4.3.2 Wheel Velocity Vectors

Differentiating the position vectors with respect to time yields the wheel velocity vectors:

$$\vec{v}_{r_0} = (\dot{x} + b_0\dot{\theta}_0\cos\theta_0)\,\hat{\mathbf{i}} + (\dot{y} + b_0\dot{\theta}_0\sin\theta_0)\,\hat{\mathbf{j}} \tag{4.21}$$

$$\vec{v}_{l_0} = (\dot{x} - b_0\dot{\theta}_0\cos\theta_0)\,\hat{\mathbf{i}} + (\dot{y} - b_0\dot{\theta}_0\sin\theta_0)\,\hat{\mathbf{j}} \tag{4.22}$$

$$\begin{aligned}\vec{v}_{r_1} = {} & (\dot{x} + L_{h1}\dot{\theta}_0\sin\theta_0 + L_1\dot{\theta}_1\sin\theta_1 + b_1\dot{\theta}_1\cos\theta_1)\,\hat{\mathbf{i}} \\ & + (\dot{y} - L_{h1}\dot{\theta}_0\cos\theta_0 - L_1\dot{\theta}_1\cos\theta_1 + b_1\dot{\theta}_1\sin\theta_1)\,\hat{\mathbf{j}}\end{aligned} \tag{4.23}$$

$$\begin{aligned}\vec{v}_{l_1} = {} & (\dot{x} + L_{h1}\dot{\theta}_0\sin\theta_0 + L_1\dot{\theta}_1\cos\theta_1 - b_1\dot{\theta}_1\sin\theta_1)\,\hat{\mathbf{i}} \\ & + (\dot{y} - L_{h1}\dot{\theta}_0\sin\theta_0 - L_1\dot{\theta}_1\sin\theta_1 - b_1\dot{\theta}_1\cos\theta_1)\,\hat{\mathbf{j}}\end{aligned} \tag{4.24}$$

4.3.3 Generalized Coordinates

The complete state vector $\vec{q}$ for the G1T system includes all positional and angular components:

$$\vec{q} = \begin{bmatrix} x & y & \theta_0 & \theta_1 & \theta_{r1} & \theta_{l1} & \theta_{r0} & \theta_{l0} \end{bmatrix}^T \tag{4.25}$$

4.3.4 Nonholonomic Constraints

The system is subject to the following nonholonomic (no-slip) constraints, expressed compactly as $A(\vec{q})\dot{\vec{q}} = 0$. These include lateral and longitudinal no-slip constraints for both the tractor and trailer. The Jacobian matrix $A(\vec{q})$ is defined based on projections of velocities onto directions orthogonal and tangential to the wheels.

4.3.5 Lagrangian Dynamics

To derive the equations of motion, the Euler-Lagrange method is applied using the total kinetic energy of the system. The dynamic model in the presence of constraints is:

$$M(\vec{q})\ddot{\vec{q}} + C(\vec{q}, \dot{\vec{q}}) + f(\dot{\vec{q}}) = B(\vec{q})\vec{U} + A^T(\vec{q})\vec{\lambda} \tag{4.26}$$

where M is the mass-inertia matrix, C is the Coriolis vector, f external forces (e.g., terramechanics), B the actuation matrix, and $\vec{\lambda}$ the Lagrange multipliers enforcing the constraints.

4.3.6 Reduced Dynamics

To express the dynamics in reduced form, we apply the null-space matrix $S(\vec{q})$:

$$\bar{M} = S^T M S \tag{4.27}$$

$$\bar{C} = S^T (C + M\dot{S}\vec{v}) \tag{4.28}$$

$$\bar{f} = S^T f \tag{4.29}$$

$$\bar{B} = S^T B \tag{4.30}$$

$$\dot{\vec{v}} = \bar{M}^{-1}(\bar{B} - \bar{C} - \bar{f}) \tag{4.31}$$

This completes the dynamic modeling of the G1T system as an extension of the unicycle using the Euler-Lagrange formulation, consistent with the previously introduced notations and symbolic definitions.

4.4 GNT Dynamic Model

To generalize the dynamic modeling of the Generalized N-Trailer (GNT) system, we define the generalized coordinates vector as:

$$q = [x, y, \psi_0, \ldots, \psi_N, \psi_{rN}, \psi_{lN}, \ldots, \psi_{r0}, \psi_{l0}] \tag{4.32}$$

where:

- x, y, ψ_0: represent the pose of the tractor.
- $\psi_1, \ldots, \psi_N$: are the orientations of trailers relative to the global frame.
- ψ_{r0}, ψ_{l0}: are the angular positions of the right and left wheels of the tractor (actuated wheels).
- $\psi_{r1}, \psi_{l1}, \ldots, \psi_{rN}, \psi_{lN}$: are the angular positions of the right and left wheels of each trailer (passive wheels).

The dynamics of the GNT are derived using the Euler-Lagrange method. The Lagrangian is defined as:

$$L(q, \dot{q}) = T(q, \dot{q}) - V(q) \tag{4.33}$$

where the kinetic energy is:

$$T(q,\dot{q}) = \frac{1}{2}\dot{q}^T M(q)\dot{q} \tag{4.34}$$

To enforce the nonholonomic constraints, we augment the Lagrangian with Lagrange multipliers λ:

$$L^*(q,\dot{q},\lambda) = L(q,\dot{q}) + \lambda^T (A(q)\dot{q}) \tag{4.35}$$

Non-conservative forces, such as rolling resistance and aerodynamic drag, are represented as:

$$Q_{nc}(q,\dot{q}) = Q_{rr}(q,\dot{q}) + Q_{ad}(q,\dot{q}) \tag{4.36}$$

Applying the Euler-Lagrange equation to L^* gives:

$$\frac{d}{dt}\left(\frac{\partial L^*}{\partial \dot{q}}\right) - \frac{\partial L^*}{\partial q} = \tau + Q_{nc}(q,\dot{q}) \tag{4.37}$$

Computing each term yields:

$$\frac{\partial L^*}{\partial \dot{q}} = M(q)\dot{q} + A(q)^T \lambda \tag{4.38}$$

$$\frac{d}{dt}\left(M(q)\dot{q} + A(q)^T \lambda\right) = M(q)\ddot{q} + \dot{M}(q)\dot{q} + \frac{d}{dt}[A(q)^T \lambda] \tag{4.39}$$

$$\frac{\partial L^*}{\partial q} = \frac{1}{2}\dot{q}^T \frac{\partial M(q)}{\partial q}\dot{q} - \nabla_q V(q) + \left(\frac{\partial [A(q)\dot{q}]}{\partial q}\right)^T \lambda \tag{4.40}$$

Combining these, the dynamic model becomes:

$$M(q)\ddot{q} + \left[\frac{\partial M(q)}{\partial q}\dot{q}\right]\dot{q} - \frac{1}{2}\dot{q}^T \frac{\partial M(q)}{\partial q}\dot{q} + A(q)^T \dot{\lambda} - \nabla_q V(q) = \tau + Q_{nc} \tag{4.41}$$

For linear nonholonomic constraints, $\dot{\lambda}$ is interpreted as λ, yielding the compact dynamic model:

$$M(q)\ddot{q} + C(q,\dot{q}) + \nabla_q V(q) = B\vec{u} + Q_{nc}(q,\dot{q}) - A(q)^T \lambda \tag{4.42}$$

where:

- $q \in \mathbb{R}^{n_q}$: generalized coordinate vector.

- $M(q) \in \mathbb{R}^{n_q \times n_q}$: mass-inertia matrix.
- $C(q, \dot{q}) \in \mathbb{R}^{n_q}$: Coriolis and centripetal force vector.
- $\nabla_q V(q) \in \mathbb{R}^{n_q}$: gravity vector.
- $B \in \mathbb{R}^{n_q \times 2}$: input matrix.
- $\vec{u} \in \mathbb{R}^2$: control inputs (torques).
- $Q_{nc}(q, \dot{q}) \in \mathbb{R}^{n_q}$: non-conservative forces.
- $A(q) \in \mathbb{R}^{n_r \times n_q}$: Jacobian of nonholonomic constraints.
- $\lambda \in \mathbb{R}^{n_r}$: Lagrange multipliers.

4.4.1 Matrix Component Derivation

The components of $M(q)$ are given by:

$$M_{jk}(q) = \sum_{i=0}^{N} \sum_{\alpha \in \{v,r,l\}} \left[m_{\alpha i} \left(\frac{\partial p_{C\alpha i}}{\partial q_j} \right)^T \left(\frac{\partial p_{C\alpha i}}{\partial q_k} \right) + I_{\alpha i} \left(\frac{\partial \phi_{\alpha i}}{\partial q_j} \right)^T \left(\frac{\partial \phi_{\alpha i}}{\partial q_k} \right) \right] \tag{4.43}$$

where:

- $\alpha \in \{v, r, l\}$: refers to the vehicle body, right wheel, or left wheel.
- $p_{C\alpha i}(q)$: position of component (α, i) of Center of Mass.
- $\phi_{\alpha i}(q)$: orientation angle of component (α, i).

The potential energy contribution from terrain slope effects is computed using:

$$\nabla_q V(q) = \sum_{i=0}^{N} \left[J_{p_i}(q)^T \cdot (-m_i g_i \cdot \vec{s}_i) \right] \tag{4.44}$$

where:

- $J_{p_i}(q)$ is the Jacobian of the CoM of vehicle i.
- $\vec{s}_i = [\tan(\alpha_{xi}), \tan(\alpha_{yi})]$ is the slope vector at vehicle i, computed from inclination angles in the x and y directions.
- m_i and g_i are the mass and local gravity constant of vehicle i.

This expression accounts for the terrain-aware gravitational contribution on each vehicle segment.

4.4.2 Coriolis and Centripetal Force Vector $C(q, \dot{q})$

The Coriolis and centripetal effects in the full dynamic model are captured through the vector $C(q, \dot{q})$, which arises from the time derivative of the kinetic energy matrix $M(q)$. This vector is derived from the Christoffel symbols of the first kind using the following definition:

$$C_i(q, \dot{q}) = \sum_{j=1}^{n_q} \sum_{k=1}^{n_q} \Gamma_{ijk}(q) \dot{q}_j \dot{q}_k \tag{4.45}$$

where the Christoffel symbols Γ_{ijk} are computed as:

$$\Gamma_{ijk}(q) = \frac{1}{2} \left(\frac{\partial M_{ij}}{\partial q_k} + \frac{\partial M_{ik}}{\partial q_j} - \frac{\partial M_{jk}}{\partial q_i} \right) \tag{4.46}$$

In practice, instead of explicitly constructing the full tensor Γ_{ijk}, we directly compute the Coriolis vector as:

$$C(q, \dot{q}) = \sum_{k=1}^{n_q} \left[\sum_{j=1}^{n_q} \left(\sum_{i=1}^{n_q} \Gamma_{ijk}(q) \right) \dot{q}_j \right] \dot{q}_k \tag{4.47}$$

This expression is implemented by iterating over all combinations of indices (i, j, k) for the generalized coordinates, and summing the Christoffel contributions accordingly. The symbolic implementation ensures generality and allows this to be adapted to any number of trailers.

The resulting vector $C(q, \dot{q}) \in \mathbb{R}^{n_q}$ is then used in the full-space dynamics:

$$M(q)\ddot{q} + C(q, \dot{q}) + \nabla_q V(q) = Bu + Q_{nc} - A^T(q)\lambda \tag{4.48}$$

When transforming to reduced coordinates using the null-space matrix $S(q)$, the projected Coriolis vector is:

$$\bar{C}(q, \nu) = S^T(q) \left[C(q, S(q)\nu) + M(q)\dot{S}(q)\nu \right] \tag{4.49}$$

This accounts both for the curvature of the manifold defined by the constraints and the time-varying nature of the null-space basis.

4.4.3 Friction Modeling via LuGre Dynamics

To capture the effect of longitudinal wheel-soil interaction with dynamic friction behavior, a LuGre friction model was implemented across all wheels of the N-Trailer system. This model allows for torque estimation due to friction forces by considering the relative slip velocities at the contact points.

The LuGre model introduces internal state variables z_i to represent the bristle deformation dynamics at the contact interface, resulting in friction forces that exhibit both pre-sliding and sliding regimes. For a system with n bodies (tractor and $n-1$ trailers), a pair of internal states (z_{r_i}, z_{l_i}) is defined per vehicle for the right and left wheels, respectively. These states evolve according to the differential equations:

$$\dot{z}_{r_i} = v_{\text{slip},r_i} - \frac{|v_{\text{slip},r_i}|}{g(v_{\text{slip},r_i})} z_{r_i}, \tag{4.50}$$

$$\dot{z}_{l_i} = v_{\text{slip},l_i} - \frac{|v_{\text{slip},l_i}|}{g(v_{\text{slip},l_i})} z_{l_i}, \tag{4.51}$$

where the function $g(\cdot)$ defines the Stribeck effect:

$$g(v) = F_c + (F_s - F_c) \cdot \exp\left(-\left(\frac{|v|}{v_s}\right)^2\right), \tag{4.52}$$

and F_s, F_c, and v_s represent the static friction, Coulomb friction, and Stribeck velocity, respectively. The resulting friction torques applied at each wheel are computed as:

$$\tau_{r_i} = r_i \left(\sigma_0 z_{r_i} + \sigma_1 \dot{z}_{r_i} + \sigma_2 v_{\text{slip},r_i}\right), \tag{4.53}$$

$$\tau_{l_i} = r_i \left(\sigma_0 z_{l_i} + \sigma_1 \dot{z}_{l_i} + \sigma_2 v_{\text{slip},l_i}\right), \tag{4.54}$$

where r_i is the wheel radius, and σ_0, σ_1, and σ_2 are LuGre model parameters representing stiffness, damping, and viscous friction respectively.

The longitudinal slip velocities v_{slip,r_i} and v_{slip,l_i} are defined based on the forward velocity and rotation rate of each vehicle:

$$v_{\text{long},r_i} = \dot{x}\cos(\theta_i) + \dot{y}\sin(\theta_i) + b_i\dot{\theta}_i, \tag{4.55}$$

$$v_{\text{long},l_i} = \dot{x}\cos(\theta_i) + \dot{y}\sin(\theta_i) - b_i\dot{\theta}_i, \tag{4.56}$$

$$v_{\text{slip},r_i} = v_{\text{long},r_i} - r_i\dot{\psi}_{r_i}, \tag{4.57}$$

$$v_{\text{slip},l_i} = v_{\text{long},l_i} - r_i\dot{\psi}_{l_i}, \tag{4.58}$$

where b_i is the half-track width for vehicle i, and $\dot{\psi}_{r_i}$ and $\dot{\psi}_{l_i}$ are angular rates of the right and left wheels.

The final friction torque vector $\tau_{\text{LuGre}} \in \mathbb{R}^{2n}$ is then appended to the generalized force vector $\vec{f}(q, \dot{q})$, preserving the system's dimensional consistency. The LuGre model thus enables a physically consistent estimation of friction-induced energy losses during locomotion on variable terrains.

4.4.4 Aerodynamic Force Modeling

In order to account for the aerodynamic drag acting on each module of the N-Trailer system, a symbolic model of the drag force was implemented. This force, quadratic in velocity, is projected onto the generalized coordinates using the Jacobians of the vehicle centers of mass.

The aerodynamic drag force acting on each vehicle i is modeled as:

$$\vec{F}_{d_i} = -\frac{1}{2}\rho C_{d_i} A_i \|\vec{v}_i\| \vec{v}_i \tag{4.59}$$

where:

- ρ: air density,
- C_{d_i}: drag coefficient of vehicle i,
- A_i: frontal area of vehicle i,
- $\vec{v}_i$: linear velocity of the center of mass of vehicle i in the global frame.

The velocity vector $\vec{v}_i$ is computed as:

$$\vec{v}_i = J_{p_i}(q)\dot{q} \tag{4.60}$$

where $J_{p_i}(q)$ is the Jacobian of the position of the center of mass of vehicle i with respect to the generalized coordinates. The resulting generalized aerodynamic force is obtained by projecting $\vec{F}_{d_i}$ onto the generalized coordinates as:

$$Q_d = \sum_{i=0}^{N} J_{p_i}^T(q) \cdot \vec{F}_{d_i} \tag{4.61}$$

To ensure numerical stability, a small positive constant ε is added when computing the magnitude:

$$\|\vec{v}_i\| = \sqrt{\vec{v}_i^T \vec{v}_i + \varepsilon^2} \tag{4.62}$$

This aerodynamic model introduces a dissipative force component that varies with the magnitude and direction of the vehicle's velocity. The symbolic implementation ensures analytical differentiability and compatibility with the overall Lagrangian formulation of the GNT dynamics.

4.4.5 Construction of the Constraint Matrix $A(q)$

The nonholonomic constraint matrix $A(q)$ captures the kinematic restrictions that arise from the no-slip condition of each wheel, both in the normal and longitudinal directions. For a system with n vehicle modules (tractor and $n-1$ trailers), each vehicle contributes three constraints:

I. One lateral (normal) constraint due to no lateral slipping of the rigid body.

II. Two longitudinal constraints, one per wheel (right and left), ensuring pure rolling without slippage.

The lateral constraint of each vehicle is formulated using a normal unit vector:

$$\vec{n}_i = \begin{bmatrix} -\sin(\theta_i) \\ \cos(\theta_i) \end{bmatrix} \tag{4.63}$$

and the Jacobian of the position of the center of mass $J_{p_i}(q)$:

$$\vec{n}_i^T J_{p_i}(q)\dot{q} = 0 \tag{4.64}$$

The longitudinal (tangential) constraints for each wheel use:

- The tangential unit vector:

$$\vec{t}_i = \begin{bmatrix} \cos(\theta_i) \\ \sin(\theta_i) \end{bmatrix} \tag{4.65}$$

- The Jacobians of the right and left wheel positions: $J_{pr_i}(q)$ and $J_{pl_i}(q)$,
- The angular velocity of each wheel $\dot{\psi}_{r_i}, \dot{\psi}_{l_i}$ and its associated rolling radius r_i.

Each tangential constraint is expressed as:

$$\vec{t}_i^T J_{pr_i}(q)\dot{q} - r_i\dot{\psi}_{r_i} = 0 \tag{4.66}$$

$$\vec{t}_i^T J_{pl_i}(q)\dot{q} - r_i\dot{\psi}_{l_i} = 0 \tag{4.67}$$

These equations are assembled row-wise into the matrix $A(q)$, with each row representing one constraint. The influence of wheel actuation is encoded via auxiliary vectors δ_r, δ_l with a $-r_i$ coefficient at the index corresponding to the angular velocity of the respective wheel.

The final constraint matrix $A(q) \in \mathbb{R}^{3n \times n_q}$ has the structure:

$$A(q) = \begin{bmatrix} \vec{n}_0^T J_{p_0}(q) \\ \vec{t}_0^T J_{pr_0}(q) - r_0\delta^T_{\psi_{r0}} \\ \vec{t}_0^T J_{pl_0}(q) - r_0\delta^T_{\psi_{l0}} \\ \vdots \\ \vec{n}_{n-1}^T J_{p_{n-1}}(q) \\ \vec{t}_{n-1}^T J_{pr_{n-1}}(q) - r_{n-1}\delta^T_{\psi_{r(n-1)}} \\ \vec{t}_{n-1}^T J_{pl_{n-1}}(q) - r_{n-1}\delta^T_{\psi_{l(n-1)}} \end{bmatrix} \tag{4.68}$$

This construction guarantees that the constraint matrix captures both the kinematic consistency of the trailer alignment and the rolling behavior of each wheel. Optionally, the expression can be symbolically simplified to facilitate later symbolic manipulations or code generation.

4.4.6 Null-Space Projection Matrix

The constraint matrix $A(q)$ introduced in the previous section imposes a set of $m = 3n$ nonholonomic constraints on the full system velocity $\dot{q} \in \mathbb{R}^{n_q}$. Since these constraints are linear in $\dot{q}$ and have full row rank, the system's feasible velocity space lies within the null space of $A(q)$. To reduce the dynamic model accordingly, we define a null-space projection matrix $S(q)$ such that:

$$\dot{q} = S(q)v \tag{4.69}$$

where:

- $S(q) \in \mathbb{R}^{n_q \times n_u}$, with $n_u = n_q - \text{rank}(A)$.
- $v \in \mathbb{R}^{n_u}$ is the reduced velocity vector, usually representing the angular velocities of the actuated wheels.

By construction, $S(q)$ satisfies:

$$A(q)S(q) = 0 \tag{4.70}$$

meaning that the projected motion obeys all nonholonomic constraints. The matrix $S(q)$ is typically computed as a basis of the null space of $A(q)$, either analytically (e.g., via symbolic row reduction or orthogonal projection) or numerically.

To derive the dynamics in reduced coordinates, the second derivative $\ddot{q}$ is required. By differentiating the velocity mapping, we obtain:

$$\ddot{q} = \dot{S}(q)v + S(q)\dot{v} \tag{4.71}$$

The time derivative of $S(q)$, denoted as $\dot{S}(q)$, introduces Coriolis-type terms due to the configuration-dependent structure of the null-space basis. It is computed using the chain rule:

$$\dot{S}(q) = \sum_{j=1}^{n_q} \frac{\partial S(q)}{\partial q_j} \dot{q}_j \tag{4.72}$$

Alternatively, by substituting $\dot{q} = S(q)v$, we obtain:

$$\dot{S}(q) = \sum_{j=1}^{n_q} \frac{\partial S(q)}{\partial q_j} [S(q)v]_j \tag{4.73}$$

This term is essential for computing the reduced Coriolis vector:

$$\bar{C}(v, q) = S^T(q)\left[C(q, \dot{q}) + M(q)\dot{S}(q)v\right] \tag{4.74}$$

and for transforming the full-space dynamics into the reduced dynamics:

$$\bar{M}(q) = S^T(q)M(q)S(q) \tag{4.75}$$

$$\bar{f}(q, v) = S^T(q)f(q, \dot{q}) \tag{4.76}$$

$$\bar{B}(q) = S^T(q)B(q) \tag{4.77}$$

The reduced dynamic model then evolves as:

$$\bar{M}(q)\dot{v} + \bar{C}(q, v) + \bar{f}(q, v) = \bar{B}(q)u \tag{4.78}$$

This null-space formulation ensures that all constraint forces are implicitly eliminated, yielding a minimal and physically consistent model for control and simulation purposes.

4.4.7 Full-State Vector Dynamics

To construct the complete system dynamics for control and simulation purposes, we define the full state vector x as:

$$x = \begin{bmatrix} q \\ \dot{q} \\ z \end{bmatrix} \tag{4.79}$$

where q represents the generalized coordinates, $\dot{q}$ their velocities, and z the internal LuGre friction states if used. The reduced dynamics are formulated in terms of the null-space velocity vector u, which satisfies:

$$\dot{q} = N(q)u \tag{4.80}$$

The full dynamics in the reduced coordinates are derived by projecting the Euler-Lagrange equations onto the null space of the constraint Jacobian:

$$\bar{M}(q)\dot{u} + \bar{C}(q, u) + \bar{G}(q) + \bar{Q}(q, u, z) = \bar{B}(q)u \tag{4.81}$$

where:

$$\begin{aligned} \bar{M}(q) &= N^T M(q)N && \text{(projected inertia)} \\ \bar{C}(q, u) &= N^T[M(q)\dot{N}(q)u + C(q, Nu)] && \text{(projected Coriolis)} \\ \bar{G}(q) &= N^T G(q) && \text{(projected gravity)} \\ \bar{Q}(q, u, z) &= N^T[Q_{aero} + Q_{lugre}] && \text{(projected external forces)} \\ \bar{B}(q) &= N^T B(q) && \text{(projected control input matrix)} \end{aligned}$$

The full-state dynamics are computed as:

$$\dot{q} = N(q)u \tag{4.82}$$

$$\dot{u} = \bar{M}(q)^{-1}\left(\bar{B}(q)U - \bar{C}(q,u) - \bar{G}(q) - \bar{Q}(q,u,z)\right) \tag{4.83}$$

If LuGre friction is used, the internal dynamics of the state vector z are also computed and concatenated, yielding the total system dynamics:

$$\dot{x} = \begin{bmatrix} \dot{q} \\ \dot{u} \\ \dot{z} \end{bmatrix} \tag{4.84}$$

If LuGre dynamics are not used, the state vector reduces to:

$$\dot{x} = \begin{bmatrix} \dot{q} \\ \dot{u} \end{bmatrix} \tag{4.85}$$

This representation is critical for formulating control strategies, as it encapsulates the complete dynamics while respecting the nonholonomic constraints.

5 | Instantaneous Power Consumption

This chapter presents a comprehensive formulation of the instantaneous power consumption (IPC) in Generalized N-Trailer (GNT) systems. Building upon the dynamic model established in the previous chapters, the objective is to quantify, at each instant of motion, the real-time energetic demand associated with the actuation of the tractor's wheels. The proposed framework explicitly incorporates the effects of nonholonomic constraints, terrain-induced loads, and frictional interactions between the wheels and the soil.

The formulation is intended to be general enough to evaluate both *nominal* operating conditions, such as steady forward motion on flat terrain, and *transient* scenarios involving accelerations, directional changes, or traversal of irregular slopes. Furthermore, the derivation also accounts for regenerative events, in which kinetic or potential energy can be partially recovered and stored in the onboard energy source.

5.1 Definition and Scope of Instantaneous Power

The instantaneous mechanical power $P(t)$ associated with an actuator is defined as the inner product between the torque it applies and its corresponding angular velocity:

$$P(t) = \tau(t) \cdot \omega(t) \tag{5.1}$$

where $\tau(t)$ represents the torque applied by the actuator and $\omega(t)$ is the resulting angular velocity of the driven shaft or wheel. Positive values of $P(t)$ indicate that the actuator is delivering power to the system, whereas negative values correspond to energy recovery or regenerative braking.

Within the GNT configuration under study, the only actively driven elements are the right and left wheels of the tractor unit. Therefore, the IPC is computed exclusively from these two actuators. Nevertheless, the torque demand at these wheels depends not only on the tractor's own dynamics but also on the mechanical load transmitted through the trailers, which modifies the traction effort required for the overall motion.

5.2 Nonholonomic Dynamics and Control Space Projection

Due to the rolling-without-slipping condition at each wheel, the GNT system is subject to a set of nonholonomic constraints that restrict the admissible velocities of its generalized coordinates. As a result, the evolution of the state vector $q \in \mathbb{R}^{n_q}$ lies on a lower-dimensional manifold defined by the null space of the constraint Jacobian $A(q)$.

The kinematic relation between generalized velocities $\dot{q}$ and the control inputs $u \in \mathbb{R}^2$—here taken as the angular velocities of the right and left tractor wheels—is:

$$\dot{q} = N(q) \cdot u \tag{5.2}$$

where $N(q) \in \mathbb{R}^{n_q \times 2}$ is the *null space matrix* of $A(q)$. This projection guarantees that any input u produces a feasible system motion that satisfies the nonholonomic constraints at all times.

5.3 Wheel-Based Power Computation

Let τ_{r0} and τ_{l0} be the actuator torques applied to the tractor's right and left wheels, and $\dot{\theta}_{r0}$ and $\dot{\theta}_{l0}$ their respective angular velocities. The instantaneous mechanical power at each wheel is then:

$$P_{r0}(t) = \tau_{r0}(t) \cdot \dot{\theta}_{r0}(t), \qquad P_{l0}(t) = \tau_{l0}(t) \cdot \dot{\theta}_{l0}(t) \tag{5.3}$$

The angular velocities are obtained from the kinematic projection:

$$\dot{\theta}_{r0}(t) = [N(q)u]_r, \qquad \dot{\theta}_{l0}(t) = [N(q)u]_l \tag{5.4}$$

where the subscripts r and l denote the respective positions in the projected velocity vector.

5.4 Total Instantaneous Power of the GNT System

The total instantaneous mechanical power input to the GNT is given by:

$$P_{\text{total}}(t) = \tau_{r0}(t) \cdot \dot{\theta}_{r0}(t) + \tau_{l0}(t) \cdot \dot{\theta}_{l0}(t) \tag{5.5}$$

This can be expressed compactly in matrix form as:

$$P(t) = u^T N^T(q) B^T \tau \tag{5.6}$$

where $\tau \in \mathbb{R}^2$ is the vector of actuator torques, and B is the actuation matrix mapping these torques into the generalized force space.

5.5 Effect of Regenerative Braking

When the torque and angular velocity at a wheel are antiparallel, the instantaneous power becomes negative:

$$P_i(t) = \tau_i(t) \cdot \dot{\theta}_i(t) < 0 \tag{5.7}$$

This condition corresponds to *regenerative braking*, whereby the wheel acts as a generator, converting mechanical energy back into electrical form for storage.

The total recoverable energy over a time interval $[t_0, t_f]$ is:

$$E_{\text{regen}} = -\int_{t_0}^{t_f} \sum_i \min\left(P_i(t), 0\right) dt \tag{5.8}$$

The actual usable fraction depends on drivetrain efficiency, electrical conversion losses, and battery charging characteristics.

5.6 Energy Balance and Component-Level Losses

The mechanical power computed above represents the gross energy flow from the actuators to the system. However, part of this energy is dissipated through various mechanisms:

- **Rolling resistance:** modeled using LuGre friction parameters, capturing both static and dynamic slip effects.
- **Aerodynamic drag:** proportional to the square of the forward velocity, contributing significantly at higher speeds.
- **Gravitational effects:** associated with climbing or descending terrain slopes, altering the effective load on the tractor.

Accordingly, the *useful* power available for net acceleration or load hauling is:

$$P_{\text{useful}}(t) = P(t) - P_{\text{drag}}(t) - P_{\text{roll}}(t) - P_{\text{gravity}}(t) \tag{5.9}$$

Finally, an instantaneous efficiency measure can be defined as:

$$\eta(t) = \frac{P_{\text{useful}}(t)}{P_{\text{input}}(t)} \tag{5.10}$$

where $P_{\text{input}}(t)$ denotes the total power delivered by the actuators. This efficiency metric is a key performance indicator for energy-aware design and mission planning, providing a quantitative basis for comparing configurations and operating strategies.

6 | Results

This chapter presents the main results derived from the implementation of the generalized dynamic model for the Generalized N-Trailer (GNT) system. The focus is placed on the analysis of instantaneous power consumption (IPC), incorporating the influence of rolling resistance (modeled using the LuGre friction model), gravitational slope effects, and aerodynamic drag. Additionally, the model's ability to capture regenerative energy events during braking or downhill motion is assessed. Both symbolic and numerical simulations are employed to evaluate the model's structural validity and its behavior under diverse operational conditions.

6.1 Validation of the Dynamic Model via Symbolic Consistency

As an initial step in evaluating the proposed model, a thorough symbolic validation was conducted to verify the mathematical consistency of its fundamental components. This included the inertia matrix $M(q)$, the Coriolis and centripetal forces $C(q, \dot{q})$, the nonholonomic constraint matrix $A(q)$, the null space projection matrix $N(q)$, and the actuation mapping matrix $B(q)$. Proper formulation of these elements ensures not only the model's ability to represent N-trailer systems accurately but also its applicability in control schemes and symbolic simulation.

First, the symmetry of the inertia matrix $M(q)$ was verified, which is a fundamental property of any Lagrangian-based formulation derived from a scalar kinetic energy expression. In all tested configurations, the matrix $M(q)$ was exactly symmetric with respect to its main diagonal, confirming the physical soundness of the energy formulation.

Second, the orthogonality between the constraint matrix $A(q)$ and the null space matrix $N(q)$ was evaluated. Specifically, the condition:

$$A(q)N(q) = 0$$

must be satisfied to ensure that the motion projected through the reduced control space (defined by u) complies with the system's nonholonomic constraints. In all simulations, the symbolic multiplication of $A(q)$ and $N(q)$ yielded a null matrix with numerical errors below symbolic tolerance ($< 10^{-12}$), validating the correct construction of $N(q)$ as the null space of $A(q)$.

Furthermore, a cross-validation was performed between the analytical derivatives of the kinetic energy $T(q, \dot{q})$ and the entries of the inertia matrix $M(q)$. Using the expression:

$$M(q) = \frac{\partial^2 T(q, \dot{q})}{\partial \dot{q}^2}$$

it was confirmed that the symbolic elements of $M(q)$ matched exactly with the second-order derivatives of T, validating that $M(q)$ was correctly assembled from a coherent energy-based formulation. This verification reinforces the reliability of the dynamic model for power estimation and behavioral analysis.

Finally, the validity of the projection operator defined as $N(q)N(q)^T$ was tested. This operator maps reduced-space velocity vectors u into full generalized coordinate velocity vectors $\dot{q}$, ensuring they comply with the nonholonomic constraints. It was verified that this projection accurately reconstructs physically admissible trajectories and that kinetic energy and projected forces remain consistent with the original dynamic equations.

Together, these analyses confirm that the proposed dynamic model rigorously satisfies the physical and structural principles required to represent a GNT system in realistic operational scenarios. These foundations support the energetic simulations and evaluations of regeneration and efficiency presented in the subsequent sections.

6.2 Case Study: Straight-Line Trajectory on Flat Terrain

This section analyzes the behavior of the *Generalized N-Trailer* (GNT) system under a simplified and controlled scenario: motion along a straight path over flat terrain, with no wind or slope. The objective is to isolate intrinsic dynamic effects related to actuation and friction, and to evaluate their impact on the resulting instantaneous power consumption (IPC).

The simulation setup applies constant torques to both tractor wheels, producing forward motion of the entire GNT structure. Under these conditions, the wheel angular velocities increase during the transient phase and converge to nearly constant values once the system reaches steady-state motion. The null-space projection, derived from the nonholonomic constraints, is used to compute the full generalized velocity vector $\dot{q}(t)$. From $\dot{q}(t)$, the IPC is evaluated based on actuator torques and wheel angular velocities.

6.2.1 Physical Parameters Used in Simulation

Table 6.1 summarizes the physical parameters of the tractor and trailers employed in the simulations.

Table 6.1: Physical parameters used in the straight-line motion simulations.

Element	a **[m]**	b **[m]**	L **[m]**	L_h **[m]**	m **[kg]**	I **[kg·m^2]**	r **[m]**	m_w **[kg]**	I_w **[kg·m^2]**
Tractor	0.05	0.24	0.00	0.00	16	0.537	0.095	0.50	0.0023
Trailer 1	0.05	0.24	0.25	0.20	16	0.537	0.095	0.50	0.0023
Trailer 2	0.05	0.24	0.25	0.20	16	0.537	0.095	0.50	0.0023
Trailer 3	0.05	0.24	0.25	0.20	16	0.537	0.095	0.50	0.0023

6.2.2 Angular Velocity and Torque Profiles

Figure 6.1 summarizes the main kinematic and dynamic variables obtained from the straight-line motion simulations of the *Generalized N-Trailer* (GNT) system. In all cases, constant torque inputs are applied to both tractor wheels, leading to a transient increase in wheel angular velocity that stabilizes once the system reaches steady-state motion. As expected, the right and left wheel angular velocity profiles are nearly identical, confirming the absence of yaw rate or turning maneuvers. The corresponding actuator torques, $\tau_{r0}(t)$ and $\tau_{l0}(t)$, remain constant throughout the maneuver due to the lack of accelerations or external disturbances.

Figure 6.1 presents the complete simulation results for three different configurations: G1T, G2T, and G3T. For each configuration:

- **a), c), e):** Torque profile, angular velocity of the tractor wheels, angular velocity of the vehicle bodies, and longitudinal velocity of the tractor.
- **b), d), f):** Straight-line displacement of the GNT system.

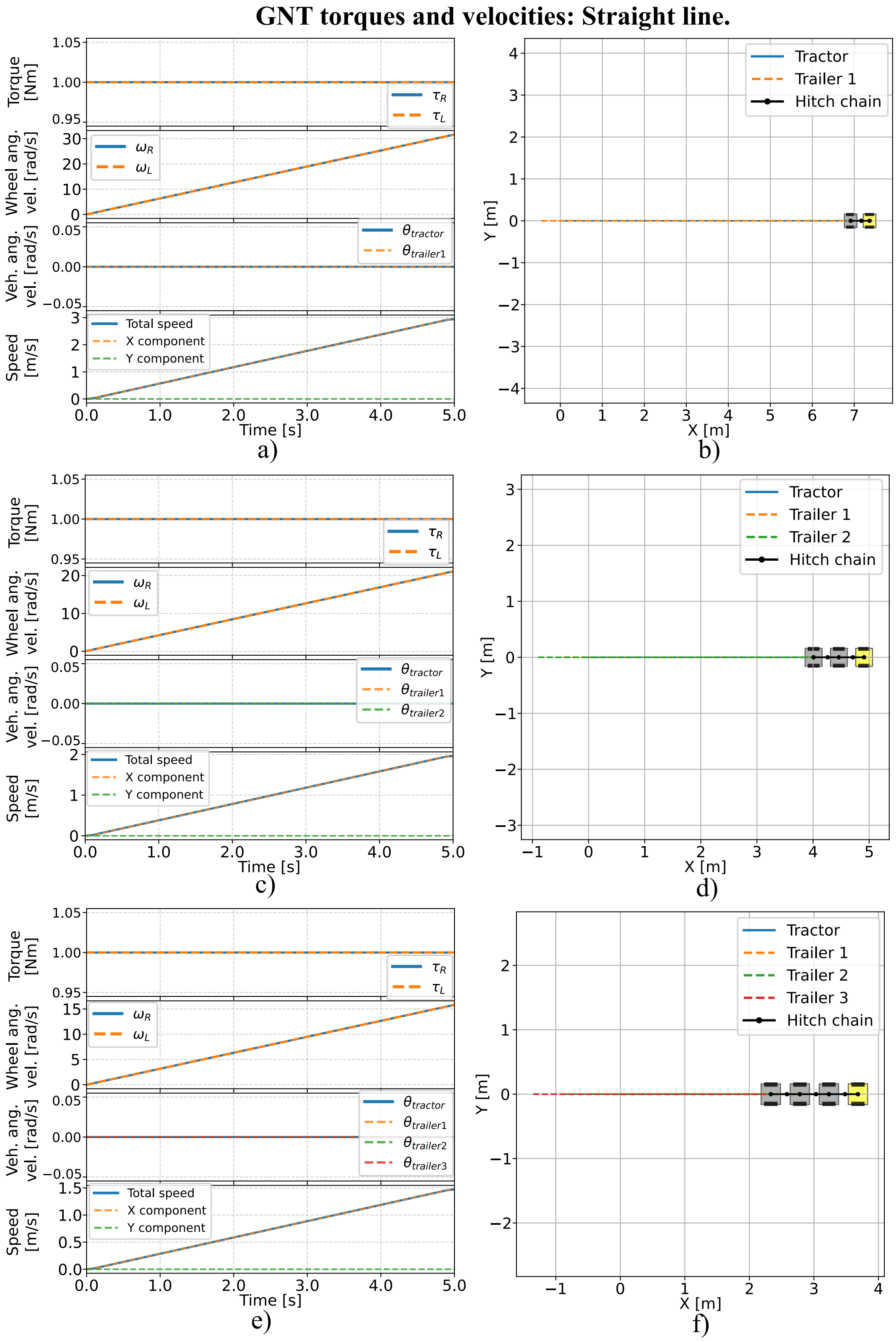

Figure 6.1: Simulation results for straight-line motion: G1T (a,b), G2T (c,d), and G3T (e,f).

6.2.3 Instantaneous Power Consumption

The instantaneous power consumption for each wheel is computed as:

$$P_i(t) = \tau_i(t) \cdot \dot{\theta}_i(t), \tag{6.1}$$

where $\tau_i(t)$ is the torque applied to the i-th wheel, and $\dot{\theta}_i(t)$ is its angular velocity. Figure 6.2 presents the results for three different GNT configurations — G1T, G2T, and G3T — during a straight-line maneuver under constant torque inputs.

Subfigure (a) corresponds to the G1T configuration. With a single trailer, the applied torque results in the highest wheel angular velocities among the three cases, producing the largest instantaneous power consumption. The profiles for the right and left wheels are practically identical due to the symmetric torque input, confirming balanced load distribution. Once steady-state is reached, the relationship between torque and power becomes nearly linear.

Subfigure (b) presents the G2T configuration. Adding a second trailer increases the total mass and rotational inertias of the system, which restricts the achievable wheel angular velocity for the same torque input. As a consequence, the instantaneous power consumption is lower than in the G1T case. This reduction in wheel speed also implies a smaller linear displacement over the same simulation horizon.

Subfigure (c) shows the G3T configuration. With three trailers, the effect of additional mass and inertia is even more pronounced, further limiting wheel angular velocity and thus reducing instantaneous power consumption. Although the mechanical power demand is lowest in this case, the vehicle covers the shortest distance for the same input torque profile, reflecting the greater inertial resistance of longer GNT structures.

Across all configurations, the nearly identical power profiles for the left and right wheels highlight the symmetrical nature of the load distribution in straight-line motion. Moreover, the observed trend confirms that, for a fixed constant torque input, increasing the number of trailers decreases instantaneous mechanical power output due to reduced wheel rotational speed, even though the torque remains unchanged.

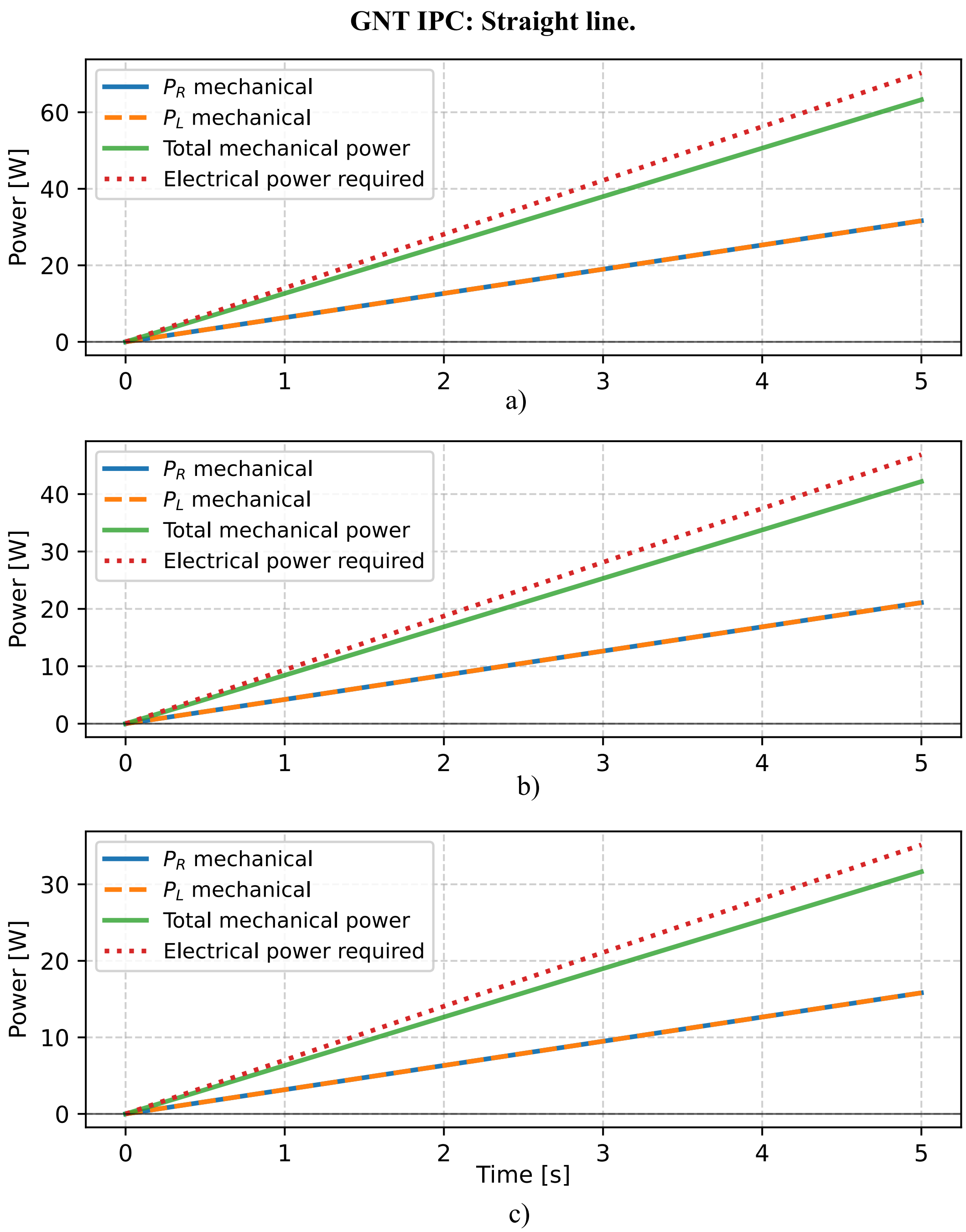

Figure 6.2: Instantaneous power consumption during straight-line motion under constant torque input: (a) G1T configuration, (b) G2T configuration, (c) G3T configuration.

6.2.4 Frictional Contribution from the LuGre Model

The LuGre friction parameters used in this study are summarized in Table 6.2. For the straight–line test, a constant driving torque of 0.1 Nm was applied for a duration of 25 s.

Table 6.2: LuGre friction parameters used in the simulations.

Parameter	Symbol	Value
Stiffness coefficient	σ_0	6
Damping coefficient	σ_1	3.5
Viscous friction coefficient	σ_2	6
Coulomb friction force	F_c	64
Static friction force	F_s	72
Stribeck velocity	v_s	0.1

Figure 6.3 illustrates the torque contribution from the LuGre model for two scenarios. In Subfigure (a), the trajectories with LuGre friction and pure rolling are compared side-by-side. Both configurations exhibit nearly identical displacements under these conditions. This occurs because the current LuGre implementation accounts only for the *longitudinal slip* component of wheel–ground interaction. In pure straight–line motion, longitudinal slip remains minimal, and the absence of lateral slip modeling results in negligible differences between LuGre and pure rolling. Extending the LuGre formulation to incorporate *lateral slip* could provide a more comprehensive frictional model. Such an extension would require augmenting the state vector to include lateral velocity, enabling the model to capture slip–induced resistive forces even in pure rolling conditions.

In Subfigure (b), a different experiment is shown for a G3T configuration, where a differential torque of 0.1 Nm on the right wheel and 0.11 Nm on the left wheel is applied. Here, the presence of LuGre friction produces a measurable deviation in the trajectory and a reduction in the total displacement compared to pure rolling, highlighting its influence in scenarios with induced slip.

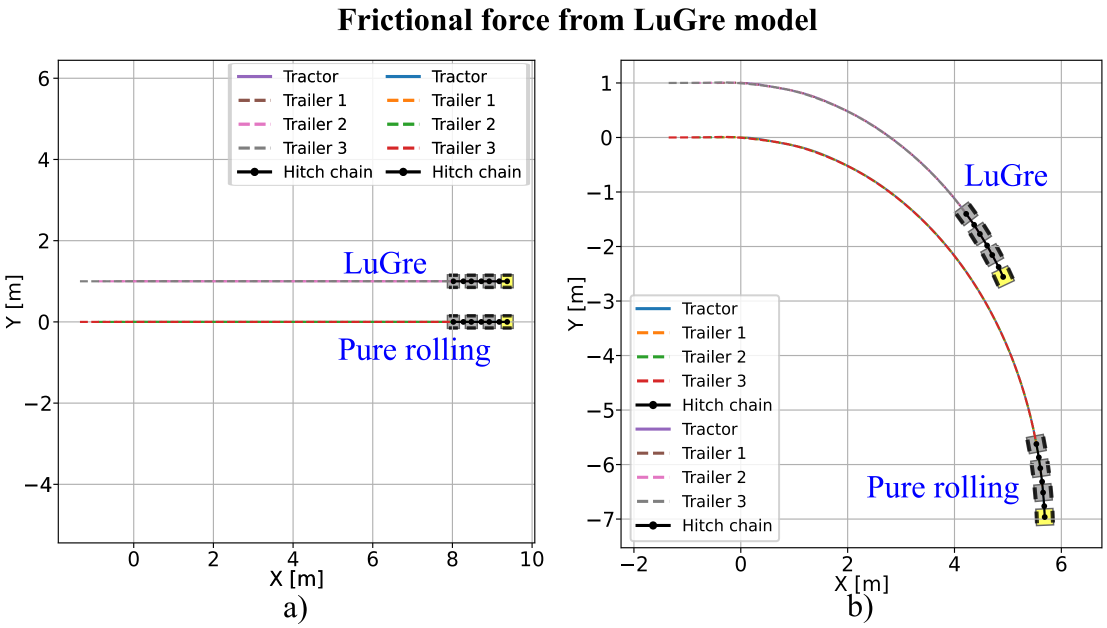

Figure 6.3: Friction torque contribution from the LuGre model: (a) straight-line displacement comparison with LuGre and pure rolling, (b) deviation and displacement reduction for differential torque input in a G3T.

6.2.5 Absence of Regenerative Events

Since the trajectory is executed at constant velocity with no braking or slope-induced deceleration, no regenerative power events occur in this simulation. All instantaneous power values remain strictly positive, indicating that the actuators solely provide energy without recovery.

6.2.6 Summary

This case study validates the energetic symmetry and predictability of the GNT system in ideal conditions. The results serve as a baseline for comparing more complex maneuvers, where slope, terrain variability, or dynamic braking may alter the power profiles and trigger regenerative effects.

6.3 Analysis on Sloped Terrain and Energy Regeneration

In this section, we examine the dynamic and energetic behavior of the GNT system when traversing inclined terrains, both uphill and downhill. The terrain slope is encoded using the slope vector $\vec{s}_i = [s_{xi}, s_{yi}]$ for each vehicle segment, and its impact on the generalized gravitational force $\nabla_q V(q)$ is evaluated. The simulation setup incorporates varying slope magnitudes to assess how terrain inclination affects power consumption and regenerative capabilities.

6.3.1 Impact of Terrain Gradient on Power Flow

Figure 6.4 illustrates the gravitational contribution $\nabla_q V(q)$ induced by the slope vector $\vec{s}_i$ for different generalized N-trailer configurations. The results reveal that uphill motion increases the gravitational load, thereby requiring a higher input torque to maintain motion, whereas downhill motion results in a gravitational component that reduces the net actuator effort.

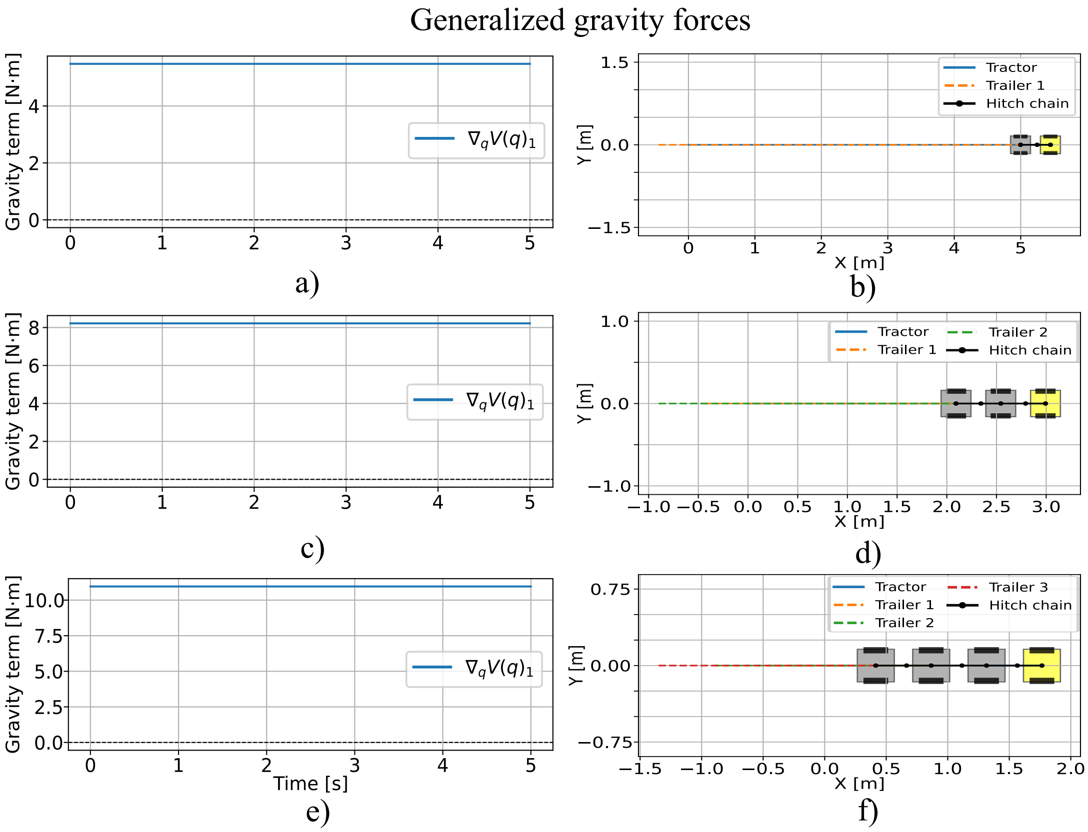

Figure 6.4: Generalized gravitational forces $\nabla_q V(q)$ for ascending slopes.

In subfigures (a) and (b), the results correspond to the G1T configuration, while subfigures (c) and (d) correspond to G2T, and subfigures (e) and (f) to G3T. In each case, the left subfigure (a, c, e) shows the contribution of each subcomponent —the tractor and each trailer individually— to the total gravitational generalized force when subjected to a constant slope of tan(1°). These curves clearly indicate how each mass contributes to the total gravitational resistance opposing motion along the x direction.

For these experiments, a constant driving torque of 1 Nm was applied to both wheels of the tractor. Under uphill conditions, the gravitational resistance increases with the number of trailers, and in some cases, this gravitational force can exceed the traction force generated by the motors, causing the vehicle to lose forward velocity and eventually move backwards along the slope. Conversely, when the slope is negative (downhill), the gravitational term acts in the same direction as the desired motion, effectively assisting the vehicle. In this case, the gravitational component has the same magnitude but opposite sign, which results in a noticeable increase in displacement compared to motion on flat terrain.

This contrast is evident in the right subfigures (b, d, f), which depict the resulting longitudinal displacement for each configuration. As the number of trailers increases, the reduction in uphill displacement becomes more pronounced, while the downhill cases exhibit enhanced displacement due to the assistance provided by gravity.

6.3.2 Regenerative Braking Events

To evaluate the regenerative braking capability of the *Generalized N-Trailer* system, a test was conducted using the G2T configuration. The maneuver consisted of a controlled deceleration at a constant rate of $-2\ \mathrm{m/s^2}$ while descending a slope. Over the course of the braking phase, the vehicle traveled approximately 9.5 m before coming to a stop.

The G2T configuration considered in this test comprised a tractor and two trailers, each weighing approximately 16 kg, resulting in a total vehicle mass dominated by the payload distribution across the three segments. The wheel–ground interaction was modeled using a LuGre friction formulation, which in this case exhibited low adhesion characteristics under straight-line motion conditions. Such reduced adhesion has a direct influence on the achievable regenerative torque, potentially limiting the energy recovery rate.

Figure 6.5 illustrates the instantaneous power consumption profiles during the downhill braking maneuver. Negative power values, which appear when the actuator torque and wheel angular velocity become antiparallel, correspond to periods where regenerative braking is active. The magnitude of these negative values indicates the mechanical power available for conversion back to electrical energy.

Considering a drivetrain regenerative efficiency of $\eta_{\mathrm{regen}} = 30\%$, only a fraction of the mechanical energy captured during braking is converted into usable electrical energy for battery recharging. The remainder is dissipated as heat in the motor and power electronics due to conversion losses. This efficiency constraint, combined with the low-adhesion contact conditions modeled by LuGre, defines the practical limit of energy recovery in this scenario.

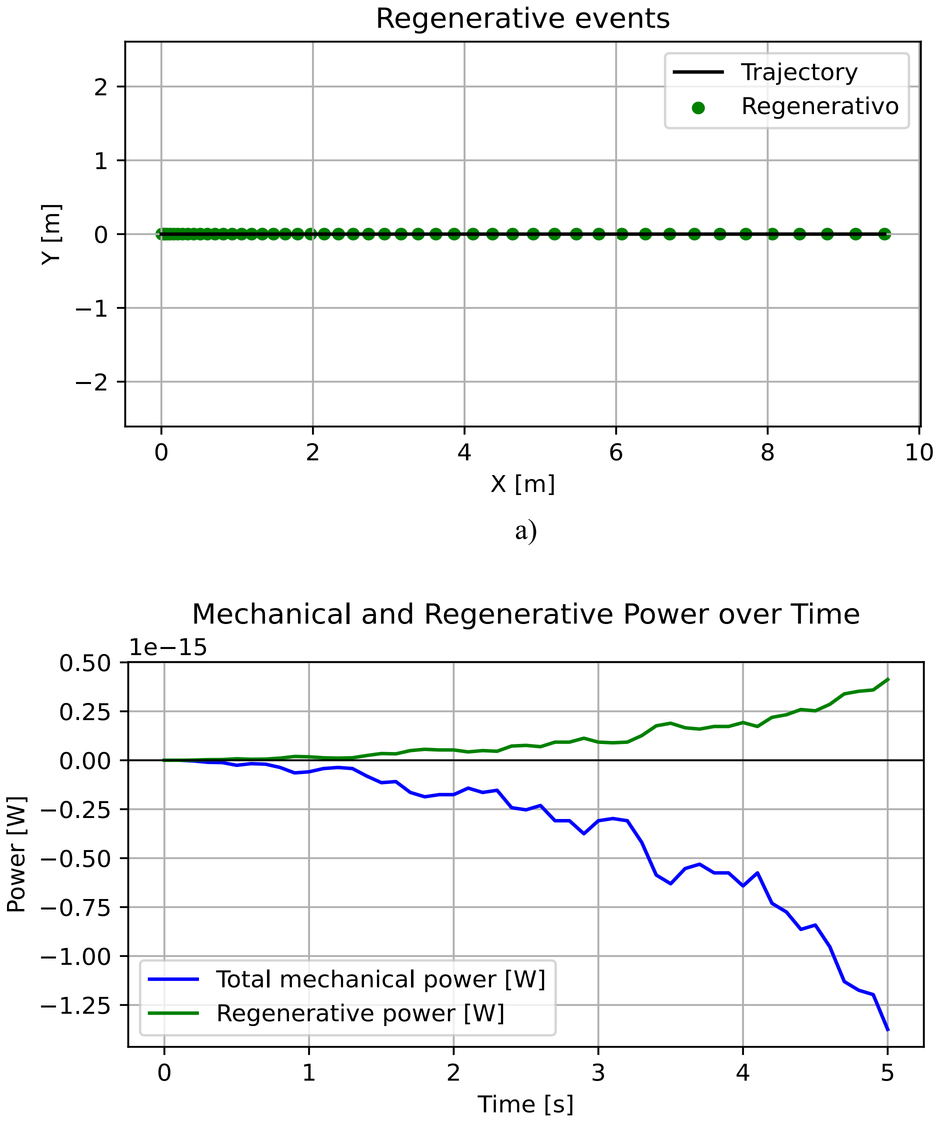

a)

b)

Figure 6.5: Instantaneous power consumption during a downhill regenerative braking event in the G2T configuration with a constant deceleration of $-2\ \mathrm{m/s^2}$. Negative power values indicate periods of active regeneration, with $\eta_{\text{regen}} = 30\%$ and low LuGre adhesion in straight-line motion.

6.3.3 Summary

These results confirm that terrain slope plays a critical role in the energy dynamics of GNT systems. Downhill segments naturally favor energy recovery through regenerative braking, while uphill trajectories demand higher energy input. The proposed model accurately captures these phenomena, providing a reliable framework for energy-aware control design.

6.4 Impact of Aerodynamic Resistance

Aerodynamic resistance constitutes one of the principal contributors to parasitic power losses in wheeled vehicles, particularly as operational speed increases. Even in compact articulated systems designed for off-road agricultural or industrial applications, such as the generalized two-trailer configuration (G2T) considered in this study, the aerodynamic component cannot be neglected in comprehensive energy consumption assessments. This section focuses exclusively on quantifying the magnitude and influence of aerodynamic drag on the instantaneous power demand, providing a comparative perspective between the total actuator power and the net useful mechanical power available for traction.

6.4.1 Aerodynamic Parameters and Assumptions

For the purpose of the present analysis, the aerodynamic characteristics of the G2T were defined according to representative values for low-profile, compact off-road machinery. These parameters are summarized as follows:

- Air density: $\rho = 1\,\mathrm{kg/m^3}$
- Drag coefficient: $C_d = 1.0$ for both the tractor and each trailer
- Effective frontal area: $A = 0.5\,\mathrm{m^2}$

The selected drag coefficient reflects a conservative assumption that accounts for the non-streamlined geometry of agricultural machinery, which typically exhibits significant protrusions and accessories increasing the effective bluffness. The chosen frontal area is consistent with the geometric profile of small-scale tractor–trailer units operating in off-road conditions, while the air density corresponds to standard atmospheric conditions at sea level.

6.4.2 Simulation Protocol

The simulation was conducted over a period of 5 seconds, during which the G2T was subjected to a velocity profile that increased monotonically from rest. This acceleration phase was designed to emulate a realistic scenario where the vehicle transitions from a standstill to moderate operating speed in a controlled yet continuous manner.

Under these conditions, the aerodynamic load increased in a nonlinear fashion, consistent with its well-known dependence on the square of the vehicle's forward velocity. Initially negligible during the first moments of acceleration, the aerodynamic drag became progressively more significant as the speed rose. By the end of the simulation, the resistive force attributable solely to aerodynamic drag reached approximately 2.8 N.

Although this value remains relatively small in absolute terms compared to other resistive forces such as rolling resistance or grade-induced gravitational loads, its contribution to total energy losses cannot be overlooked in sustained operation or during prolonged acceleration phases. In practice, the cumulative effect of aerodynamic drag over extended distances or at higher velocities can translate into a measurable reduction in overall energy efficiency.

6.4.3 Implications for Instantaneous Power Demand

The influence of aerodynamic resistance manifests directly in the instantaneous power profile of the vehicle. As velocity increases, the mechanical power required to overcome aerodynamic drag grows disproportionately, becoming a cubic function of speed when expressed in terms of resistive power demand. This characteristic makes aerodynamic drag relatively minor at low speeds but increasingly dominant at higher ones.

Figure 6.6 presents the comparative evolution of the total actuator power and the net useful power delivered to the ground once aerodynamic losses are subtracted. The shaded region between the curves represents the instantaneous power dissipated exclusively by aerodynamic resistance. In the early stages of acceleration, this shaded region is barely perceptible; however, it becomes progressively more pronounced toward the latter part of the simulation.

From an operational standpoint, these results highlight that even for moderate-speed off-road applications, aerodynamic considerations should be incorporated into energy modeling, particularly when optimizing propulsion strategies for efficiency. In long-duration tasks or when operating at elevated cruising speeds, aerodynamic drag may constitute a significant proportion of the total parasitic losses, influencing both battery autonomy in electric platforms and fuel consumption in conventional engines.

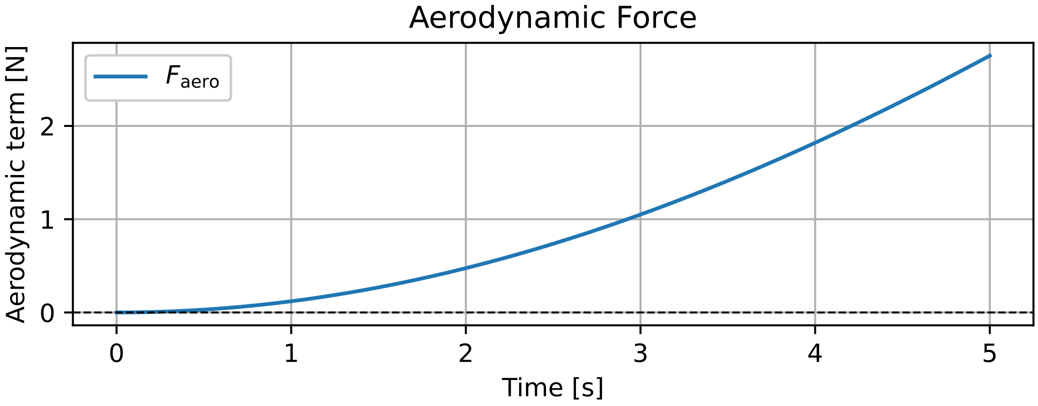

Figure 6.6: Comparison between total power input and useful power output for the G2T configuration, highlighting resistive losses attributable exclusively to aerodynamic drag.

6.4.4 Summary

The results of this study reveal that the energy dynamics of Generalized N-Trailer (GNT) systems are intrinsically governed by the interplay between mechanical configuration and resistive phenomena. Variations in the number of trailers N significantly influence the system's instantaneous power profile, altering the structure of the input-to-motion mapping through the configuration-dependent matrix $N(q)$. These structural changes not only modify the propulsion power required for a given trajectory but also affect the system's capability to exploit regenerative braking during deceleration phases, with higher N configurations offering increased opportunities for energy recovery.

Furthermore, the analysis confirms the dual nature of energy losses in GNT systems. At low velocities, parasitic losses are predominantly governed by rolling resistance, here modeled via the LuGre friction framework, which captures the complex velocity-dependent and pre-sliding behaviors of wheel–ground interactions. In contrast, as operating speeds increase, aerodynamic drag emerges as the dominant dissipative mechanism, with its cubic dependency on velocity leading to rapidly escalating power demands. This transition in loss dominance underscores the importance of speed-dependent optimization in both design and control.

To address this complexity, an instantaneous efficiency metric was introduced, enabling a direct quantification of the proportion of actuator power effectively converted into useful mechanical work. This metric provides a powerful diagnostic tool for real-time, energy-aware decision-making in control strategies, facilitating adaptive modulation of speed, torque distribution, and regenerative braking thresholds to minimize unnecessary energy dissipation.

Overall, the findings highlight that energy efficiency in multi-trailer systems cannot be addressed solely through improved control algorithms or hardware enhancements in isolation. Instead, a holistic design perspective is required—one that simultaneously considers the mechanical configuration, the prevailing resistive regimes across operational speeds, and the control policy—thereby enabling the realization of truly energy-optimized multi-trailer platforms.

6.5 Discussion on Modeling Assumptions and Future Extensions

This section provides a critical reflection on the modeling assumptions adopted in the development of the Generalized N-Trailer (GNT) dynamic framework, highlighting current limitations and proposing directions for future extensions. These considerations aim to enhance the realism, generality, and applicability of the presented model.

6.5.1 Limitations of the Current Model

Despite the broad scope of the symbolic dynamic formulation, several simplifying assumptions were adopted to enable tractability:

- **No soil deformation modeling:** The interaction between wheels and soft terrain is modeled through frictional forces and gravitational slope projections, but without accounting for subsurface deformation, sinkage, or shear displacement in the soil.

- **Absence of lateral slip:** The no-slip nonholonomic constraints impose strict tangential rolling, ignoring lateral tire slip or complex tire dynamics. While this is consistent with classical robotic modeling, it limits realism at high curvature or rapid maneuvering.
- **Simplified actuator model:** The electric motor and drivetrain system is modeled as ideal torque sources. Internal inefficiencies, delay dynamics, and actuator saturation are omitted.
- **No thermal coupling:** Temperature-dependent effects (e.g., in motor efficiency or frictional coefficients) are not considered.

While these assumptions support the symbolic derivation and enable consistent control-oriented formulations, they may underestimate energy losses and dynamic behaviors in field deployments.

6.5.2 Robustness of the Symbolic Framework

One of the key strengths of the presented model lies in its symbolic architecture. The use of symbolic tools (e.g., SymPy) enables:

- **Parameter variability:** System parameters (e.g., masses, inertias, lengths) can be varied without re-deriving the model. This allows extensive parametric studies and system tuning.
- **Automatic simplification:** Redundant expressions and zero elements can be simplified analytically, reducing computational cost for numerical evaluation.
- **Analytical validation:** Structural properties (e.g., symmetry of $M(q)$, orthogonality of $A(q)$ and $N(q)$) can be verified symbolically for correctness.

These properties make the model scalable, maintainable, and easily extensible to other articulated robotic systems beyond the GNT configuration.

6.5.3 Future Extensions

Several directions for model enhancement are envisioned:

- **Powertrain efficiency modeling:** Integrating electric motor efficiency maps, inverter losses, and battery internal resistance would enable more accurate estimation of electrical energy consumption.
- **Thermal modeling:** Coupling frictional and electrical losses with thermal models would allow for temperature-aware control and fault prevention in long-duration tasks.
- **Soil interaction:** Introducing soil mechanics models (e.g., Bekker theory or terramechanics-based resistive forces) could improve off-road traction prediction and motion planning.

- **Experimental validation:** Acquiring real-world data from robotic platforms or scaled prototypes would provide benchmarks to refine model assumptions and validate the energy predictions.
- **3D extensions:** Incorporating roll and pitch dynamics would generalize the current planar model to uneven terrains and hilly conditions.

In summary, while the current model provides a solid foundation for energetically-aware control and analysis, future research should aim at bridging the gap between symbolic dynamics and full-scale experimental realism.

7 | Conclusion and Future Work

7.1 Main Conclusions

This thesis has presented a comprehensive and physically consistent framework for the dynamic modeling and energetic evaluation of Generalized N-Trailer (GNT) systems operating in off-road environments. By integrating symbolic multibody dynamics with terrain- and friction-aware extensions, the work advances both the theoretical understanding and the practical applicability of articulated vehicle modeling.

The proposed dynamic formulation, derived symbolically, captures the coupled behavior of the tractor–trailer ensemble under nonholonomic constraints, variable terrain slopes, and complex wheel–ground interactions. Rolling resistance is modeled through LuGre friction laws, gravitational contributions are explicitly related to terrain inclination, and aerodynamic drag is considered as a speed-dependent dissipative effect.

The instantaneous power consumption (IPC) model developed in this work offers a consistent means to quantify, at the actuator level, both energy expenditure and regenerative potential. Simulation studies show that the approach can detect energy-saving operational patterns, evaluate component-level power losses, and distinguish between regimes dominated by frictional resistance versus those where regenerative braking is possible.

The incorporation of regenerative braking into the IPC formulation enables the detection and quantification of energy recovery events, highlighting their dependence on both terrain gradient and deceleration profiles. Results indicate that, for constant-velocity motion, frictional dissipation dominates, whereas in descending or decelerating conditions, regenerative power contributions become significant.

Finally, the use of symbolic computation allows for the automatic derivation of Jacobians, null-space projections, and constraint-consistent dynamics. This not only streamlines the integration of the model into model predictive control (MPC) schemes but also facilitates rapid adaptation to different vehicle configurations and operating conditions. The outcome is a unified platform for simulation, control design, and energetic assessment of articulated robotic vehicles.

7.2 Research Contributions

This work advances the state of the art in energy modeling and control of articulated off-road robotic systems through the following key contributions:

- **Symbolic Dynamic Modeling of GNT Systems:** A general symbolic formulation for the dynamics of multi-trailer configurations was derived, enabling accurate enforcement of nonholonomic constraints and precise modeling of mechanical couplings.
- **Energetic Formulation under Constraints:** A new IPC formulation was proposed that respects the constraint manifold of the system and decomposes instantaneous power into actuator-driven, frictional, gravitational, and aerodynamic components.
- **Friction- and Terrain-Aware Modeling:** Integration of LuGre-based rolling resistance and slope-dependent gravitational vectors increases the fidelity of off-road energetic predictions.
- **Regenerative Braking Analysis:** Analytical conditions for energy recovery were established and validated in simulation, offering quantitative insight into the regenerative potential across operational profiles.
- **Simulation-Based Energy Assessment:** The framework supports detailed evaluation of energy consumption and recovery in multiple terrain and maneuver scenarios, enabling scenario-specific optimization strategies.

7.3 Future Work

Based on the results obtained, several promising directions for future research are identified:

- **Soil–Vehicle Interaction Modeling:** Incorporating deformable terrain models, such as Bekker–Wong or terramechanics-based formulations, will allow improved prediction of traction forces and energy consumption under soft soil conditions.
- **Real-Time Control Integration:** Embedding the symbolic dynamic model into real-time MPC or NMPC controllers, potentially with hardware-in-the-loop validation, will enable closed-loop energy optimization.
- **Data-Driven Parameter Estimation:** Leveraging machine learning techniques to infer terrain type, friction coefficients, and actuator efficiency from onboard sensory data could enhance adaptability to unknown or changing environments.
- **Comprehensive Powertrain Modeling:** Extending the IPC framework to include motor efficiency maps, inverter losses, and battery models will enable full closed-loop energy flow analysis.
- **Experimental Validation:** Field trials on physical robotic platforms will be essential to validate the modeling assumptions and quantify discrepancies between simulation and reality across different terrains and loading conditions.

- **Sustainability and Deployment Analysis:** Evaluating the environmental, operational, and economic implications of GNT-based autonomous systems in agriculture, forestry, and mining will strengthen the case for adoption.

In summary, this research provides a foundational contribution to the dynamic and energetic modeling of constrained, articulated robotic systems in challenging off-road scenarios. The methodologies and insights developed herein are expected to guide both theoretical advancements and the deployment of energy-aware autonomous platforms, contributing to the design of more efficient, robust, and sustainable off-road robotic operations.

References

[1] M. M. Michalek, "Cascade-like modular tracking controller for non-standard n-trailers," *IEEE Transactions on Control Systems Technology*, vol. 25, no. 2, pp. 619–627, 2017. (document), 2.5.1.2, 2.5.5.4, 2.20, 2.21, 2.3

[2] M. Kovačić, M. Mutavdžija, and K. Buntak, "New paradigm of sustainable urban mobility: Electric and autonomous vehicles—a review and bibliometric analysis," *Sustainability*, vol. 14, no. 15, p. 9525, 2022. 1.1

[3] J. A. Manzolli, J. P. Trovao, and C. H. Antunes, "A review of electric bus vehicles research topics–methods and trends," *Renewable and Sustainable Energy Reviews*, vol. 159, p. 112211, 2022. 1.1

[4] N. Deniz, F. Jorquera, M. Torres-Torriti, and F. A. Cheein, "Model predictive path-following controller for generalised n-trailer vehicles with noisy sensors and disturbances," *Control Engineering Practice*, vol. 142, p. 105747, 2024. 1.1, 2.2.1, 2.5.5

[5] G. Rigatos, K. Busawon, and M. Abbaszadeh, "A nonlinear optimal control approach for the truck and n-trailer robotic system," *IFAC Journal of Systems and Control*, vol. 20, p. 100191, 2022. 1.1

[6] M. Lukassek, J. Dahlmann, A. Völz, and K. Graichen, "Model predictive path-following control for truck–trailer systems with specific guidance points—design and experimental validation," *Mechatronics*, vol. 100, p. 103190, 2024. 1.1, 2.1.1

[7] F. Jorquera, J. Estrada, and F. Auat, "Remote Instantaneous Power Consumption Estimation of Electric Vehicles from Satellite Information," *Robotics*, vol. 12, no. 6, 2023. Type: Article. 1.1, 2.3.2, 2.5.6

[8] J. Leng, J. Peng, J. Liu, Y. Zhang, J. Ji, and Y. Zhang, "Profiling Power Consumption in Low-Speed Autonomous Guided Vehicles," *IEEE Robotics and Automation Letters*, vol. 9, no. 7, pp. 6027 – 6034, 2024. Type: Article. 1.1

[9] J. Zhang, Z. Wang, P. Liu, and Z. Zhang, "Energy consumption analysis and prediction of electric vehicles based on real-world driving data," *Applied Energy*, vol. 275, p. 115408, 2020. 1.1

[10] I. Miri, A. Fotouhi, and N. Ewin, “Electric vehicle energy consumption modelling and estimation—a case study,” *International Journal of Energy Research*, vol. 45, no. 1, pp. 501–520, 2021. 1.1, 2.3.4

[11] Y. Iwashita, K. Nakashima, J. Gatto, S. Higa, A. Stoica, N. Khoo, and R. Kurazume, “Virtual ir sensing for planetary rovers: Improved terrain classification and thermal inertia estimation,” vol. 5, no. 4, pp. 6302–6309, 2020. 1.1

[12] K.-M. Choo and C.-Y. Won, “Design and analysis of electrical braking torque limit trajectory for regenerative braking in electric vehicles with pmsm drive systems,” vol. 35, no. 12, pp. 13308–13321, 2020. 1.1

[13] Y. Yang, Q. He, Y. Chen, and C. Fu, “Efficiency optimization and control strategy of regenerative braking system with dual motor,” vol. 13, no. 3, 2020. 1.1

[14] A. T. Hamada and M. F. Orhan, “An overview of regenerative braking systems,” *Journal of Energy Storage*, vol. 52, p. 105033, 2022. 1.1

[15] L. Hou, F. Zhou, K. Kim, and L. Zhang, “Practical model for energy consumption analysis of omnidirectional mobile robot,” vol. 21, no. 5, pp. 1–18, 2021. 1.1

[16] O. Lamarre, O. Limoyo, F. Marić, and J. Kelly, “The canadian planetary emulation terrain energy-aware rover navigation dataset,” vol. 39, no. 6, pp. 641–650, 2020. 1.1

[17] M. Mikschi, *Identification of the driving dynamics of a skid-steered mobile robot based on geodetic measurements*. PhD thesis, Wien, 2023. 1.1

[18] J. Villacrés and F. Auat Cheein, “In-field piecewise regression based prognosis of the IPC in electrically powered agricultural machinery,” *Computers and Electronics in Agriculture*, vol. 202, 2022. Type: Article. 1.1, 2.3.2

[19] S. Pokharel, P. Sah, and D. Ganta, “Improved prediction of total energy consumption and feature analysis in electric vehicles using machine learning and shapley additive explanations method,” *World Electric Vehicle Journal*, vol. 12, no. 3, p. 94, 2021. 1.1

[20] J. Villacrés and F. A. Cheein, “In-field piecewise regression based prognosis of the ipc in electrically powered agricultural machinery,” *Computers and Electronics in Agriculture*, vol. 202, p. 107324, 2022. 1.1, 2.5.7, 2.5.7, 2.5.8, 2.5.8.4

[21] I. Holovatenko and A. Pysarenko, “Energy-efficient path-following control system of automated guided vehicles,” vol. 32, no. 2, pp. 390–403, 2021. 1.1

[22] X. Zhang, Y. Huang, Y. Rong, G. Li, H. Wang, and C. Liu, “Optimal trajectory planning for wheeled mobile robots under localization uncertainty and energy efficiency constraints,” vol. 21, no. 2, pp. 1–26, 2021. 1.1

[23] Y. Xiao, Y. Zhang, I. Kaku, R. Kang, and X. Pan, “Electric vehicle routing problem: A systematic review and a new comprehensive model with nonlinear energy recharging and consumption,” *Renewable and Sustainable Energy Reviews*, vol. 151, p. 111567, 2021. 1.1

[24] M. Bruglieri, M. Paolucci, and O. Pisacane, “A matheuristic for the electric vehicle routing problem with time windows and a realistic energy consumption model,” *Computers & Operations Research*, vol. 157, p. 106261, 2023. 1.1

[25] G. Rigatos, K. Busawon, and M. Abbaszadeh, “A nonlinear optimal control approach for the truck and n-trailer robotic system,” vol. 20, 2022. 1.1

[26] L. Guevara, R. Rocha, and F. Cheein, “Improving the manual harvesting operation efficiency by coordinating a fleet of n-trailer vehicles,” vol. 185, 2021. 1.1

[27] M. M. Michałek, “Trailer-maneuverability in n-trailer structures,” *IEEE Robotics and Automation Letters*, vol. 5, no. 4, pp. 5105–5112, 2020. 1.1

[28] H. Kücüksariyildiz, E. Canli, and K. Carman, “Experimentally detected aerodynamic drag coefficient of the agricultural tractor form considering effects of windshield angle and hood front shape,” *Energy*, vol. 296, p. 131167, 2024. 1.1

[29] Y. Marumo, T. Yokota, and A. Aoki, “Improving stability and lane-keeping performance for multi-articulated vehicles using vector follower control,” vol. 58, no. 12, pp. 1859–1872, 2020. 1.1

[30] Á. J. Prado, M. Torres-Torriti, J. Yuz, and F. A. Cheein, “Tube-based nonlinear model predictive control for autonomous skid-steer mobile robots with tire–terrain interactions,” *Control Engineering Practice*, vol. 101, p. 104451, 2020. 1.1

[31] K. Aro, L. Guevara, M. Torres-Torriti, F. Torres, and A. Prado, “Robust nonlinear model predictive control for the trajectory tracking of skid-steer mobile manipulators with wheel–ground interactions,” *Robotics*, vol. 13, no. 12, p. 171, 2024. 1.1

[32] Z. He, J. Liang, Y. Li, W. Hou, and Q. Shi, “Trajectory tracking control for self-driving vehicle considering road slope and adhesion condition,” *International Journal of Automotive Technology*, pp. 1–18, 2024. 1.1

[33] A. B. Robat, K. Arezoo, K. Alipour, and B. Tarvirdizadeh, “Dynamics modeling and path following controller of tractor-trailer-wheeled robots considering wheels slip,” *ISA transactions*, vol. 148, pp. 45–63, 2024. 1.1, 2.2.4

[34] P. Sarkar and H. Raheman, “Development and performance evaluation of an electric cabbage harvester with a precise cabbage pushing mechanism,” *Smart Agricultural Technology*, vol. 8, 2024. Type: Article. 1.1

[35] M. Padhiary, R. Kumar, and L. N. Sethi, “Navigating the future of agriculture: A comprehensive review of automatic all-terrain vehicles in precision farming,” *Journal of The Institution of Engineers (India): Series A*, pp. 1–16, 2024. 1.1

[36] A. J. Prado, M. Torres-Torriti, and F. A. Cheein, “Distributed tube-based nonlinear mpc for motion control of skid-steer robots with terra-mechanical constraints,” *IEEE Robotics and Automation Letters*, vol. 6, no. 4, pp. 8045–8052, 2021. 1.1

[37] J. A. T. Bustos, M. E. Orchard, M. Torres-Torriti, and F. A. Cheein, “GNSS-Based Estimation of Average Instantaneous Power Consumption in Electric Vehicles,” *IEEE Transactions on Industrial Electronics*, vol. 70, no. 9, pp. 9281 – 9290, 2023. Type: Article. 1.1

[38] H. Mediouni, A. Ezzouhri, Z. Charouh, K. El Harouri, S. El Hani, and M. Ghogho, “Energy Consumption Prediction and Analysis for Electric Vehicles: A Hybrid Approach,” *Energies*, vol. 15, no. 17, 2022. Type: Article. 1.1

[39] J. Leng, J. Peng, J. Liu, Y. Zhang, J. Ji, and Y. Zhang, “Profiling power consumption in low-speed autonomous guided vehicles,” *IEEE Robotics and Automation Letters*, vol. 9, no. 7, pp. 6027–6034, 2024. 2.1.1

[40] P. Saiteja, B. Ashok, A. S. Wagh, and M. E. Farrag, “Critical review on optimal regenerative braking control system architecture, calibration parameters and development challenges for evs,” *International Journal of Energy Research*, vol. 46, no. 14, pp. 20146–20179, 2022. 2.1.2

[41] N. Yang, L. Han, L. Bo, B. Liu, X. Chen, H. Liu, and C. Xiang, “Real-time adaptive energy management for off-road hybrid electric vehicles based on decision-time planning,” *Energy*, vol. 282, p. 128832, 2023. 2.1.3

[42] M. Lukassek, A. Völz, T. Szabo, and K. Graichen, “Model predictive path-following control for general n-trailer systems with an arbitrary guidance point,” in *2021 European Control Conference (ECC)*, pp. 1335–1340, IEEE, 2021. 2.2.1

[43] J. Kolb, G. Nitzsche, S. Wagner, and K. Röbenack, “On the backward path tracking control of n-trailer systems,” *SYSTEM THEORY, CONTROL AND COMPUTING JOURNAL*, vol. 1, no. 1, pp. 13–20, 2021. 2.2.2, 2.5.1.5, 2.5.1.6

[44] M. R. da Silva, J. Coelho, F. Gonçalves, F. Novais, and P. Flores, “Multibody dynamics in robotics with focus on contact events,” *Robotica*, vol. 42, no. 12, pp. 4070–4102, 2024. 2.2.3

[45] S. Mirtaheri and H. Zohoor, “Efficient formulation of the gibbs–appell equations for constrained multibody systems,” *Multibody System Dynamics*, vol. 53, no. 3, pp. 303–325, 2021. 2.2.3

[46] A. Naderolasli, K. Shojaei, and A. Chatraei, “Leader-follower formation control of euler-lagrange systems with limited field-of-view and saturating actuators: A case study for tractor-trailer wheeled mobile robots,” *European Journal of Control*, vol. 75, p. 100903, 2024. 2.2.3

[47] A. Habibnejad Korayem, “State and parameter estimation of vehicle-trailer systems,” 2021. 2.2.4

[48] X. Liu, F. Zhao, H. Hao, and Z. Liu, “Comparative analysis for different vehicle powertrains in terms of energy-saving potential and cost-effectiveness in china,” *Energy*, vol. 276, p. 127564, 2023. 2.3.4

[49] A. Malik, H. Haghbayan, J. Plosila, and M. E. C. Wu, “Integrated energy consumption analysis of autonomous mobile robots: A sensor fusion framework with real-time soc awareness,” *Robotics and Autonomous Systems*, 2025. 2.3.5

[50] K. Purohit, S. Srivastava, V. Nookala, V. Joshi, P. Shah, R. Sekhar, S. Panchal, M. Fowler, R. Fraser, M.-K. Tran, *et al.*, “Soft sensors for state of charge, state of energy, and power loss in formula student electric vehicle,” *Applied System Innovation*, vol. 4, no. 4, p. 78, 2021. 2.3.5

[51] B. Golanbari, A. Mardani, N. Farhadi, and G. Reina, “Machine learning applications in off-road vehicles interaction with terrain: An overview,” *Journal of Terramechanics*, vol. 116, p. 101003, 2024. 2.3.5

[52] M. H. Nampoothiri, B. Vinayakumar, Y. Sunny, and R. Antony, “Recent developments in terrain identification, classification, parameter estimation for the navigation of autonomous robots,” *SN Applied Sciences*, vol. 3, no. 4, p. 480, 2021. 2.3.5

[53] H. Rahnejat, P. Johns-Rahnejat, N. Dolatabadi, and R. Rahmani, “Multi-body dynamics in vehicle engineering,” *Proceedings of the Institution of Mechanical Engineers, Part K: Journal of Multi-body Dynamics*, vol. 238, no. 1, pp. 3–25, 2024. 2.4.2

[54] Y. Jin, Y. Li, B. He, X. Yang, and L. Zheng, “Mass estimation of tractor-semitrailer systems: An approach of dynamics and data fusion-driven in real environments,” *Measurement*, vol. 238, p. 115367, 2024. 2.4.3

[55] J. Zhang, Z. Han, K. Liu, and Y. Zhao, “Optimization for fuel consumption and tco of a heavy-duty truck with electricity-propelled trailer,” *Energy*, vol. 312, p. 133555, 2024. 2.4.3

[56] L. Guevara, F. Jorquera, K. Walas, and F. Auat-Cheein, “Robust control strategy for generalized n-trailer vehicles based on a dual-stage disturbance observer,” *Control Engineering Practice*, vol. 131, p. 105382, 2023. 2.5.1

[57] A. Keymasi Khalaji and M. Jalalnezhad, “Control of a tractor-trailer robot subjected to wheel slip,” *Proceedings of the Institution of Mechanical Engineers, Part K: Journal of Multi-body Dynamics*, vol. 0, no. 43, pp. 1–12, 2019. 2.5.1.1, 2.5.1.6

[58] J. Morales, J. L. Martinez, A. Mandow, and A. J. Garcia-Cerezo, “Steering the Last Trailer as a Virtual Tractor for Reversing Vehicles With Passive On- and Off-Axle Hitches,” *IEEE Transactions on Industrial Electronics*, vol. 60, pp. 5729–5736, dec 2013. 2.5.1.4, 2.5.1.5

[59] N. Evestedt, O. Ljungqvist, and D. Axehill, “Path tracking and stabilization for a reversing general 2-trailer configuration using a cascaded control approach,” in *2016 IEEE Intelligent Vehicles Symposium (IV)*, pp. 1156–1161, IEEE, 2016. 2.5.1.4

[60] M. Michałek and M. Kiełczewski, “Cascaded vfo set-point control for n-trailers with on-axle hitching,” *IEEE Transactions on Control Systems Technology*, vol. 22, no. 4, pp. 1597–1606, 2013. 2.5.1.4

[61] M. M. Michałek and M. Kiełczewski, “Robustification of the modular tracking control system for non-Standard N-Trailers of uncertain kinematics,” *Control Engineering Practice*, vol. 64, pp. 160–172, 2017. 2.5.1.5, 2.5.1.6, 2.5.1.8, 2.5.1.9, 2.5.1.10, 2.5.1.11

[62] A. Keymasi Khalaji and S. A. A. Moosavian, “Dynamic modeling and tracking control of a car with n trailers,” *Multibody System Dynamics*, vol. 37, no. 2, pp. 211–225, 2016. 2.5.1.5

[63] C. de Saxe and D. Cebon, “Measurement of articulation angle by image template matching,” *Proceedings of the Institution of Mechanical Engineers, Part D: Journal of Automobile Engineering*, vol. 233, no. 14, pp. 3801–3815, 2019. 2.5.1.5

[64] C. DeSaxe and D. Cebon, “Estimation of trailer off-tracking using visual odometry,” *Vehicle System Dynamics*, vol. 57, no. 5, pp. 752–776, 2019. 2.5.1.5

[65] O. Ljungqvist, N. Evestedt, D. Axehill, M. Cirillo, and H. Pettersson, “A path planning and path-following control framework for a general 2-trailer with a car-like tractor,” *Journal of Field Robotics*, vol. 36, no. 8, pp. 1345–1377, 2019. 2.5.1.5

[66] D. Arnström, *State Estimation for Truck and Trailer Systems using Deep Learning*. PhD thesis, Linkoping University, 2018. 2.5.1.5

[67] J. Han, “From PID to active disturbance rejection control,” in *IEEE Transactions on Industrial Electronics*, vol. 56, pp. 900–906, 2009. 2.5.1.7

[68] R. Madoński and P. Herman, “Survey on methods of increasing the efficiency of extended state disturbance observers,” *ISA Transactions*, vol. 56, pp. 18–27, 2015. 2.5.1.8, 2.5.1.9

[69] W. R. Abdul-adheem and I. K. Ibraheem, “Improved Sliding Mode Nonlinear Extended State Observer based Active Disturbance Rejection Control for Uncertain Systems with Unknown Total Disturbance,” *International Journal of Advanced Computer Science and Applications*, vol. 7, no. 12, pp. 80–93, 2016. 2.5.1.9

[70] T. Jiang, C. Huang, and L. Guo, “Control of uncertain nonlinear systems based on observers and estimators,” *Automatica*, vol. 59, pp. 35–47, 2015. 2.5.1.9

[71] B. Sebastian and P. Ben-Tzvi, “Active disturbance rejection control for handling slip in tracked vehicle locomotion,” *Journal of Mechanisms and Robotics*, vol. 11, no. 2, 2019. 2.5.1.9

[72] D. J. Jwo and S. H. Wang, “Adaptive fuzzy strong tracking extended Kalman filtering for GPS navigation,” *IEEE Sensors Journal*, vol. 7, pp. 778–789, may 2007. 2.5.1.9

[73] L. Guevara, M. Michałek, and F. Auat Cheein, “Headland turning algorithmization for autonomous n-trailer vehicles in agricultural scenarios,” vol. 175, 2020. 2.5.1.10

[74] L. Guevara, M. Michałek, and F. Cheein, “Collision risk reduction of n-trailer agricultural machinery by off-track minimization,” vol. 178, 2020. 2.5.1.10

[75] P. Morin and C. Samson, "Motion Control of Wheeled Mobile Robots," in *Springer Handbook of Robotics* (B. Siciliano and O. Khatib, eds.), pp. 799–826, Springer Berlin Heidelberg, 2008. 2.5.1.10

[76] N. Deniz, F. Jorquera, and F. A. Cheein, "Absolute joint-angle estimation of generalised n-trailer vehicles equipped with incremental encoders using moving horizon estimation," *ISA transactions*, vol. 143, pp. 678–691, 2023. 2.5.2

[77] M. M. Michałek, "A highly scalable path-following controller for n-trailers with off-axle hitching," *Control Engineering Practice*, vol. 29, pp. 61–73, 2014. 2.5.2.1, 2.5.2.1

[78] I. D. Landau, R. Lozano, M. M'Saad, and A. Karimi, *Adaptive control: algorithms, analysis and applications*. Springer Science & Business Media, 2011. 2.5.2.3

[79] E. D. Sontag and Y. Wang, "Output-to-state stability and detectability of nonlinear systems," *Systems & Control Letters*, vol. 29, no. 5, pp. 279–290, 1997. 2.5.2.3, 2.5.3

[80] G. Sanchez, M. Murillo, and L. Giovanini, "Adaptive arrival cost update for improving moving horizon estimation performance," *ISA transactions*, vol. 68, pp. 54–62, 2017. 2.5.2.5, 2.5.5.1, 2.5.5.1

[81] M. A. Müller, "Nonlinear moving horizon estimation in the presence of bounded disturbances," *Automatica*, vol. 79, pp. 306–314, 2017. 2.5.2.5

[82] N. Deniz, M. Murillo, G. Sanchez, and L. Giovanini, "Robust stability of moving horizon estimation for non-linear systems with bounded disturbances using adaptive arrival cost," *IET Control Theory & Applications*, vol. 14, no. 18, pp. 2879–2888, 2020. 2.5.2.5

[83] L. Grüne and J. Pannek, "Nonlinear model predictive control," in *Nonlinear model predictive control: Theory and algorithms*, pp. 45–69, Springer, 2016. 2.5.2.6

[84] B. Houska, H. J. Ferreau, and M. Diehl, "Acado toolkit—an open-source framework for automatic control and dynamic optimization," *Optimal control applications and methods*, vol. 32, no. 3, pp. 298–312, 2011. 2.5.4.1

[85] M. Murillo, G. Sánchez, L. Genzelis, and L. Giovanini, "A path-planning algorithm based on receding horizon techniques," in *IX jornadas argentinas de robótica (JAR)*, pp. 1–6, 2017. 2.5.5.2

[86] J. B. Rawlings, D. Q. Mayne, M. Diehl, *et al.*, *Model predictive control: theory, computation, and design*, vol. 2. Nob Hill Publishing Madison, WI, 2020. 2.5.5.3, 2.5.5.3

[87] D. A. Allan, C. N. Bates, M. J. Risbeck, and J. B. Rawlings, "On the inherent robustness of optimal and suboptimal nonlinear mpc," *Systems & Control Letters*, vol. 106, pp. 68–78, 2017. 2.5.5.3

[88] S. A. Roth and P. Batavia, “Evaluating path tracker performance for outdoor mobile robots,” in *Automation Technology for Off-Road Equipment Proceedings of the 2002 Conference*, p. 388, American Society of Agricultural and Biological Engineers, 2002. 2.5.5.4

[89] K. Genikomsakis and G. Mitrentsis, “A computationally efficient simulation model for estimating energy consumption of electric vehicles in the context of route planning applications,” vol. 50, pp. 98–118, 2017. 2.5.7, 2.5.7

[90] P. Iora and L. Tribioli, “Effect of ambient temperature on electric vehicles energy consumption and range: Model definition and sensitivity analysis based on nissan leaf data,” *World Electric Vehicle Journal*, vol. 10, no. 1, p. 2, 2019. 2.5.7

[91] J. Romero Schmidt and F. Auat Cheein, “Prognosis of the energy and instantaneous power consumption in electric vehicles enhanced by visual terrain classification,” vol. 78, pp. 120–131, 2019. 2.5.7, 2.5.7, 2.5.8, 2.5.8.4

[92] S. Zhou, Q. Wang, and J. Liu, “Control strategy and simulation of the regenerative braking of an electric vehicle based on an electromechanical brake,” *Transactions of FAMENA*, vol. 46, no. 1, pp. 23–40, 2022. 2.5.7

[93] W. Wu, S. Wang, W. Wu, K. Chen, S. Hong, and Y. Lai, “A critical review of battery thermal performance and liquid based battery thermal management,” *Energy conversion and management*, vol. 182, pp. 262–281, 2019. 2.5.7

[94] G. Reina, R. Galati, and A. Milella, “All-terrain estimation for mobile robots in precision agriculture,” in *2018 IEEE International Conference on Industrial Technology (ICIT)*, pp. 63–68, IEEE, 2018. 2.5.7

[95] A. Ghobadpour, G. Monsalve, A. Cardenas, and H. Mousazadeh, “Off-road electric vehicles and autonomous robots in agricultural sector: Trends, challenges, and opportunities,” *Vehicles*, vol. 4, no. 3, pp. 843–864, 2022. 2.5.7